Experimental Evaluation of Low-Loss/Non-Dispersive Terahertz Waveguides

by

Robert Levi Smith
B.Eng., University of Victoria, 2011
M.A.Sc., University of Victoria, 2014

A Dissertation Submitted in Partial Fulfillment of the Requirements for the Degree of

DOCTOR OF PHILOSOPHY

in the Department of Electrical and Computer Engineering

Experimental Evaluation of Low-Loss/Non-Dispersive Terahertz Waveguides

by

Robert Levi Smith
B.Eng., University of Victoria, 2011
M.A.Sc., University of Victoria, 2014

Supervisory Committee

Dr. Thomas Darcie, Supervisor
(Department of Electrical and Computer Engineering)

Dr. Jens Bornemann, Departmental Member
(Department of Electrical and Computer Engineering)

Dr. Stephanie Willerth, Outside Member
(Department of Mechanical Engineering)

ABSTRACT

Low-loss waveguides with minimal dispersion are desired throughout the electromagnetic spectrum. These properties are difficult to achieve in the Terahertz (THz) region due to material and geometric constraints. This thesis focuses on the design, fabrication, and testing of waveguide-based devices using two promising technologies: the free-space metallic-slit waveguide (MSWG) and the coplanar strip (CPS) waveguide on a thin (1 μm) commercial silicon nitride membrane. The work presented here differs from standard THz waveguide research which commonly uses the field radiated by a photoconductive antenna (THz optics) for excitation and detection. To improve upon system integration, a focus is placed on planar waveguide devices without refractive THz elements. Three main waveguide devices are investigated. First, an edge-coupled MSWG-based linear tapered slot antenna (LTSA) was used for THz-Time Domain Spectroscopy (TDS). This device functions as an alternative to a standard photoconductive switch coupled to a silicon lens and maintains comparable performance. Next an edge-coupled tapered MSWG was investigated. The MSWG conductor separation was increased to a low-loss configuration where the field propagated for 24 mm, after which the conductors were tapered to focus the field onto the receiving active region where a THz-bandwidth pulse was detected. Finally a CPS waveguide was fabricated on a thin silicon nitride membrane where a THz-bandwidth pulse was detected after propagating for 10 mm. The active regions for this device were fabricated using a unique method. This method results in the creation of thousands of small (40 μm $\times$ 20 μm) active regions (from a 4 mm $\times$ 4 mm host substrate) which can be placed anywhere for THz excitation and detection. The small active regions in conjunction with the CPS waveguide on the silicon nitride membrane provide an excellent platform for THz system testing. A single membrane can host many THz circuits which can be made "active" by the placement of a few thin-film photoconductive devices. Main potential future applications include waveguide-based spectroscopy and coherent THz-bandwidth circuit analysis.

Contents

List of Figures

Acronyms

ADC	Analog-to-Digital Converter
Au	Gold
CPS	Coplanar Strip
CW	Continuous Wave
DC	Direct Current
DFT	Discrete Fourier Transform
DI	Deionized
EDFA	Erbium-doped fiber amplifier
FBPS	Fiber-Based Probe-Station
FIB	Focus Ion Beam
FWHM	Full Width at Half Maximum
GHz	Gigahertz
GVD	Group Velocity Dispersion
HDPE	High Density Polyethylene
HF	Hydrofluoric
HRFZ-Si	High Resistivity Float Zone Silicon
IPA	Isopropyl Alcohol
IR	Infrared Radiation

LOR	Lift-off Resist
LTG-GaAs	Low Temperature Grown Gallium Arsenide
LTSA	Linear Tapered Slot Antenna
MBE	Molecular Beam Epitaxy
MSWG	Metallic-Slit Waveguide
NMP	N-Methyl-2-Pyrrolidone
Np	Neper
PC	Photoconductive
PCA	Photoconductive Antenna
PEC	Perfect Electric Conductor
PPCF	Plastic Photonic Crystal Fiber
PPWG	Parallel-Plate Waveguide
PVD	Physical Vapor Deposition
QCL	Quantum Cascade Laser
RF	Radio Frequency
RTD	Resonant Tunneling Diode
SI-GaAs	Semi-insulating Gallium Arsenide
SOS	Silicon-on-Sapphire
TCE	Trichloroethene
TEM	Transverse Electromagnetic
THz	Terahertz
THz-TDS	Terahertz Time Domain Spectroscopy
Ti	Titanium
TIR	Total Internal Reflection
TM	Transverse Magnetic
TMIC	Terahertz monolithic integrated circuit
TWWG	Two-Wire Waveguide

UV	Ultra Violet
VDW	Van der Waals

ACKNOWLEDGEMENTS

I would like to thank:

My girlfriend Ghazal Hajisalem, my family, and my friends, for supporting me during my studies.

My supervisor Dr. Thomas Darcie, for many great discussions and openly providing guidance.

Professors Dr. Jens Bornemann and Dr. Reuven Gordon, for allowing me to use their equipment and space.

Professor Dr. Thomas Tiedje, for fabricating our photoconductive devices.

My lab colleagues Afshin Jooshesh and James (Jinye) Zhang, for providing assistance whenever possible.

Chapter 1

Introduction

1.1 Thesis Format

This thesis presents our experimental research completed on low-loss waveguides with minimal dispersion. A publication-based format is used and the bulk of the novel research is copied into the Appendices. Chapter 1 provides a background to Terahertz (THz) engineering which includes example applications, standard methods for THz field generation and detection, and a summary of THz waveguiding technologies. Chapter 2 discusses the fabrication methods used during the research. Chapter 3 describes the motivation for each of the contributions. Chapter 4 is the conclusion and identifies a few potential future projects.

1.2 THz Gap

The THz gap is an isolated region of the electromagnetic spectrum with exists between electronic and photonic regions (Fig. 1.1). Note that the THz gap range is not consistently defined across literature; however, it typically falls within the 100 Gigahertz (GHz) to 30 THz range [3]. A key benefit of the THz gap is that photon energies are low (< 0.1 eV) such that the dangers associated with ionizing radiation (> 10 eV) are removed. Also THz wavelengths are relatively short that admirable resolution (sub-mm) can be achieved in an imaging system.

There are two logical approaches to accessing the THz gap, either using high frequency electronic methods or low frequency photonic methods. Resonant Tunneling Diodes (RTDs) approach the THz gap from the electronic side of the spectrum

and have demonstrated room temperature generation of frequencies up to 1.92 THz (0.4 μW) [4]. Quantum Cascade Lasers (QCLs) approach from the photonic side of the spectrum and have demonstrated room temperature operation down to 2.06 THz (4.2 μW) [5]. A hybrid room temperature electronic/photonic technique called Photoconductive (PC) switching generates a broad spectrum of frequencies (typically 0 to 4 THz) with potentially large average powers (4 mW [6]).

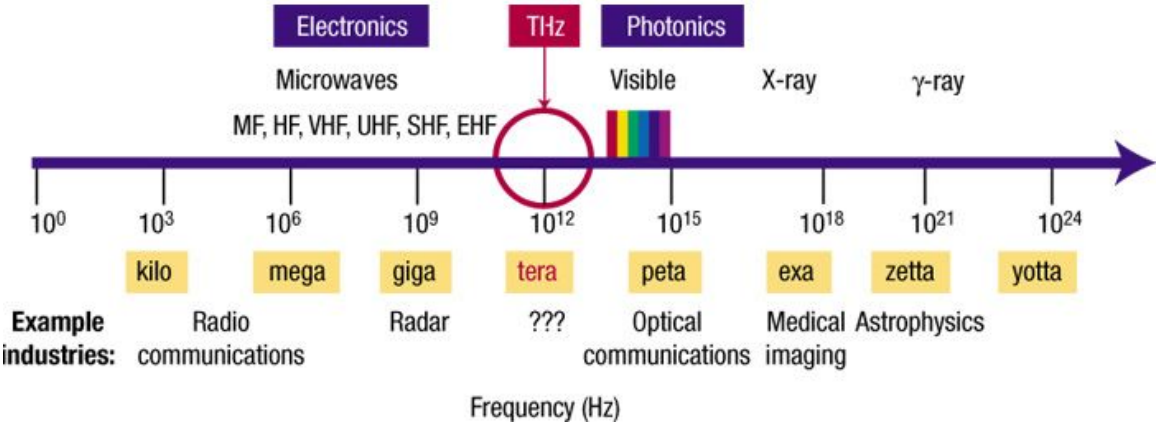

Figure 1.1: Terahertz gap. Reprinted by permission from [7]. © 2002 Springer Nature.

Within the THz gap realistic materials (like humid air) exhibit a chemically-dependent loss-spectrum which gives them a unique fingerprint which can be used for unknown material identification. Figure 1.2 plots the absorption spectrum for a few chemicals (H_2O, CO, NH_3, and H_2S) [8]. A room temperature experimental technique called Terahertz Time Domain Spectroscopy (THz-TDS) (discussed later) is commonly used to probe a portion of these absorption spectra.

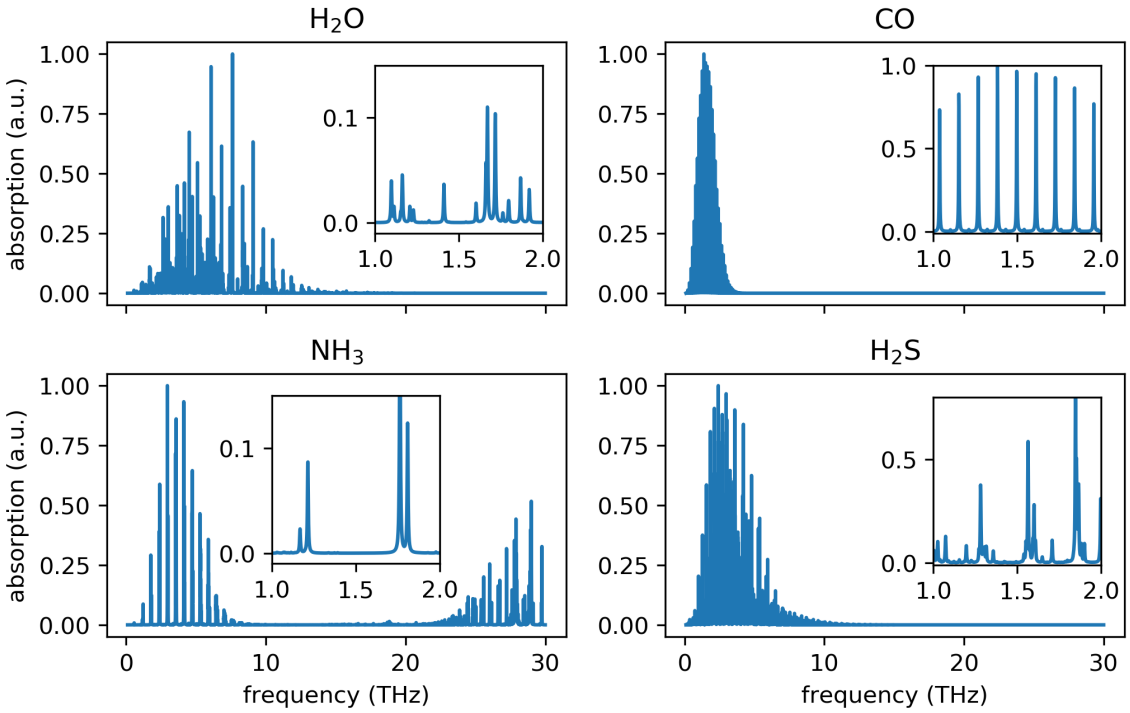

Figure 1.2: Chemical absorption spectrum in the THz region.

1.3 THz Generation and Detection [9]

THz fields can be generated using a number of methods, for example, photoconductive switching [10], photoconductive mixing [11], optical rectification [12], microwave frequency multiplication [13], backward wave oscillators [14], free-electron lasers [15], or quantum cascade lasers [16]. Each method has its benefits and drawbacks, and the price can vary substantially - from thousands of dollars for the photoconductive methods, to millions of dollars for free-electron lasers. This thesis only focuses on photoconductive devices because they are an inexpensive option which perform admirably at room temperature ($>$ 4 THz bandwidth with resonable average output powers).

A photoconductive device consists of a voltage-biased semiconductor which is excited by an optical laser. Optical excitation of the photoconductor results in the generation of electron-hole pairs which alters the substrate conductivity. The change in conductivity in conjunction with an applied or induced electric field generates a photocurrent with frequency components that can extend into the THz range. A com-

mon substrate material is Low Temperature Grown Gallium Arsenide (LTG-GaAs) ($E_g^{GaAs} = 1.42$ eV) because it can function as a transmitter or receiver (short carrier-lifetime) and absorbs standard near-Infrared Radiation (IR) ($E_{780nm} = 1.59$ eV) optical sources.

Figure 1.3 illustrates a typical photoconductive device coupled to a High Resistivity Float Zone Silicon (HRFZ-Si) lens. In this document this structure is called a Photoconductive Antenna (PCA). The HRFZ-Si lens serves two purposes, it collimates the radiation emitted by the antenna and it maximizes the transmitted power by minimizing refraction losses. Refraction losses occur because the discrepancy between dielectric constants at the Semi-insulating Gallium Arsenide (SI-GaAs)/air interface. Figure 1.4 illustrates the trapped rays which occur without the HRFZ-Si lens. The critical angle, θ_c, for a GaAs substrate is $\theta_c \approx \sin^{-1}(1/\sqrt{13}) = 16.1°$. Without a HRFZ-Si lens only $\approx 4\%$ of the total power will escape the substrate (350 μm thick). Usage of a HRFZ-Si lens eliminates refraction loss, however a reflection still exists at the interface, therefore at most $\approx 68\%$ of the incident power is radiated into free-space.

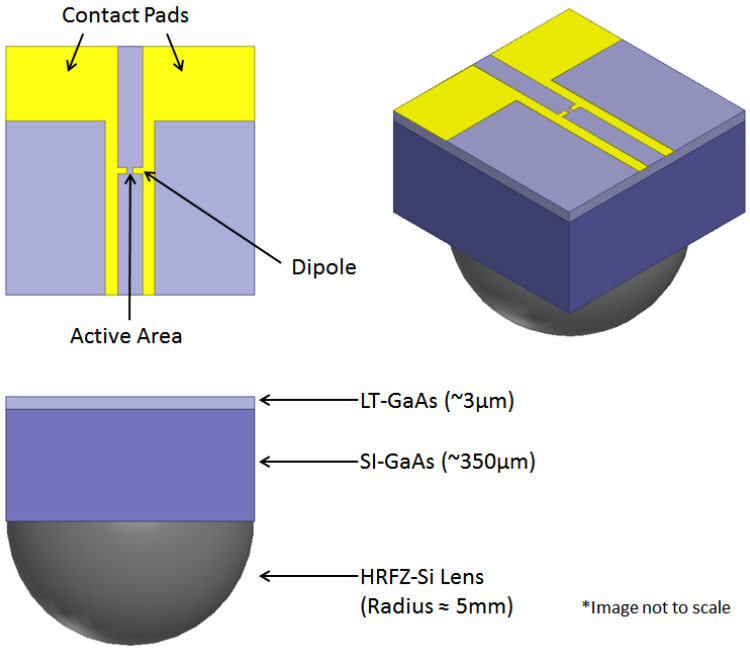

Figure 1.3: Illustration of a THz PCA [9].

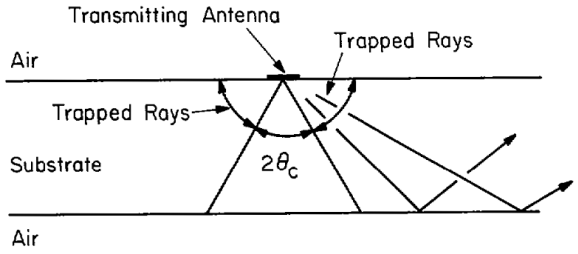

Figure 1.4: Trapped substrate rays. Reprinted by permission from [17]. © 1982 IEEE.

1.3.1 Photoconductive Mixing [9]

Photoconductive mixing is used to generate a Continuous Wave (CW) THz signal by combining two lasers, λ_1 and λ_2, separated by nanometer-scale wavelength difference, $\Delta\lambda$. The combined beam is then focused onto the voltage-biased active area of a PCA. Optimal mixing occurs when the spatial distribution and polarization state of the two lasers are identical [18]. Figure 1.5 illustrates a standard photomixer. The total laser intensity is modulated at beat frequency:

$$f_{beat} = \Delta\nu = \frac{c|\lambda_1 - \lambda_2|}{\lambda_1\lambda_2} = \frac{c|\Delta\lambda|}{\lambda_1\lambda_2}, \tag{1.1}$$

where c is the speed of light in a vacuum. For a beat frequency of 1 THz at a center wavelength of $\lambda_c = 854$ nm a wavelength separation of $\Delta\lambda = 2.431$ nm is required.

Photomixing was initially investigated by [19], which states that the THz emission is dependent on the photocarrier density [20]:

$$\frac{dn}{dt} = \frac{\eta}{h\nu_c Ad}P(\omega, t) - \frac{n}{\tau}, \tag{1.2}$$

where $\omega = 2\pi\Delta\nu$, n is the photocarrier density, η is the quantum efficiency, A is the active area, d is the absorption depth, $h\nu_c$ is the photon energy, τ_c is the 1/e carrier lifetime. The incident optical power is given by:

$$P(\omega, t) \approx P_1 + P_2 + 2\sqrt{mP_1P_2}cos(\omega t), \tag{1.3}$$

where P_1 and P_2 are the laser powers at λ_1 and λ_2, respectively. Modulation depth $(0 \leq m \leq 1)$ accounts for the polarization overlap between the two lasers.

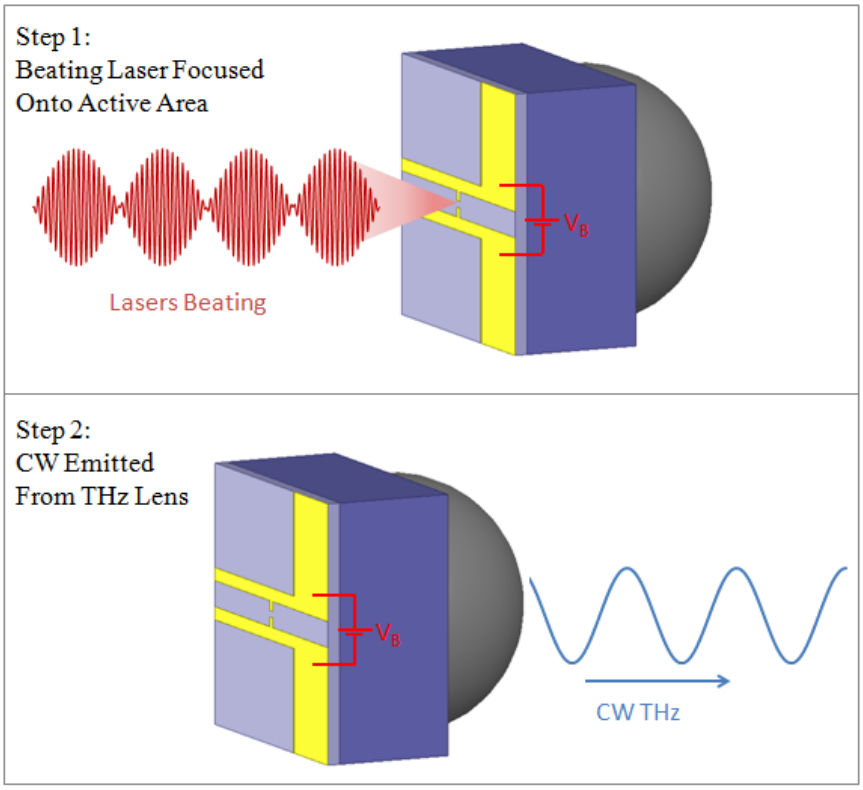

Figure 1.5: Photoconductive mixing. a) Incident beating CW lasers focused onto biased active area. b) CW THz emitted from the back of the substrate [9].

THz radiation is generated by driving an antenna with an oscillating current source. This is achieved by applying a fixed voltage across a modulated conductance which is given by:

$$G(\omega, t) \approx \frac{\mu e d\sqrt{A}}{r} n(\omega, t) \approx G_0[1 + \beta sin(\omega t + \phi)], \tag{1.4}$$

where μ is the effective carrier mobility, e is the elementary charge, r is the width of the photoconductive gap. The second part of Eqn. 1.4 is used to simplify the concept of photomixing; G_0 is the average photoconductance and β represents the modulation of the photoconductance.

Photomixing is conceptually simple but its performance is limited by a key difficulty: the average source resistance, G_0^{-1}, is much larger than the antenna radiation resistance, R_A. Typical values for G_0 are in the $(0.5\ M\Omega)^{-1}$ region whereas $R_A < 200$ Ω. This results in poor transmitter and receiver antenna efficiency, thereby limiting the practicality of a radiating photomixing source.

This concept is illustrated by considering the following circuit (Figure 1.6) which models an ideal (no capacitance) photomixer:

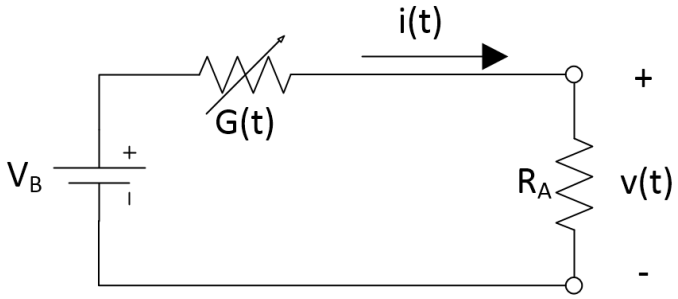

Figure 1.6: Photoconductive mixer circuit equivalent.

where:

$$i(t) = \frac{G(t)V_B}{G(t)R_A + 1}, \tag{1.5a}$$

$$v(t) = i(t)R_A = \frac{G(t)V_B R_A}{G(t)R_A + 1}, \tag{1.5b}$$

the total radiated power, is given by:

$$P_{rad} = \left(\frac{i_{p-p}}{2\sqrt{2}}\right)^2 R_A, \tag{1.6}$$

where i_{p-p} is the peak-to-peak current. In a realistic situation (except ignoring C) we can select: $G_0 = (0.5\ M\Omega)^{-1}$, $\beta = 1$, $R_A = 100\ \Omega$, $f = 1$ THz, and $V_B = 20$ V which results in 80 nW of radiated power.

1.3.2 Photoconductive Switching [9]

Photoconductive switching is the process of generating a pulsed THz signal. Pulsed THz signals are generated by focusing a sub-picosecond optical pulse onto the active area of a PCA as shown in Fig. 1.7. The semiconductor conductivity rises sharply when the optical pulse is absorbed and falls as the carriers trap and recombine when the optical pulse dissipates.

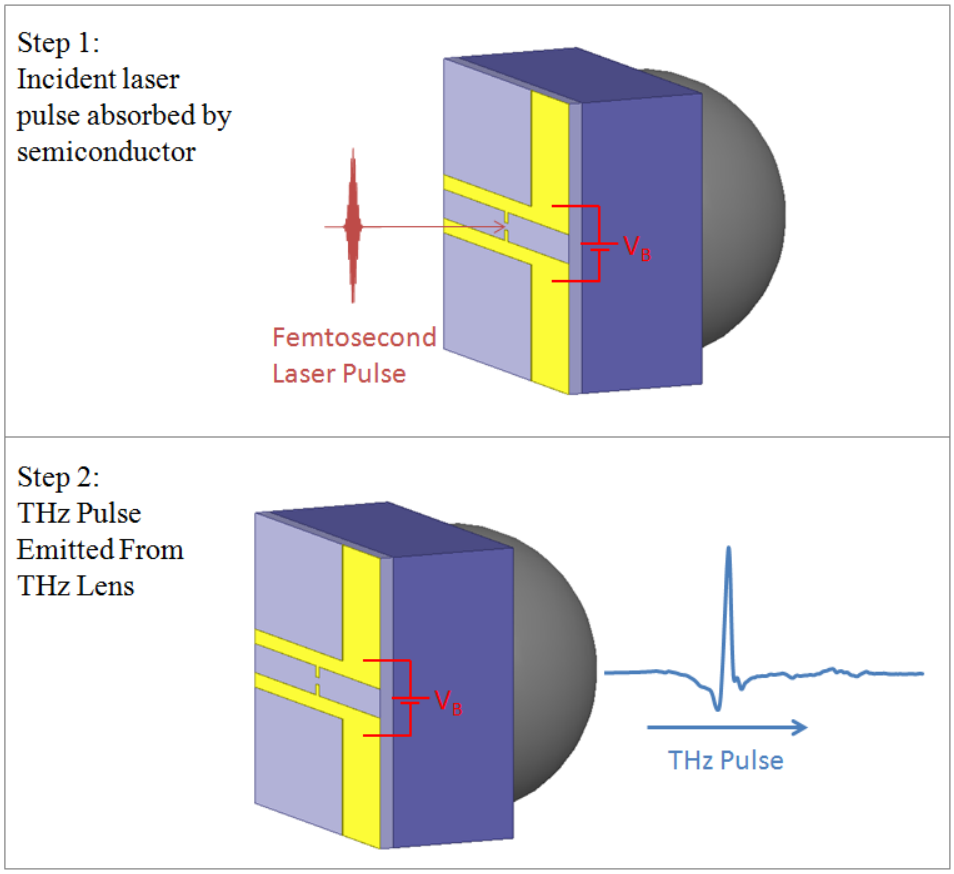

Figure 1.7: Photoconductive switching. a) incident femtosecond pulse focused onto biased active area. b) THz pulse emitted from the back of the substrate [9].

During excitation photocarriers are generated and accelerated along the electric field, E_B, established by V_B towards the antenna electrodes. The emitted THz field is proportional acceleration of charge, $E_{THz} \propto \frac{dI_{PC}}{dt}$, where the photocurrent is given by [3]:

$$I_{PC} = I_{amp}\left[\exp\left(\frac{\tau_p^2}{4\tau_c^2} - \frac{t}{\tau_c}\right)\cdot \operatorname{erfc}\left(\frac{\tau_p}{2\tau_c} - \frac{t}{\tau_p}\right) - \exp\left(\frac{\tau_p^2}{4\tau_{cs}^2} - \frac{t}{\tau_{cs}}\right)\cdot \operatorname{erfc}\left(\frac{\tau_p}{2\tau_{cs}} - \frac{t}{\tau_p}\right)\right] \tag{1.7}$$

where $I_{amp} = \frac{\sqrt{\pi}}{2}\mu_e E_{DC} I_{opt}$, μ_e is the electron mobility, E_B is the electric field established by V_B, I_{opt} is the optical pump intensity, τ_p is the optical pulse width (Gaussian), τ_c is the carrier lifetime, τ_s is the momentum relaxation time, $\tau_{cs} = (\tau_c^{-1} + \tau_s^{-1})^{-1}$, and $\operatorname{erfc}(x) = 1 - \operatorname{erf}(x) = \frac{2}{\pi}\int_x^\infty e^{-t^2} dt$.

Figure 1.8a plots the radiated E-field using Eqn. (1.7) for various τ_c. Figure 1.8b plots the spectral response. Typical optical pulse width ($\tau_p = 0.048$ ps) and momentum relaxation time ($\tau_s = 0.03$ ps) were used [3]. I_{amp} was set to 1.0A because we are interested in the relative difference. From Fig. 1.8b it is clear that substrates with a long carrier lifetime radiate better than short carrier lifetimes. This means that LTG-GaAs ($\tau_c \approx 0.5$ ps) is not required for a transmitter, however it functions adequately [21].

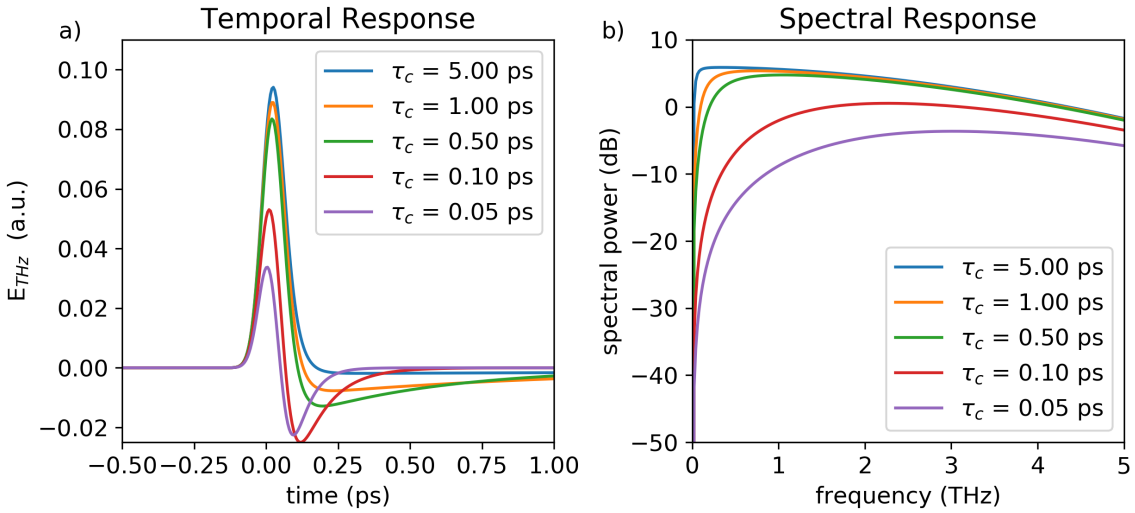

Figure 1.8: Radiated E-field, using Eqn. (1.7): $I_{amp} = 1$, $\tau_p = 0.048$ ps, $\tau_s = 0.03$ ps.

As with photomixing, the conductance is dependent on the incident optical power. For photoconductive switching the instantaneous peak pulse power is large, $P_{peak} \approx$ 4kW, compared to photomixing where $P_{max}(\omega, t) \approx$ 50mW. The conductance of the photoconductive switch becomes comparable to the radiation resistance during the illumination time resulting in higher THz output powers.

1.3.3 THz Field Sampling

A PCA on LTG-GaAs can act as either a transmitter or receiver, the only difference is the connection to external circuitry. For a transmitter an electrical bias is applied to the active area via the contact pads. For a receiver the contact pads are connected to a lock-in amplifier which is used to cleanly measure the small photocurrents (100 pA - 10 nA) induced by the incident THz field.

No Analog-to-Digital Converter (ADC) exists that can sample at 60×10^{12} samples/s, therefore another method must be used to reconstruct the temporal profile of a THz bandwidth pulse. Figure 1.10 gives an overview of the THz generation and detection process using PCAs. Photocarriers are generated in the receiver when the optical pulse reaches the semiconductor which exist for the carrier lifetime. The photocarriers will become accelerated by the incoming THz field creating a photocurrent, $J(t)$. This current can be calculated by [3]:

$$J(t) = \int_{-\infty}^{t} \sigma_s(t - t') E_{THz}(t') dt', \tag{1.8}$$

where $E_{THz}(t)$ is the incident THz pulse and $\sigma_s(t)$ is the receiver surface conductivity which is given by:

$$\sigma_s(t) = \frac{2\sigma_0}{\sqrt{\pi}\tau_p} \int_{-\infty}^{t} e^{-t'^2/\tau_p^2} \left(1 - e^{-(t-t')/\tau_s}\right) e^{-(t-t')/\tau_c} dt', \tag{1.9}$$

where,

$$\sigma_0 = \frac{\sqrt{\pi} e \mu_e (1 - R_{opt}) I_0 \tau_p}{2\hbar\omega}, \tag{1.10}$$

and e is the electron charge, μ_e is the receiver's electron mobility, R_{opt} is the substrate reflectance, I_0 is the optical intensity, $\hbar = h/2\pi$ where h is Planck's constant, ω is the angular frequency, τ_p is the optical pulse width, τ_s is the momentum relaxation time, and τ_c is the carrier lifetime.

In the frequency domain Eqn. 1.8 is given by the pointwise product of the individual Fourier transforms (convolution theorem):

$$\mathcal{F}\{J\} = \mathcal{F}\{\sigma_s\} \cdot \mathcal{F}\{E_{THz}\}. \tag{1.11}$$

The simplest way to interpret this equation is to define the ideal scenario, in which the received photocurrent should be directly proportional to E_{THz}. This is accomplished when $\mathcal{F}\{\sigma_s\} =$ constant, a condition that is satisfied when $\sigma_s(t)$ is an impulse. Therefore $\sigma_s(t)$ should approximate an impulse (pulse width < 1 ps). LTG-GaAs has a short carrier lifetime (≈ 0.5 ps) whereas SI-GaAs has a much longer carrier lifetime (hundreds of picoseconds) [21]. Figure 1.9 illustrates $\sigma_s(t)$ for SI-GaAs and LTG-GaAs where it is clear that LTG-GaAs is a closer approximation to a impulse.

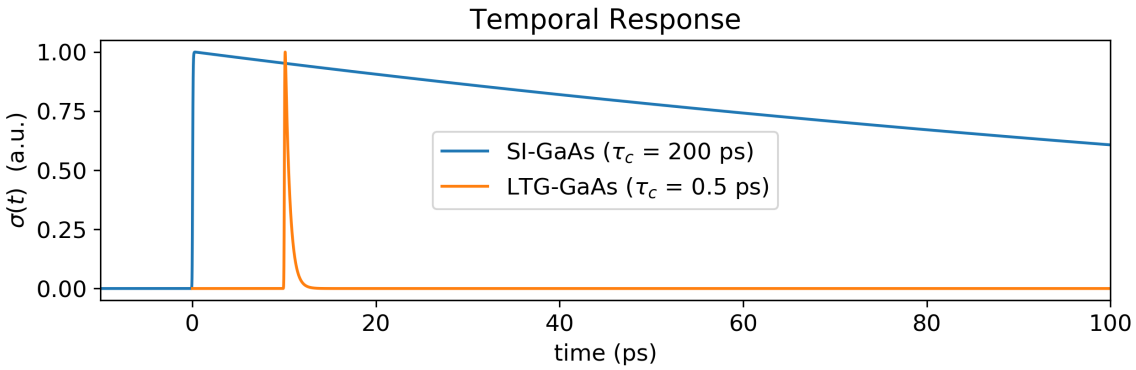

Figure 1.9: SI-GaAs and LTG-GaAs surface conductivities.

Experimentally the temporal THz electric field profile is reconstructed by varying the time delay between the received incident THz and optical pulses. A mechanical delay line is commonly used to introduce this delay and the sampling rate becomes a function the speed of light and translational step size, Δx (in μm), which is given by:

$$\Delta t = \frac{\Delta x(2 \times 1\mu m)}{3 \times 10^8 m/s} = \Delta x \times 6.67 \frac{fs}{\mu m}. \tag{1.12}$$

Current stepper motors are capable of achieving minimum step sizes of < 0.2 μm which corresponds to a sampling period of 1.33 fs. This translates into a Nyquist frequency of 376 THz which will not be a limiting factor.

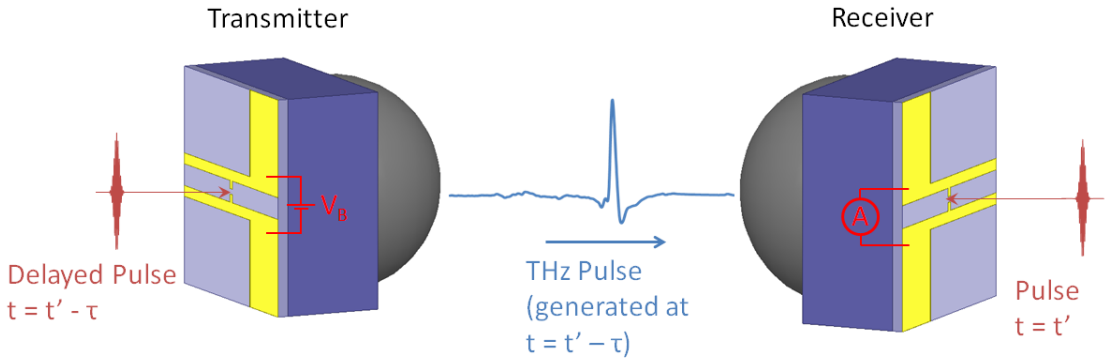

Figure 1.10: THz pulse detection. The THz pulse is plotted by varying the delay between the receivers optical pulse and incident THz pulse.

1.4 THz-Time Domain Spectroscopy

When introducing THz waves it is common to discuss THz-TDS because it is one of the most used applications. THz-TDS is used to obtain spectrographic information from a sample (e.g. Fig. 1.2). Ideally, in the time domain, the spectrum is obtained by generating an infinitely short pulse, transmitting it through a sample, and continuously sampling the received pulse forever. In reality this is not possible, however it is possible to generate a short electrical pulse with frequency components extending into the THz region. This pulse can be sampled at discrete points in time over a finite duration. To better define a short pulse Fig. 1.11 plots the temporal and spectral response for a selection of Gaussian pulses with differing Full Width at Half Maximums (FWHMs). From Fig. 1.11 it is clear that very short pulses (FWHM $<<$ 50 fs) are required to achieve a broad frequency response which spans across 30 THz. It is possible to generate and receive pulses with wide bandwidths ($>$ 15 THz) [22, 23], however they are frequently avoided due to experimental difficulties. It is more common to investigate the 0.1 THz to 4 THz region because experimentation is simpler and many (but not all) spectroscopic lines appear in this range (see Fig. 1.2). Stringent environmental controls are not necessary for many THz-TDS applications, meaning it can be performed in an illuminated area at room temperature; however, water vapor will likely be detected.

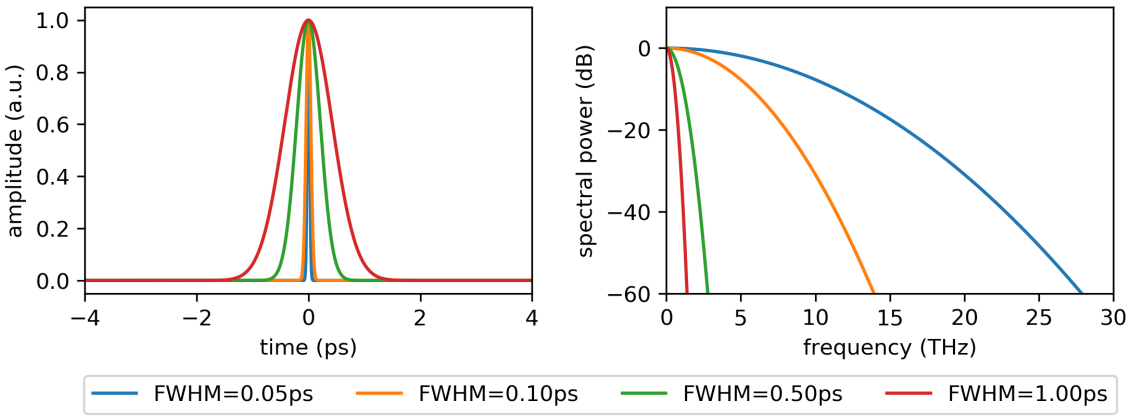

Figure 1.11: Gaussian frequency response for a selection of full width at half maximums.

1.4.1 THz-TDS Experiment

THz-TDS uses a configuration similar to Fig. 1.10. Figure 1.12 illustrates the standard component arrangement defining the optical delivery paths. A femtosecond laser generates an optical pulse train (for example, 780 nm wavelength, 100 fs pulse width, 80 MHz repetition rate, 20 mW average power) which is directed though a beam splitter to obtain two beams which are sent to the transmitter and receiver PCAs. In the transmitter path, the optical beam passes through a mechanical delay line and optical chopper before becoming focused onto the PCA active area. In the receiver path, the optical beam is simply focused on the PCA active area. The optical waist size at both active areas is approximately 7 μm (for a 5 μm gap). The delay line can be placed in either path, however the optical chopper must be placed in the transmitter path such that the transmitted THz pulse is modulated at a known frequency. The transmitter typically has $\approx$20 V_{DC} bias applied for a 5 μm gap active area (Fig. 1.3). The receiver is connected to a lock-in amplifier (referenced to the optical chopper) to measure the induced photocurrent. It is crucial that the total transmitter path $(a, b, c, d_1, d_2, e, f, g)$ and receiver path (x_1, x_2, y, z) have the correct lengths; otherwise no pulse will be detected. To setup the THz-TDS experiment the mechanical delay line should be placed near its half-way point (middle of travel length), then set:

$$a + b + c + d_1 + d_2 + \frac{e}{n_{sub}} + f + \frac{g}{n_{sub}} = x_1 + x_2 + y + z, \tag{1.13}$$

which can be simplified given that $a + c = y$, $b = d_1$, $z = x_2$, and approximating that the substrate and silicon lenses are air ($n_{sub} = 1$), then $d_2 + e + f + g = x_1$. These conditions and assumptions result in the simple condition that $b = z$.

The exact lengths are not crucial providing $b = z$ near the middle of the delay line, however the lengths are constrained by beam divergence (not typically an issue with adequate collimation) and physical space available. Table 1.1 tabulates the lengths that were found useful (sufficient working space for experiment). Note the odd choice of units (inches) is selected because it corresponds to the optical tables bolt spacing.

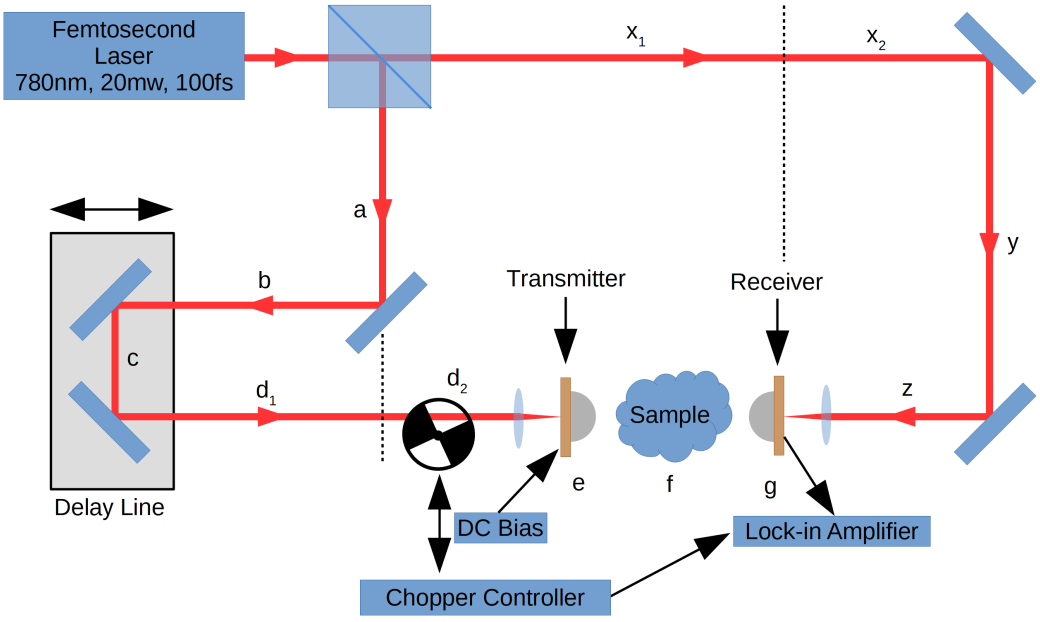

Figure 1.12: THz-TDS optical setup, see Table 1.1 for used lengths. The "Sample" could be a gas cell, chemical compound, or waveguide.

Path	a	b	c	d_1	d_2	e	f	g	x_1	x_2	y	z
Length (inches)	7	14	1	14	5	0.5	4	0.5	10	14	8	14

Table 1.1: Lengths Used During Experiments.

Figure 1.13 illustrates a THz-TDS measurement in dry (left side) and humid (right side) air. Note that water vapor in humid air appears as dips in the absorption spectrum (Fig. 1.13b). The motorized delay line is translated and the lock-in amplifier is sampled to obtain the temporal response (Fig. 1.13a). Figure 1.13b is obtained by applying the Discrete Fourier Transform (DFT) to the data in Fig. 1.13a. The difference between $E_{samp}(\omega)$ and $E_{ref}(\omega)$ can be calibrated to measure the complex permittivity of the sample resulting in data similar to Fig. 1.2.

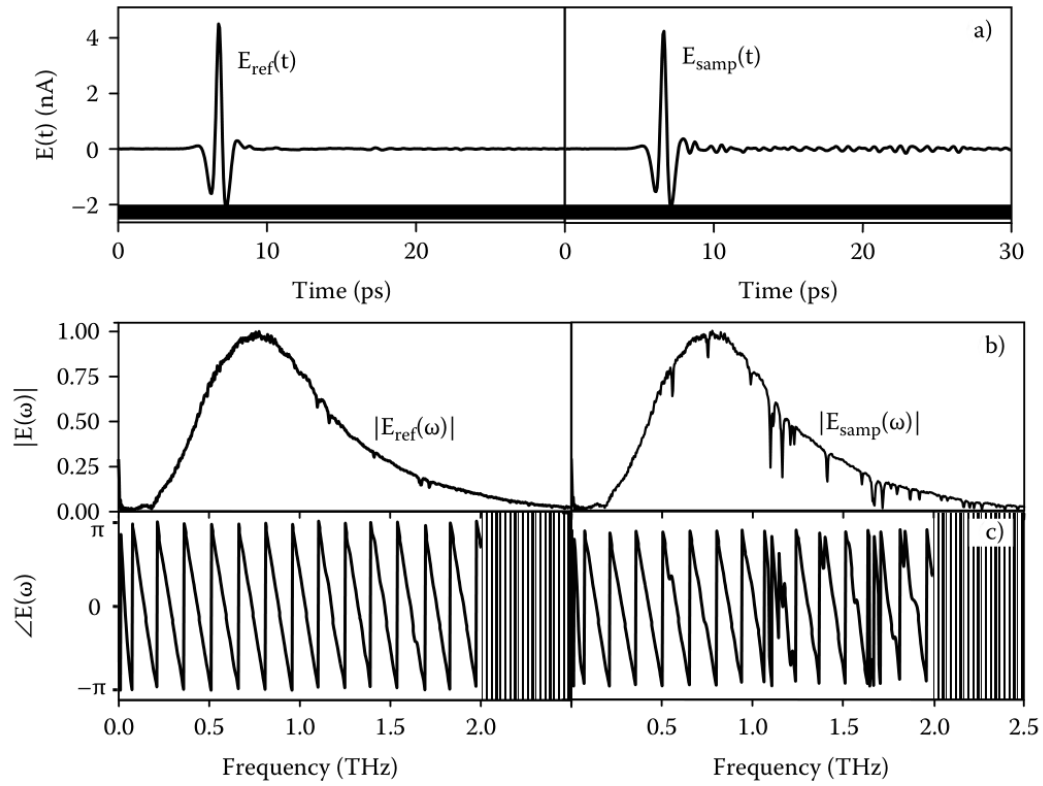

Figure 1.13: The reference and samples pulses are shown in (a) for dry and humid air. Numerical Fourier transforms of the amplitude and phase, (b) and (c), respectively, illustrate the effect of the sample on the plane wave components that comprise the THz pulse. Reproduced by permission from [24]. © 2008 Taylor & Francis Group, LLC.

1.5 Maxwell's Equations

Maxwell's equations describe the relationship between the electric and magnetic field in a medium (and source terms). In phasor form they are given by [25]:

$$\nabla \times \bar{E} = -j\omega\mu\bar{H}, \tag{1.14a}$$

$$\nabla \times \bar{H} = j\omega\varepsilon\bar{E} + \bar{J}, \tag{1.14b}$$

$$\nabla \cdot \bar{D} = \rho, \tag{1.14c}$$

$$\nabla \cdot \bar{B} = 0, \tag{1.14d}$$

the constitutive relations which describe the impact of the medium are given by:

$$\bar{D} = \varepsilon \bar{E}, \tag{1.15a}$$

$$\bar{B} = \mu \bar{H}, \tag{1.15b}$$

where $\bar{E}$ is the electric field (V/m), $\bar{D}$ is the electric flux density (C/m^2), $\bar{H}$ is the magnetic field (A/m), $\bar{B}$ is the magnetic flux density (Wb/m^2), $\bar{J}$ is the electric current density (A/m^2), ρ is the electric charge density (C/m^3). The sources of electromagnetic fields are $\bar{J}$ and ρ.

Source-free ($\bar{J} = \rho = 0$) electromagnetic field propagation is described by solving Eqn. (1.14a) or (1.14b). This well-known procedure is accomplished by taking the curl of either equation, then using the vector identity $\nabla \times \nabla \times \bar{A} = \nabla(\nabla \cdot \bar{A}) - \nabla^2 \bar{A}$ [25]:

$$\nabla \times \bar{E} = -j\omega\mu\bar{H}, \tag{1.16a}$$

$$\nabla \times \nabla \times \bar{E} = -j\omega\mu\nabla \times \bar{H}, \tag{1.16b}$$

$$\nabla(\nabla \cdot \bar{E}) - \nabla^2 \bar{E} = -j\omega\mu(j\omega\varepsilon\bar{E}), \tag{1.16c}$$

$$\nabla^2 \bar{E} + k^2 \bar{E} = 0, \tag{1.16d}$$

where Eqn. (1.16d) is the Helmholtz equation and k is the wavenumber given by: $k = \omega\sqrt{\mu\varepsilon}$, ω is the angular frequency, μ is the permeability, ε is the permittivity. As a example where E is uniform and linearly-polarized normal ($\hat{x}$ or $\hat{y}$) to the propagation direction ($\hat{z}$), then $\bar{E} = E_x\hat{x} + E_y\hat{y} + E_z\hat{z} = E_x\hat{x}$:

$$\nabla^2 E_x + k^2 E_x = 0, \tag{1.17a}$$

$$\frac{\partial^2 E_x}{\partial z^2} + k^2 E_x = 0, \tag{1.17b}$$

which has the following solution:

$$E_x = E^+ e^{-jkz} + E^- e^{+jkz}, \tag{1.18}$$

which states that E_x consists of two waves of amplitudes E^+ and E^- traveling in the $+z$ and $-z$ directions, respectively. Once either $\bar{E}$ or $\bar{H}$ is known then the other can be solved using Eqn. (1.14a) or (1.14b) (again source-free).

1.6 Pulse Propagation

Electromagnetic pulse propagation is an important concept which is relevant to THz-bandwidth systems. Pulse propagation is impacted by many factors but mainly material properties and waveguide geometry. Electric field propagation is described in the frequency domain by the following equation:

$$\hat{E}_{out}(\omega) = e^{-jk(\omega)z}\hat{E}_{in}(\omega) \tag{1.19}$$

where $\hat{E}_{in}(\omega)$ and $\hat{E}_{out}(\omega)$ are the Fourier transforms of the input and output pulses, respectively, z is the propagation distance, ω is the angular frequency, $k(\omega)$ is the wavenumber, and $j = \sqrt{-1}$.

Complications associated with field propagation are introduced by $k(\omega) = \beta(\omega) - j\alpha(\omega)$ where $\beta(\omega)$ is the phase constant and $\alpha(\omega)$ is the attenuation constant. For a plane wave in a lossless vacuum system $\beta(\omega) = \omega/c$ and $\alpha(\omega) = 0$ where c is the speed of light. With these substitutions the output is given by:

$$\hat{E}_{out}(\omega) = e^{-j\omega z/c}\hat{E}_{in}(\omega) \tag{1.20}$$

which means the output is a time-shifted copy of the input (Fourier transform properties), which is an ideal scenario for many applications. This scenario is not possible throughout the entire electromagnetic spectrum due to realistic material properties. In the non-ideal plane wave scenario, the phase constant in a material is given by $\beta(\omega) = \omega\sqrt{\varepsilon(\omega)\mu(\omega)}$, where $\varepsilon(\omega) = \varepsilon_0\varepsilon_r(\omega)$ is the complex permittivity and $\mu(\omega) = \mu_0\mu_r(\omega)$ is the complex permeability. The vacuum permittivity and permeability are given by $\varepsilon_0 \approx 8.8542 \times 10^{-12}$ F/m and $\mu_0 = 4\pi \times 10^{-7}$ H/m, respectively. The frequency dependence and complex nature (lossy) of $\varepsilon(\omega)$ and $\mu(\omega)$ modify Eqn. (1.20) such that the output is no longer a simple time shift of the input. For the remainder of this thesis we do not investigate magnetic materials, thus it is assumed $\mu_r(\omega) = 1$. Figure 1.14 illustrates a general form of $\varepsilon_r(\omega) = \varepsilon_r'(\omega) - j\varepsilon_r''(\omega)$ from Direct Current (DC) to the Ultra Violet (UV) portion of the electromagnetic spectrum. From Fig. 1.14 it is clear that the dielectric function becomes more complicated above 1 GHz.

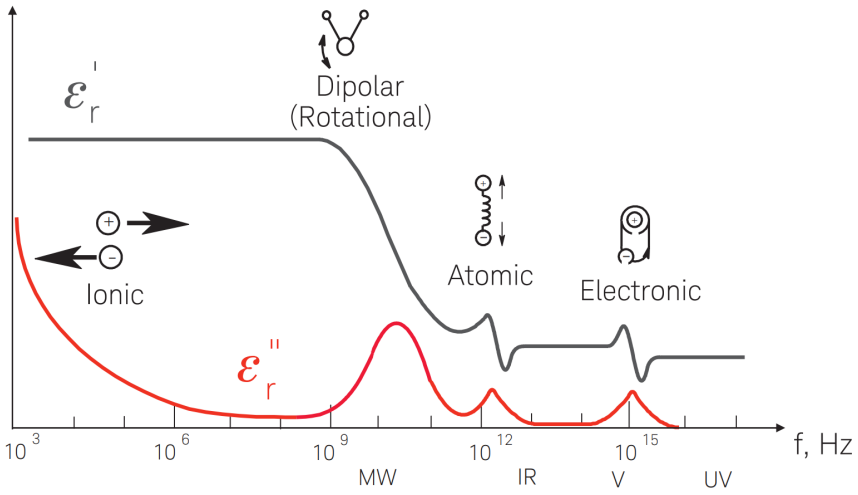

Figure 1.14: Frequency response for dielectric mechanisms. Ionic and dipole relaxation are prominent at the sub-THz region. In and above the THz region atomic and electronic resonant polarization effects are observed [26].

1.6.1 Attenuation

Attenuation occurs through a number of mechanisms; however, imperfect conductors (such as gold) and dielectrics (such as GaAs) always introduce some attenuation, α_c and α_d, respectively. Referring to Eqn. (1.19), attenuation (or possibly gain) is introduced by the imaginary part of $k(\omega)$. A propagating wave is given by:

$$\hat{E}_{out}(\omega) = e^{-j\beta(\omega)z} e^{-\alpha(\omega)z} \hat{E}_{in}(\omega), \tag{1.21}$$

which indicates that the output will be attenuated for $\alpha(\omega) > 0$. The overall attenuation coefficient, $\alpha(\omega) = \alpha_c(\omega) + \alpha_d(\omega)$, is given in Nepers (Nps) per unit length which implies a reduction in the field amplitude by 1/e at that distance. For example, if $\alpha(\omega) = 1.1513$ cm^{-1} then the field amplitude will be reduced by a factor of 0.3679 after propagating for 1.1513^{-1} cm. The attenuation constant is commonly used to discuss the power attenuation which is proportional to the square of the field. In this context attenuation coefficient can be multiplied by 10 log $e^2 = 8.686$ dB/Np to express the power loss in terms dB per unit distance. For example $\alpha(\omega) = 1.1513$ cm^{-1} $\times$ 8.686 dB/Np = 10 dB/cm, therefore the power will be multiplied by 0.1 every cm which corresponds to $e^{-2\times 1.1513\text{cm}^{-1}\times 1\text{cm}} = 0.1$.

The attenuation coefficient for a specific structure is calculated from the power

loss per unit length, P_l, which is obtained by recognizing that [25]:

$$P(z) = P_0 e^{-2\alpha z}, \tag{1.22}$$

where P_0 is the input power and therefore:

$$P_l(z) = -\frac{\partial P(z)}{\partial z} = 2\alpha P_0 e^{-2\alpha z} = 2\alpha P(z) \quad \rightarrow \quad \alpha = \frac{P_l(z=0)}{2P_0}, \tag{1.23}$$

note that α could relate to the conductor and dielectric attenuation (next Sections).

Dielectric Loss

Dielectric loss is introduced by the imaginary part of the dielectric function, $\varepsilon(\omega) = \varepsilon'(\omega) - j\varepsilon''(\omega)$. It is common to specify the dielectric loss tangent, $\tan\delta_\varepsilon = \varepsilon''(\omega)/\varepsilon'(\omega)$ to characterize the dielectric loss. Using this definition, the dielectric function can be expressed in terms of the loss tangent:

$$\varepsilon(\omega) = \varepsilon'(\omega)[1 - j\tan\delta_\varepsilon(\omega)] = \varepsilon_0\varepsilon_r(\omega)[1 - j\tan\delta_\varepsilon(\omega)]. \tag{1.24}$$

To calculate the dielectric attenuation coefficient for a specific guiding structure the transverse electric ($\bar{E}$) and magnetic field ($\bar{H}$) profiles must be known. First the input power, P_0, must be calculated by integrating the Poynting vector:

$$P_0 = \frac{1}{2}\mathrm{Re}\int_S \bar{E} \times \bar{H}^* \cdot d\bar{s}, \tag{1.25}$$

then the dielectric power loss and attenuation coefficient per unit length is given by [25]:

$$P_{ld} = \frac{\omega\varepsilon''(\omega)}{2}\int_V |\bar{E}|^2 ds, \quad \rightarrow \quad \alpha_d = \frac{P_{ld}}{2P_0}, \tag{1.26}$$

where the integration occurs over the dielectric area in the transverse plane ($\hat{x}$, $\hat{y}$) and up to a unit distance in the propagation direction ($\hat{z}$). The dielectric attenuation coefficient will typically take the following form:

$$\alpha_d(\omega) \propto \omega\varepsilon''(\omega)Z_0(\omega) \tag{1.27}$$

where $Z_0(\omega)$ is the characteristic impedance of the specific guiding structure.

Conductor Loss

Conductor loss describes attenuation associated with field propagation along a conductor with finite conductivity. A key parameter in determining the conductor loss is the surface resistance, R_s. The surface resistance originates because high frequency waves are unable to propagate deeply into a conductor. The skin depth characterizes the penetration depth and is given by:

$$\delta_s = \sqrt{\frac{2}{\omega\mu(\omega)\sigma}}, \tag{1.28}$$

where σ is the conductivity of the metal. Figure 1.15a plots the skin depth for a few common metals where it is clear that submicrometer skin depths are expected in the THz range. The shallow skin depth implies the majority of the power will propagate near the conductor surface. Once the skin depth is known the surface resistance (Fig. 1.15b) is calculated by:

$$R_s(\omega) = \frac{1}{\sigma\delta_s(\omega)}. \tag{1.29}$$

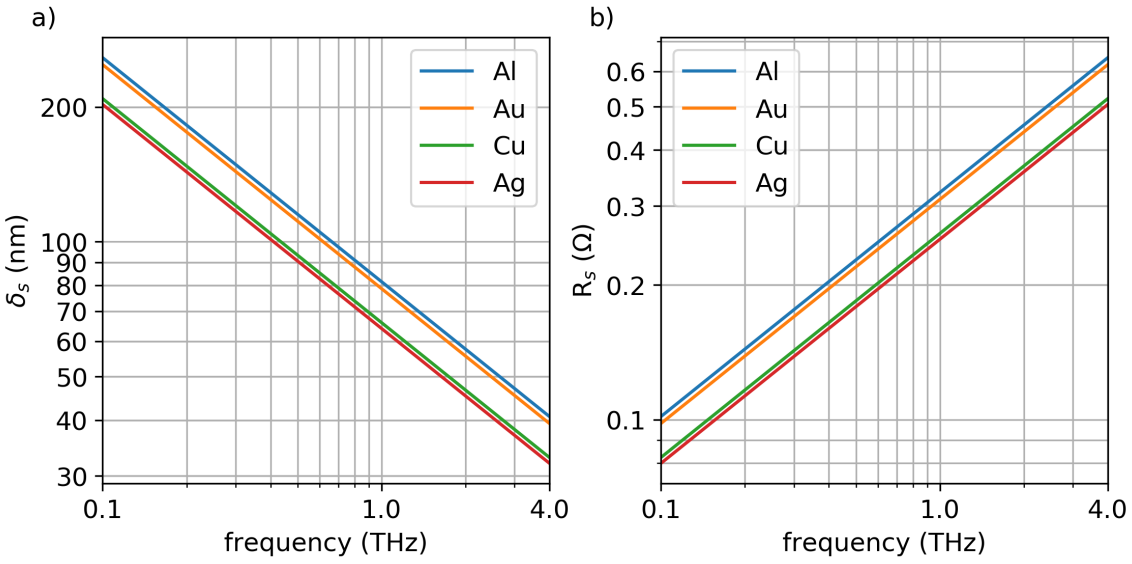

Figure 1.15: Skin depth and surface resistance in the THz range for a few common metals.

The conductor attenuation coefficient is obtained using a similar method to the

dielectric attenuation coefficient, Eqn. (1.26), and is calculated by [25]:

$$P_{lc} = \frac{R_s(\omega)}{2} \int_S |\bar{H}_t|^2 ds, \quad \rightarrow \quad \alpha_c = \frac{P_{lc}}{2P_0}. \tag{1.30}$$

where the integration occurs over the conductor surface in the transverse plane ($\hat{x}$, $\hat{y}$) and up to a unit distance in the propagation direction ($\hat{z}$). The conductor attenuation coefficient will typically take the following form:

$$\alpha_c(\omega) \propto \frac{R_s(\omega)}{Z_0(\omega)}, \tag{1.31}$$

noting that $R_s(\omega) \propto \omega^{1/2}$ the conductor loss will increase with this frequency dependence.

Leaky-wave Radiation Loss

THz systems are susceptible to leaky-wave radiation loss which can greatly exceed dielectric or conductor loss. This loss occurs when a field propagates along a mismatched dielectric interface. This concept is best characterized by difference in group and phase velocity for pulse propagation, however it can be intuitively described by Snell's law (Fig. 1.16):

$$n_1 \sin(\theta_1) = n_2 \sin(\theta_2), \tag{1.32}$$

where n_1 and n_2 are the refractive indexes of the two mediums, θ_1 is the incident angle, and θ_2 is the refracted angle. Leaky-wave radiation is similar to setting the incident angle to $\theta_1 = 90^\circ$ which results in a refracted angle of:

$$\theta_2 = \sin^{-1}\left(\frac{n_1}{n_2}\right), \tag{1.33}$$

assuming a typical THz scenario where $n_1(\text{air}) = 1$ and $n_2(\text{LTG-GaAs}) \approx \sqrt{13}$, this corresponds to $\theta_2 = 16.1^\circ$. This small angle means that a very small portion of power propagates near the dielectric-air interface. It is desirable for θ_2 to be close to 90° which would minimize radiation.

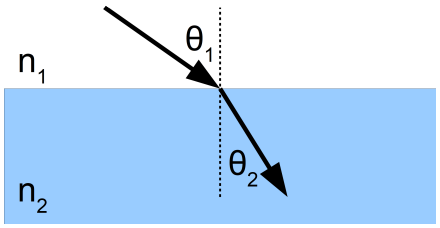

Figure 1.16: Snell's law illustration. Incident ray in medium 1 (n_1) with angle θ_1 with respect to surface normal. Refracted ray in medium 2 (n_2) with angle θ_2 with respect to surface normal.

Less intuitively leaky-wave radiation is described by the difference between the wavenumber of the propagating field and radiated field in the substrate [27]. Figure 1.17 illustrates this concept for a Coplanar Strip (CPS) waveguide. As a quasi-static approximation, a transmission line on the dielectric interface will have a quasi-Transverse Electromagnetic (TEM) mode with a phase constant given by:

$$\beta_{\text{qTEM}}(\omega) = \omega\sqrt{\varepsilon_{r,eff}\varepsilon_0\mu_0}, \tag{1.34}$$

where $\varepsilon_{r,eff} \approx (\varepsilon_{r,1} + \varepsilon_{r,2})/2$, $\varepsilon_{r,1}$ and $\varepsilon_{r,2}$ are the relative dielectric constants for the two materials. For a GaAs-air interface this corresponds to $\varepsilon_{r,eff} = (1 + 13)/2 = 7$. The propagation constant in the substrate is given by:

$$\beta_{\text{sub}}(\omega) = \omega\sqrt{13\varepsilon_0\mu_0}, \tag{1.35}$$

The semicone of radiation emits at an angle, ψ, which is calculated by [27]:

$$\psi = \cos^{-1}\left(\frac{\beta_{\text{qTEM}}}{\beta_{\text{sub}}}\right) = \cos^{-1}\left(\frac{\sqrt{7}}{\sqrt{13}}\right) = 42.8°. \tag{1.36}$$

This angle is close to what was calculated using Eqn. (1.16) which assumed the incident ray existed in air only ($n_1 = 1$). If the average ($n_1 = \sqrt{(1 + 13)/2}$) was selected the two results would be identical.

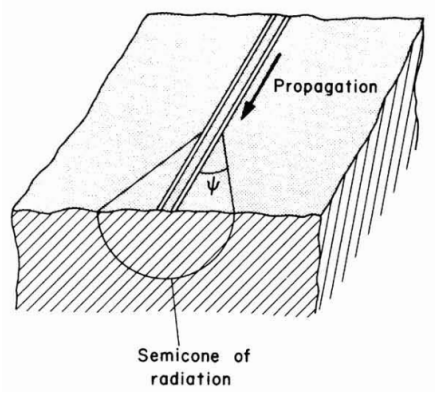

Figure 1.17: Leaky-wave radiation for a CPS waveguide. Reprinted by permission from [28]. © 1983 IEEE.

The leaky-wave radiation loss is dependent on the waveguide geometry, dielectric mismatch, and frequency. For example the leaky-wave radiation loss for a CPS waveguide is given by [29]:

$$\alpha_{\text{rad}}^{\text{cps}} = \pi^5 \left(\frac{3-\sqrt{8}}{2}\right) \sqrt{\frac{\varepsilon_{eff}(f)}{\varepsilon_r}} \left(1 - \frac{\varepsilon_{eff}(f)}{\varepsilon_r}\right)^2 \frac{(S+2W)^2 \varepsilon_r^{3/2}}{c^3 K'(k) K(k)} f^3, \tag{1.37}$$

where $\varepsilon_{eff}(f)$ is the frequency-dependent effective relative permittivity for the guided field, ε_r is the relative permittivity for the substrate, S is the separation between the two conductors, W is the width of the conductors, c is the speed of light, $k = S/(S+2W)$, $K(k)$ is the complete elliptic integral of the first kind, $K'(k) = K(\sqrt{1-k^2})$, and f is the frequency.

An important observation is that the leaky-wave radiation loss scales cubically, i.e. f^3; however, $\varepsilon_{eff}(f)$ modifies this dependency such that [29]:

$$\alpha_{\text{rad}}^{\text{cps}} \propto f^n, \quad \text{where } n = 2 - 3. \tag{1.38}$$

Figure 1.18 shows the results of a time domain simulation (using ANSYS HFSS) which illustrates leaky wave radiation for a CPS transmission line (similar to Fig. 1.17). The transmission line was excited with a short Gaussian pulse (FWHM = 0.5 ps) and the field (Fig. 1.18) was plotted 1.5 mm away from the source. The CPS conductors were Perfect Electric Conductors (PECs) and the dielectrics were lossless air ($n_1 = 1$) and GaAs ($n_2 = 3.59$). The difference in radiation angle (40° vs 42.8°) is explained by the usage of the quasi-static approximation in Eqn. (1.36). When non-quasi-static

effects are accounted for (see set of equations in [29]), the radiation angle becomes closer to 40°.

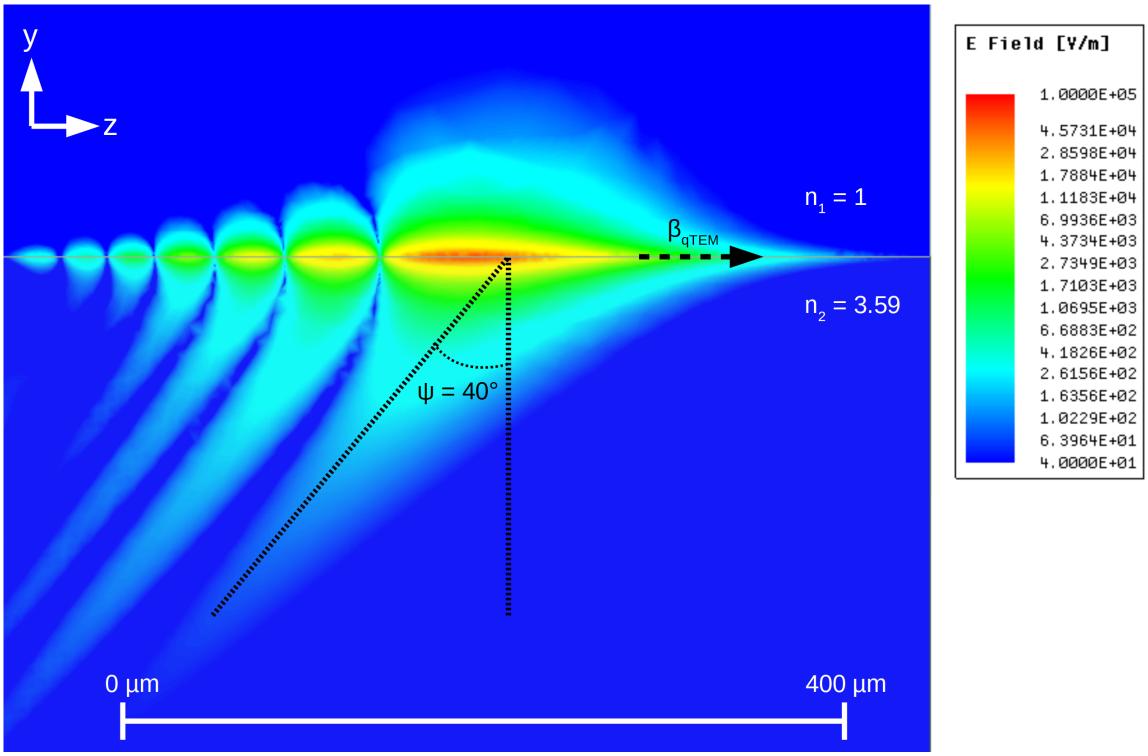

Figure 1.18: Electric field illustrating leaky-wave radiation for a short pulse traveling along a CPS transmission line on GaAs.

1.6.2 Dispersion

Dispersion characterizes a variation in field propagation velocity with respect to frequency. This could refer to either the phase, v_p, or group, v_g, velocities which are given by:

$$v_p(\omega) = \frac{\omega}{k(\omega)}, \quad v_g(\omega) = \frac{\partial \omega}{\partial k(\omega)}. \tag{1.39}$$

The phase velocity describes the propagation of a fixed phase point. The group velocity is more applicable to pulsed systems because it describes the velocity at which a wave packet propagates. For a material to be non-dispersive the phase and group velocity must be equal and constant with respect to frequency. This is true for

a material with a constant relative dielectric function where $k(\omega) = \omega\sqrt{\varepsilon_0\varepsilon_r\mu_0}$:

$$v_p(\omega) = \frac{1}{\sqrt{\varepsilon_0\varepsilon_r\mu_0}}, \quad v_g(\omega) = \frac{1}{\sqrt{\varepsilon_0\varepsilon_r\mu_0}}, \tag{1.40}$$

however any dependence on ω will introduce dispersion (i.e. $\varepsilon_r(\omega)$). The terms dispersion and Group Velocity Dispersion (GVD) are used to describe the variation in phase and group velocities with respect to frequency, respectively. Dispersion is more relevant to continuous wave systems (i.e. not short pulses systems), GVD is relevant to short pulse systems. For a system with uncompensated GVD a short pulse will broaden.

Pulse Propagation in a Lossy Dispersive Medium

The simple Debye relaxation model is used to illustrate the impact of a non-ideal dielectric (such as water) on pulse propagation [3]. Debye relaxation is described by:

$$\varepsilon(\omega) = \varepsilon(\infty) + \frac{\varepsilon(0) - \varepsilon(\infty)}{1 + j\omega\tau_d}, \tag{1.41}$$

where ω is the angular frequency, $\varepsilon(\infty)$ is the high frequency limit of the dielectric function, $\varepsilon(0)$ is the DC value for the dielectric function, τ_d is the Debye relaxation time, and $j = \sqrt{-1}$.

For illustrative purposes Fig. 1.19 plots plane wave pulse pulse propagation for a non-magnetic Debye material, $\mu_r(\omega) = 1$, $\varepsilon_r(0) = 13$, $\varepsilon_r(\infty) = 11$, the Debye relaxing time is varied $\tau_d = 1$ ps, 10 ps, 100 ps, and 1000 ps. Figure 1.19(a-b) plots the real and imaginary parts of the dielectric function. Figure 1.19c plots the input (Gaussian FWHM = 0.5 ps) and output (1 cm away) pulses for a selection of τ_d. Figure 1.19d plots the spectral attenuation for the pulses shown in Fig. 1.19c. From Fig. 1.19(c-d) it is clear that the output pulse can become significantly attenuated depending on the value of τ_d.

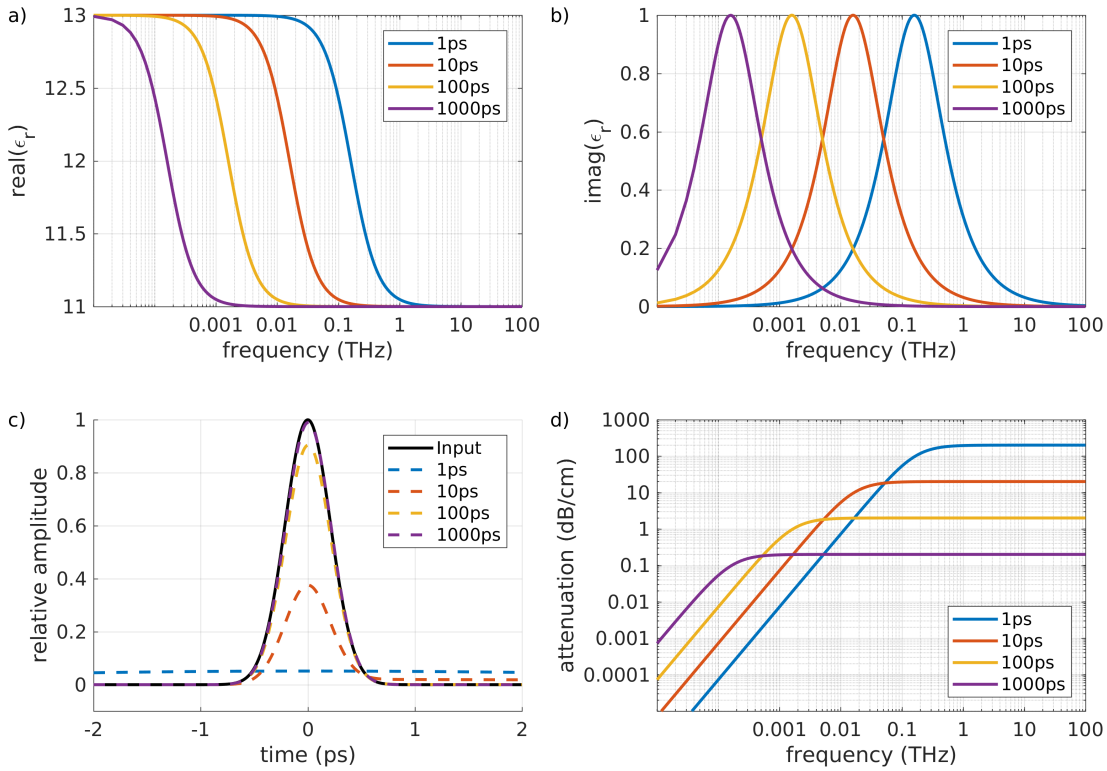

Figure 1.19: Pulse transmitted 1 cm with Debye $\varepsilon(\omega)$.

Waveguide Dispersion

Apart from material properties, waveguide geometry impacts $k(\omega)$. For a simple two-conductor free-space transmission line where the conductor geometry and spacing is small compared to the guided wavelength only a single TEM mode will exist ($E_z = H_z = 0$). This results in an identical wavenumber to the free-space plane wave case, $k(\omega) = \omega/c$. Deviations from this case will result in modifications of the wavenumber. To illustrate this concept pulse propagation along a common THz waveguide, the free-space Parallel-Plate Waveguide (PPWG), is shown for a few Transverse Magnetic (TM) ($H_z = 0$) modes. Figure 1.20 illustrates the geometry of a PPWG.

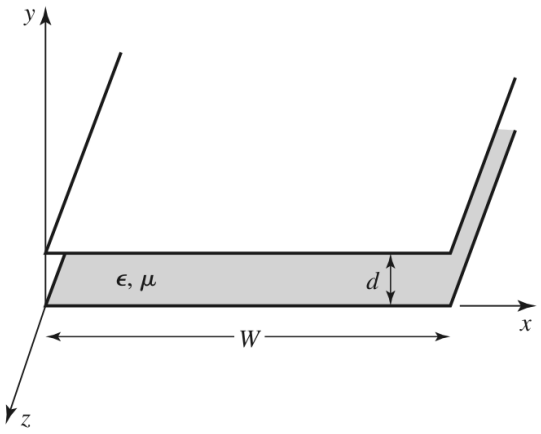

Figure 1.20: PPWG geometry. Reprinted by permission from [25]. © 2012, 2005, 1998 John Wiley & Sons, Inc.

The phase constant, $\beta(\omega)$, for TM_n modes in a PPWG is given by:

$$\beta_n(\omega) = \sqrt{k_n^2(\omega) - k_{c,n}^2}, \tag{1.42}$$

where $k_{c,n}$ is the cut-off wavenumber which is given by $k_{c,n} = n\pi/d$ (for a PPWG), n is the specified mode, and d is the plate separation. From Eqn. (1.42) it is seen that $k_n^2(\omega)$ must be greater than $k_{c,n}^2$ for $\beta_n(\omega)$ to be real valued. This means that a specific mode can only propagate at frequencies above the cut-off frequency (or wavenumber) which is defined by the waveguide geometry. Here we will illustrate propagation of the $\hat{y}$ component of the electric field which is calculated from the longitudinal portion of the electric field given by:

$$E_{z,n} = \sin\left(\frac{n\pi y}{d}\right) e^{-j\beta_n(\omega)z}, \tag{1.43}$$

from $E_{z,n}$, $E_{y,n}$ can be calculated as:

$$E_{y,n} = \frac{-j\beta_n(\omega)}{k_{c,n}^2}\frac{\partial E_{z,n}}{\partial y} = \frac{-j\beta_n(\omega)}{k_{c,n}}\cos\left(\frac{n\pi y}{d}\right) e^{-j\beta_n(\omega)z}. \tag{1.44}$$

Note that for $n = 0$ then $E_{z,0} = 0$ which means that both $H_z = 0$ and $E_z = 0$ which is the definition for a TEM wave, therefore Eqn. (1.44) is not applicable. For $n = 0$

the $\hat{y}$ component of the electric field is given by:

$$E_{y,0} = -\frac{V_0}{d} e^{-jk(\omega)z}, \tag{1.45}$$

where V_0 is the potential difference between the two plates.

In Eqn. (1.44) the transverse y-dependence is contained within the cosine term and varies between -1 and 1. To provide a consistent demonstration of the impact on the temporal pulse we will look at the maximum value (i.e. set the cosine term to 1):

$$E_{y,n} = \frac{-j\beta_n(\omega)}{k_{c,n}} e^{-j\beta_n(\omega)z}. \tag{1.46}$$

Figure 1.21a plots the normalized (and time shifted) pulses for the first four TM_n modes after propagating in PPWG for 10 cm where $d = 300$ μm. The input pulse is Gaussian shaped with FWHM = 0.5 ps. Figure 1.21b plots the relative unnormalized spectral power for each of the modes. The cut-off frequency for modes in a free-space PPWG are calculated by:

$$f_{c,n} = \frac{n}{2d\sqrt{\varepsilon_0 \mu_0}}, \tag{1.47}$$

which results in: $f_{c,0} = 0$ Hz, $f_{c,1} = 0.5$ THz, $f_{c,2} = 1.0$ THz, and $f_{c,3} = 1.5$ THz. These cut-off frequencies are seen in Fig. 1.21b where the spectral power for each $\mathrm{TM}_{n>0}$ mode sharply decreases.

Figure 1.21b illustrates that $\mathrm{TM}_{n>0}$ modes broaden significantly and heavily oscillate due to significant dispersion near the cut-off frequency. For broadband pulse propagation these higher order modes are typically not beneficial and best to avoid. For a PPWG this can be accomplished by ensuring the cut-off frequency of the TM_1 mode is larger than the highest detectable signal frequency.

Figure 1.21c plots the phase and group velocity normalized to the speed of light for the PPWG ($d = 300$ μm). This plot illustrates that modes fail to propagate ($v_g \to 0$) below their cut-off frequency. The strong variation in phase and group velocity near the cut-off frequency indicates dispersion. From Fig. 1.21c (for the $\mathrm{TM}_{n>0}$ modes) the group velocity increases with frequency, thus higher frequency components propagate faster indicating normal (non-anomalous) dispersion. Inspection of the TM_1 modes leading edge in Fig. 1.21a clearly shows that higher frequencies travel faster. The superluminal phase velocity is expected as it is a measure of the bouncing phase front along the propagation axis, but no information is propagating at this velocity.

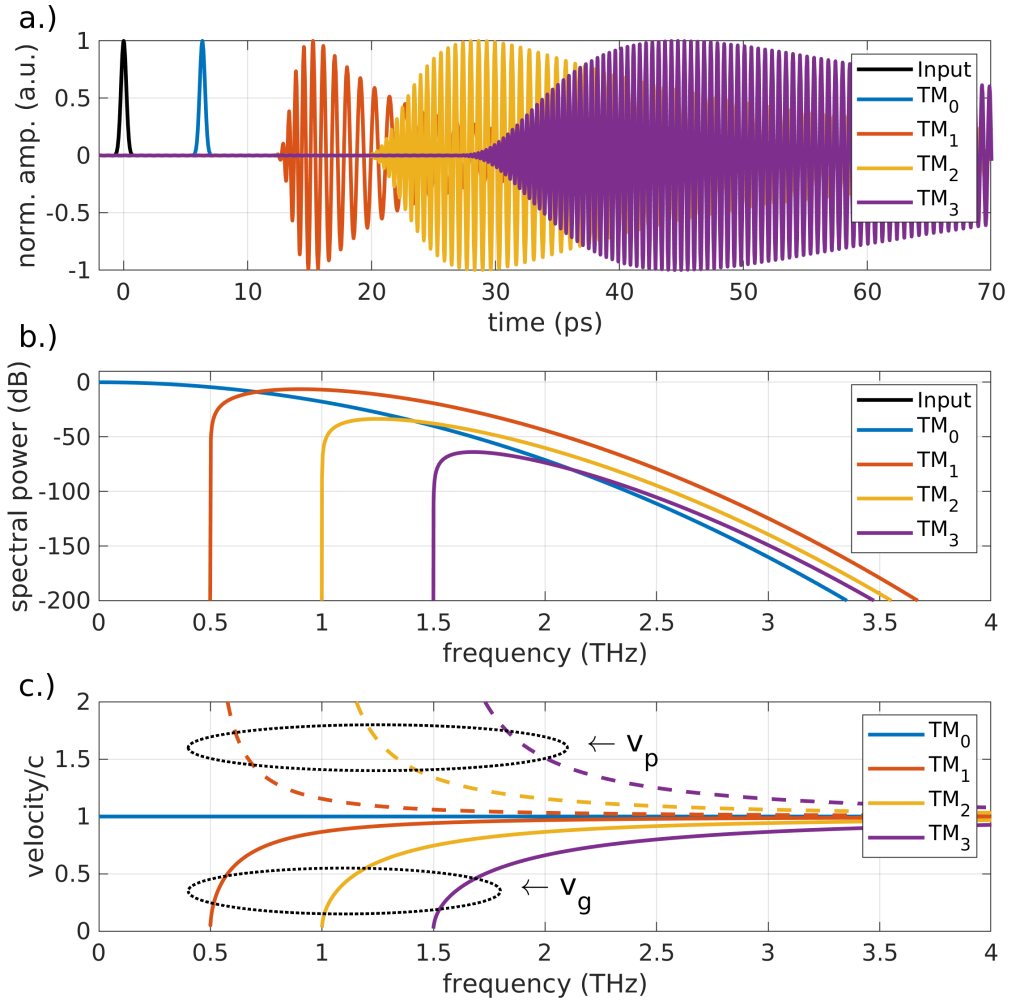

Figure 1.21: PPWG characterization ($d = 300\ \mu$m). a.) Temporal response at output of a 1 cm long PPWG with input pulse width FWHM = 0.5 ps. b) Spectral response for the pulses. c) Relative phase and group velocity for $d = 300\ \mu$m waveguide geometry, c = 3×10^8 m/s.

1.7 THz Field Guiding Technologies

To retain signal strength and integrity low-loss waveguides with minimal dispersion are desired throughout the electromagnetic spectrum. At low frequencies, <10 GHz, twisted-pair conductors, coaxial cables, or waveguides can provide this functionality. At much higher frequencies, >100 THz, optical fibers can be used. As previ-

ously discussed a common method for generating a THz-bandwidth signal is called PC switching which generates an electric field with a broad spectrum of frequencies (i.e. 100 GHz $\rightarrow$ 4 THz). Given that our THz sources utilize PCA switching we limit our focus to this range.

A number of broadband THz waveguides currently exist, each with its own benefits and drawbacks. The main waveguiding technologies in the THz region are the PPWG [30], Sommerfeld wire [31], Two-Wire Waveguide (TWWG) [32], CPS transmission lines [29], Metallic-Slit Waveguide (MSWG) [33], Plastic Photonic Crystal Fiber (PPCF) [34], and the ribbon waveguide [35]. The following subsections give a brief description of each and summarize the advantages and disadvantages. To remain consistent, all the quoted attenuation coefficients are obtained around 0.5 THz because this is the upper limit to some of cited experimental results.

1.7.1 Parallel-Plate Waveguide

The PPWG was previously illustrated in Fig. 1.20 when discussing waveguide dispersion. With proper design a PPWG provides low loss and minimal dispersion in the THz region. The inset of Fig. 1.22a depicts a common excitation method for PPWGs. The electric field generated by a photoconductive switch is coupled in and out of the PPWG using high resistivity silicon plano-cylindrical lenses. Figure 1.22a plots the detected THz-bandwidth pulse after propagating for 22.4 mm in a PPWG (plate separation = 108 μm) [30]. Figure 1.22b plots the spectral response of the received pulse. The dotted line is the reference spectrum without PPWG, for this measurement the silicon lenses were arranged in a confocal configuration. The solid line is with a 22.4 mm PPWG in place (as shown in the inset). Introduction of the PPWG attenuates the spectrum by a relatively minor amount which demonstrates that the PPWG performs admirably in the THz region. The first higher order mode, TM_1 ($f_{c,1}$ = 1.4 THz) is not excited because of its odd mode profile, the second TM_2 ($f_{c,2}$ = 2.8 THz) mode is attenuated more than the TM_0 mode thus GVD is not observed [30].

The main disadvantage for the PPWG relates to system integration. At minimum two high resistivity silicon lenses are required (four if using a PCA transmitter and receiver) and THz alignment is required at each of these lenses which is a sensitive procedure.

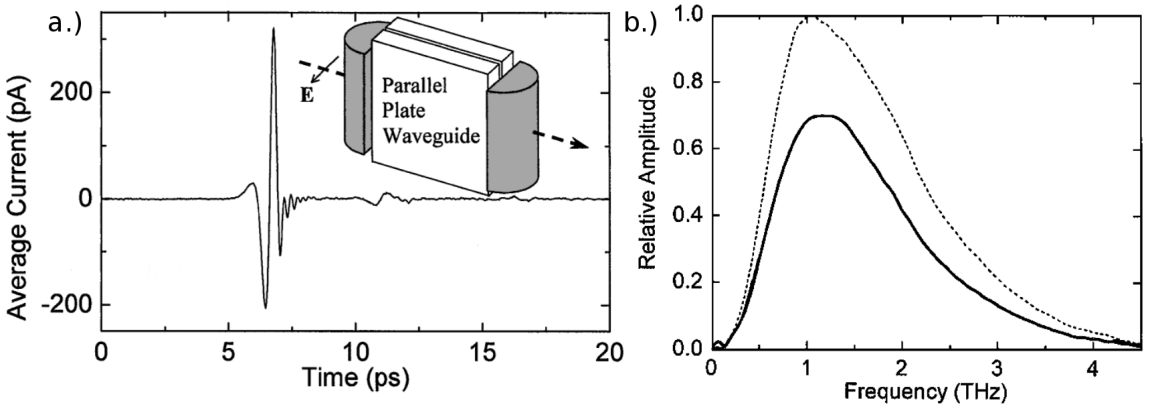

Figure 1.22: Experiment results for PPWG. a) Temporal Response. b) Spectral response, the dotted line is the reference without PPWG with the silicon lenses placed in a confocal configuration. The solid line is with 22.4 mm long PPWG in place (as shown in the inset). Reprinted by permission from [30]. © 2001 Optical Society of America.

1.7.2 Sommerfeld Wire

A single wire can guide a THz-bandwidth pulse by coupling to the radially polarized Sommerfeld mode [31]. The Sommerfeld wave propagates with low loss and dispersion (Fig. 1.23), however it has a few detriments. First the wave is weakly bound to the conductor, thus it experiences a large bending loss [36]. Also exciting the radially polarized mode is difficult when most THz sources are typically linearly polarized. Initially the Sommerfeld wave was excited by placing an input coupler near the wire to transfer energy into the radial mode (see Fig. 1.24). Another technique was shown in [36] where the source photoconductor geometry was modified to maximize the field overlap between the generated field and the radial mode, however then other difficulties arise related to focusing the optical pump. Ultimately the usefulness of the Sommerfeld wire is limited by the substantial bend loss, however it can still be used for spectrographic applications [37].

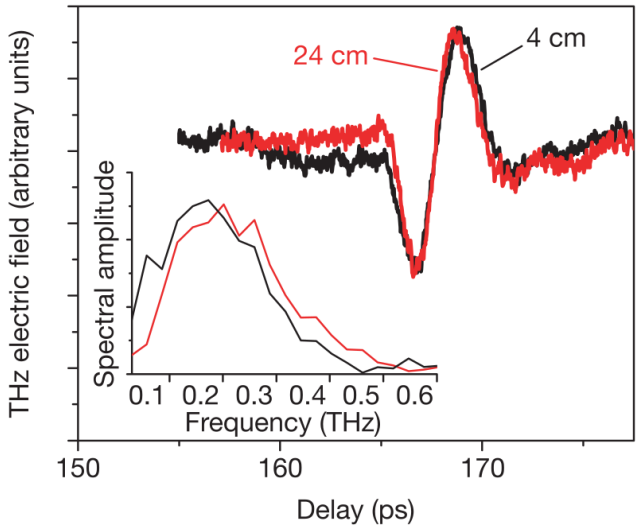

Figure 1.23: Sommerfeld wire pulses excitation and detection. Reprinted by permission from [31]. © 2004 Springer Nature.

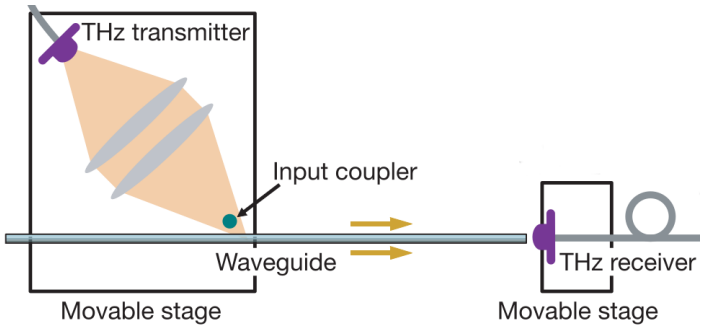

Figure 1.24: Sommerfeld wire excitation and detection experiment. Reprinted by permission from [31]. © 2004 Springer Nature.

1.7.3 Two-Wire Waveguide

The TWWG is the natural extension to the single Sommerfeld wire where another wire is added. Figure 1.25 illustrates the cross-section of the TWWG and flux distribution [38]. Theoretically a TWWG can exhibit low loss (0.001 dB/mm) and dispersion [39, 38], however there do not appear to be experimental results supporting this claim (to this degree). Regardless there are experimental results for more practical structures when the TWWG is supported by a dielectric [40, 41]. In [40] a commercial twin-pair TV-antenna cable (Fig. 1.26b) was used and an attenuation coefficient of

≈0.01 dB/mm was obtained. Figure 1.26a plots the received pulse for two different lengths (24 cm and 60 cm) where it is clear that the dielectric causes substantial pulse distortion.

In [41] the TWWG (14 cm long) was clamped in a polystyrene foam and the loss was ≈0.1 dB/mm. Figure 1.27 plots the results for the TWWG in [41] where less pulse distortion is observed likely because the surrounding dielectric is homogeneous and $\varepsilon_r \approx 1$.

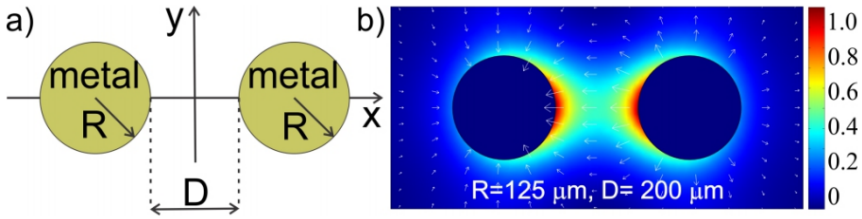

Figure 1.25: TWWG [38]. a) Cross-section. b) Flux distribution for the TEM mode of a two-wire waveguide. Arrows show vectorial distribution of the corresponding transverse electric field. Reprinted by permission from [38]. © 2013 Optical Society of America.

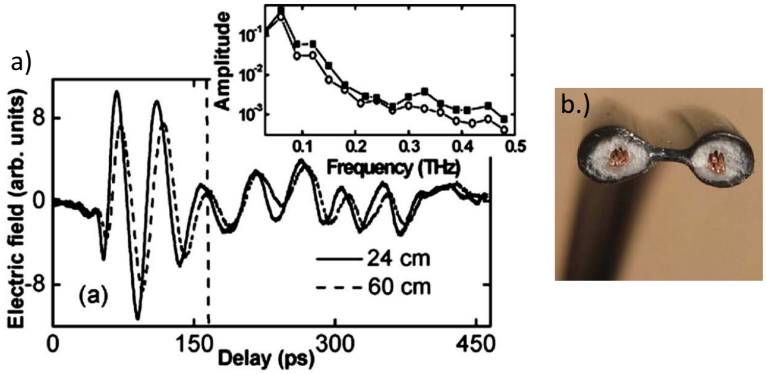

Figure 1.26: TWWG from [40]. a) Transmitted THz pulses along a 60 cm and 24 cm waveguide. The inset shows the spectral response for the pulses after truncation at the dashed line. b) Image of the twin-lead cable used for this experiment. Reprinted by permission from [40]. © 2009 AIP Publishing.

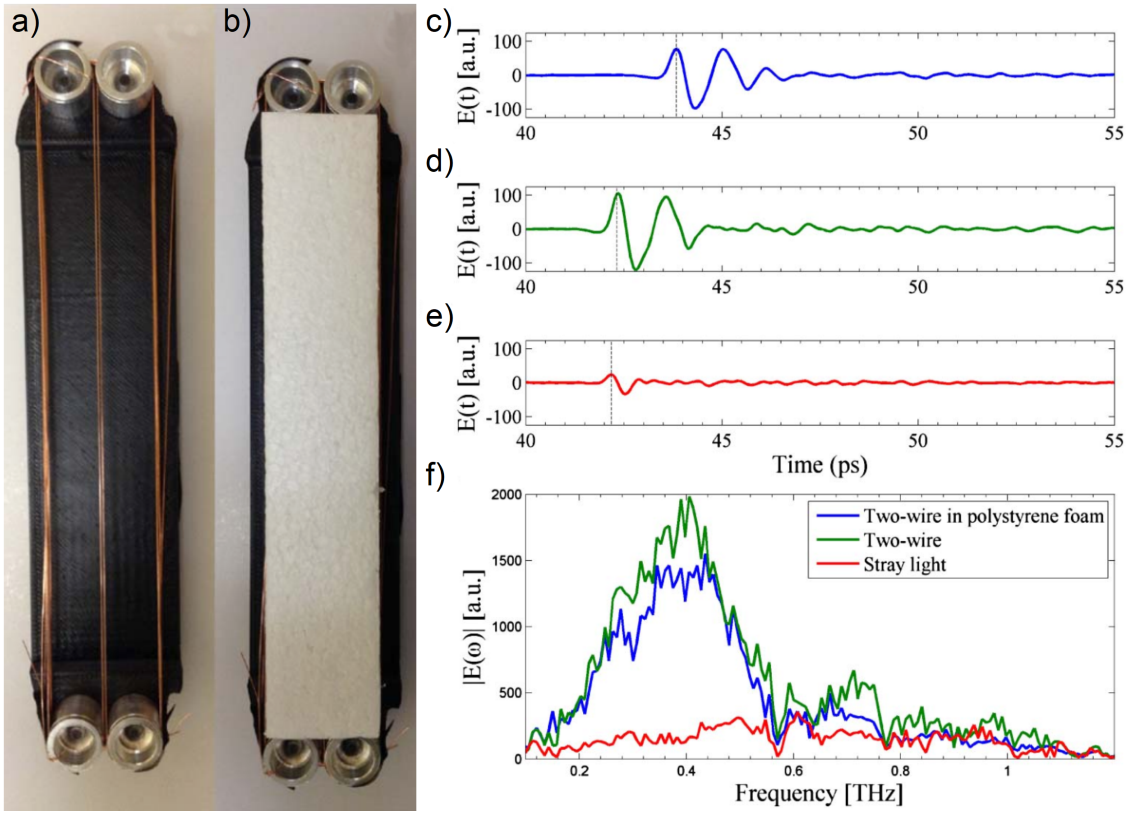

Figure 1.27: TWWG from [41]. a) Image of TWWG. b) Image of TWWG embedded in polystyrene foam. b) Detected temporal pulse with TWWG embedded in polystyrene foam. c) Detected temporal pulse with TWWG in air. e) Reference without wires. f) Transmission spectra of the corresponding electric field. Reprinted by permission from [41]. © 2014 Optical Society of America.

1.7.4 CPS Waveguide

The CPS waveguide is a planar structure which was introduced when describing leaky-waves (Fig. 1.17). CPS waveguides are a desirable technology because they are compatible with standard lithographic processing, therefore planar micrometer-scale structures are easily fabricated. The cross section for a CPS is shown in Fig. 1.28. Key detriments for the CPS waveguide are the conductor and leaky-wave losses (Fig. 1.18), note these loss mechanisms typically exceed the dielectric material loss. The loss is expressed as: $\alpha(f_0) = A_{\text{cond}} f_0^{1/2} + A_{\text{rad}} f_0^3$, where f_0 is the unitless magnitude of the frequency in THz. For example, f_0=1 corresponds to 1 THz. A_{cond} and A_{rad} the conductor and leaky-wave radiation attenuation coefficients, respectively. The cube

dependence for the leaky-wave radiation loss implies A_{rad} requires minimization. For a CPS-like structure on a Silicon-on-Sapphire (SOS) substrate the following values were obtained: $A_{\text{cond}} = 6$ cm^{-1} and $A_{\text{rad}} = 32$ cm^{-1} ($S = 15$ μm, $W = 4$ μm, $H =$ thick) [42]. This corresponds to a power loss of 7.2 dB/mm at 0.5 THz and 230 dB/mm at 2 THz. Without leaky-wave radiation ($A_{\text{rad}} = 0$ cm^{-1}) the following values are obtained: 3.7 dB/mm at 0.5 THz and 7.4 dB/mm at 2 THz which shows improvement but the total loss is still substantial.

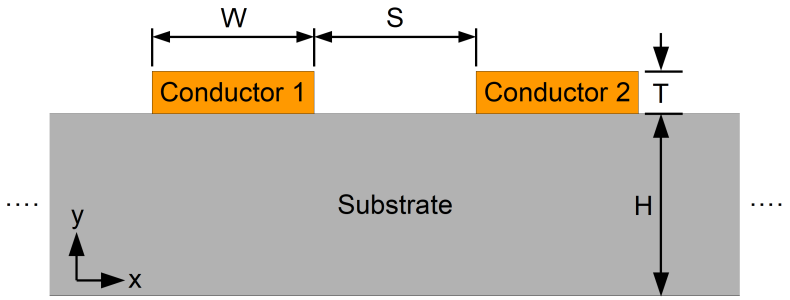

Figure 1.28: CPS cross-section.

Leaky-wave radiation losses can be mitigated by sandwiching the waveguide to make the surrounding dielectric homogeneous [27], however then optical excitation becomes difficult. Another potential solution is to reduce the conductor separation, S, and width, W, below 1 μm, however this will increase the conductor loss substantially [42]. Alternatively the substrate can be thinned (H reduced) such that the field remains localized near the conductors in free-space [27, 43]. In [43] a CPS was fabricated on a thin ($H = 1.4$ μm) membrane where $S = W = 20$ μm. The authors claim that no f^3 dependence was observed within their measurement window (up to 1 THz) which implies $A_{\text{rad}} < A_{\text{cond}}$. The experimental data in [43] does not follow a $f^{1/2}$ dependence below 1 THz (see Fig. 1.29); however, it experiences low loss, 0.4 dB/mm at 0.5 THz. This improvement over the previously estimated value (3.7 dB/mm) is likely due to different conductor geometry i.e. $S = W = 20$ μm, compared to $S = 16$ μm and $W = 4$ μm. The narrower conductor strips will have a higher resistance thus conductor loss. This concept illustrates that the waveguide geometry (S and W) can be optimized for low loss operation; however, as the cross-section ($S + 2W$) increases radiation loss increases during excitation. This concept is discussed more in Appendix C. The substrate thickness, H, was reduced to minimize the leaky-wave loss; however as the substrate enters the $H \approx 50$ μm region then

surface waves may become present within the signal bandwidth. Surface waves are the result of the pulse resonating in the substrate. As an approximation the resonance occurs at $\Delta f = 3{\times}10^8/(2nH)$. For silicon nitride ($n = 2.76$) this corresponds to $\Delta f(50\ \mu\text{m}) = 1.1$ THz, if the substrate thickness was changed to $H = 1\ \mu$m then the resonance now occurs at $\Delta f(1\ \mu\text{m}) = 54.3$ THz, thus when using very thin substrates surface waves will not be observed. To summarize, the CPS waveguide on a thin membrane is an attractive technology because experimental results demonstrate it is capable of functioning up to at least 1 THz with reasonable attenuation and very minor distortion.

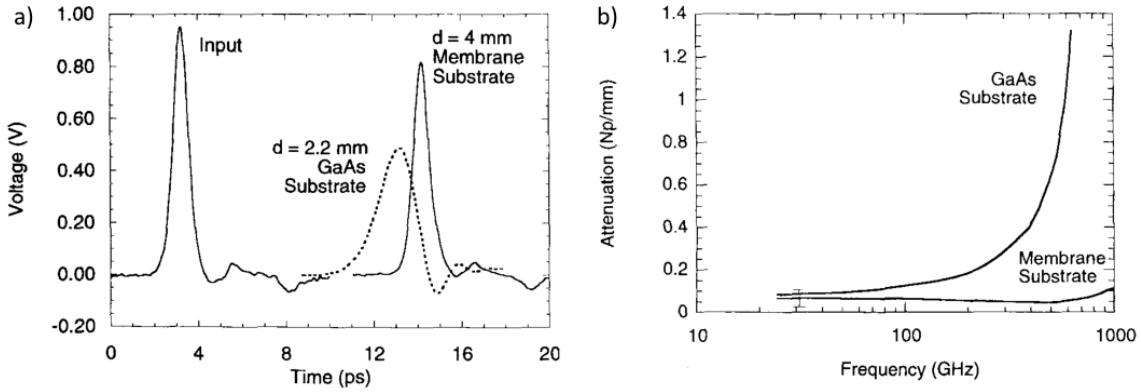

Figure 1.29: CPS experiment from [43], d is the propagation distance. a) Temporal response illustrating the pulse on membrane and GaAs substrate (for comparison). b) The attenuation coefficient for each structure. Reprinted by permission from [43]. © 1994 IEEE.

1.7.5 Metallic-Slit Waveguide

The MSWG resembles a CPS waveguide (Fig. 1.28) except it is wider ($W >> S$) and thicker ($50\ \mu\text{m} < T < 300\ \mu$m). Figure 1.30 illustrates the cross-section of a MSWG. The increased thickness improves the mechanical strength (compared to a CPS waveguide on a thin substrate) and the guiding region can be suspended in free-space (when supported by the outer edges). Suspension in free-space eliminates the previously discussed leaky-wave radiation because the surrounding dielectric is homogeneous. The conductor loss for the MSWG is reduced because of the relatively large conductor surface area.

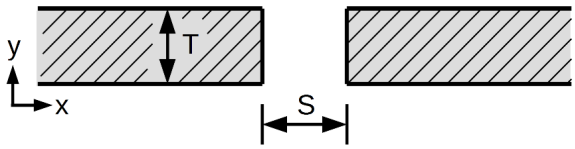

Figure 1.30: MSWG cross-section [2].

The MSWG was first experimentally investigated in the THz region in [44] with the following dimensions: $S = 270\ \mu$m and $T = 300\ \mu$m. Figure 1.31 plots the experimental and simulated data presented in [44]. The temporal pulse profiles shown in Fig. 1.31a illustrate that the pulse is not heavily distorted when propagating and experiences a reasonable loss of 0.03 dB/mm (at 0.5 THz).

A downside to the MSWG relates to system integration. In [44] the MSWG was excited by placing a photoconductive switch array normal to the waveguide entrance. The detector probe was placed normal to the propagation direction. This results in two orthogonal optical excitation paths which is sufficient for experimentation, however it is limiting when attempting to construct an integrated system. Solutions to this problem are identified later in Sections 3.1.1 and 3.1.1.

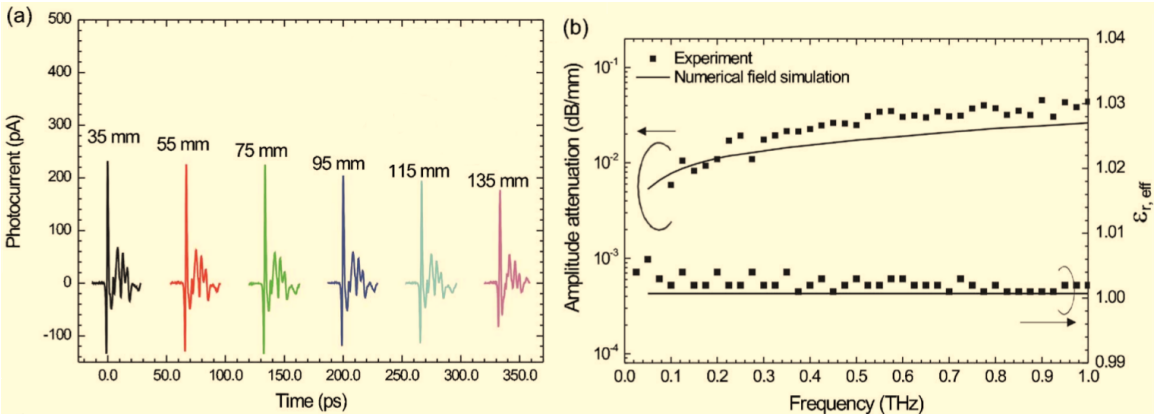

Figure 1.31: MSWG experimental data from [44]. a) Terahertz pulses sampled for different propagation distances along the MSWG. b) Frequency-dependent attenuation and effective permittivity derived from the time-domain data and from numerical field simulations. Reprinted by permission from [44]. © 2007 AIP Publishing.

1.7.6 Plastic Photonic Crystal Fiber

PPCFs are capable of transmitting a THz pulse with relatively low loss and dispersion (compared to a step-index single-mode fiber). In [34] a PPCF was constructed which consisted of a solid High Density Polyethylene (HDPE) core (diameter = 500 μm) surrounded by HDPE tubes (outer diameter = 500 μm, inner diameter = 400 μm). Figure 1.32 illustrates the cross section of the constructed PPCF. The PPCF guides the field via Total Internal Reflection (TIR) and therefore no conductors are required which eliminates the conductor loss. Field attenuation is primarily dependent on the dielectric material loss of HDPE which resides in the 0.2 dB/mm to 2 dB/mm range at 1 THz [34]. The loss for the PPCF in [34] was measured to be 0.4 dB/mm at 0.6 THz. Figure 1.33 plots the temporal and spectral responses for a THz pulse transmitted through a PPCF where it is clear that the pulse experiences some distortion. The PPCF is not well-suited for system integration because it requires excitation by a radiated source (i.e. photoconductive antenna) and is not a planar structure.

Figure 1.32: PPCF cross-section. Reprinted by permission from [34].

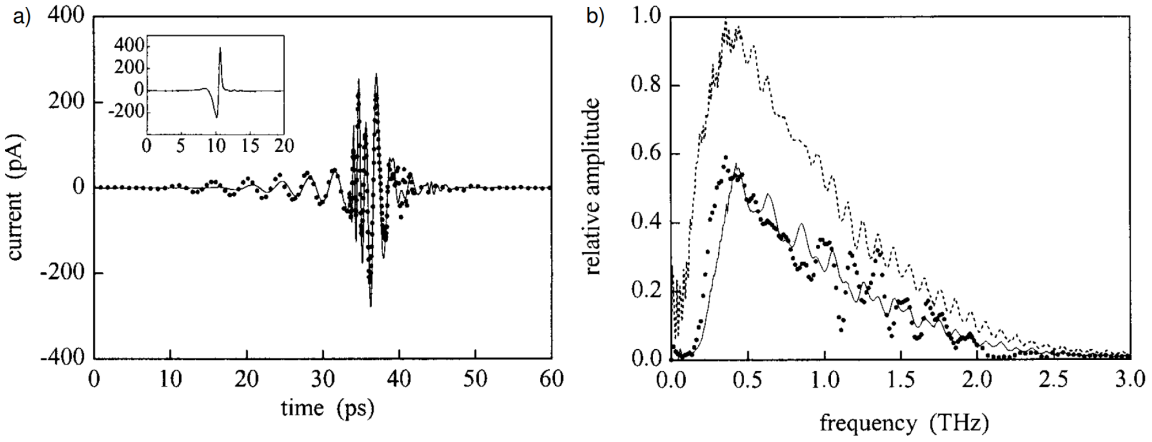

Figure 1.33: PPCF experimental data from [34]. a) Measured (dots) and calculated (solid line) pulses after propagating through a 2 cm long PPCF. The inset shows the measured input pulse. b) Amplitude spectra of measured (dots) and calculated (solid line) pulses after propagating through a 2 cm long PPCF. The dashed line shows the input pulse spectrum. Reprinted by permission from [34]. © 2002 AIP Publishing.

1.7.7 Ribbon Waveguide

The ribbon waveguide consists of a thin dielectric layer suspended in air and claims the lowest loss in the THz region (0.0002 dB/mm) [35]. Little discussion will be given for this waveguide because it is heavily impacted by GVD limiting its applicability when transmitting THz pulses (however it is useful for narrow-band systems). This limitation was discussed in detail in [45].

1.7.8 Summary of Waveguide Technologies

A number of previous studies use a similar experiment to THz-TDS (Fig. 1.12) for characterization, except the "Sample" is the waveguide of interest. More specifically all waveguides, except the CPS waveguide, were excited by radiation. The radiation configuration is acceptable for characterization; however, it is impractical to implement into an integrated system due to coupling issues. Table 1.2 compares an achievable attenuation coefficient for each of the discussed waveguide technologies. The approximate spatial field area is given as a geometrical comparison between the various waveguides.

Waveguide Type	$\approx \alpha$ (dB/mm) @ 0.5THz	$\approx A_{field}$ (mm^2)
PPWG [46]	0.01	$0.104 \times 10 = 1.04$
Sommerfeld Wire [31]	0.005	$\pi\ 6^2 = 113$
TWWG [32]	0.005	$0.3 \times 5 = 1.5$
CPS on a thin membrane [47]	0.4	$0.06 \times 0.03 = 0.0018$
MSWG [33].	0.03	$0.3 \times 0.3 = 0.09$
PPCF [34]	0.4	$\pi\ 0.25^2 = 0.2$
Ribbon Waveguide [35]	0.0002	N.A.

Table 1.2: Approximate attenuation coefficient and field area for various waveguides.

We limited our focus to waveguides which could be excited using a photoconductive region which acts similarly to a small current line ($\approx$ 20 μm). This means the waveguide is not excited with a plane wave or a mode-matched field which limits the options significantly. The A_{field} column of Table 1.2 helps clarify this concept. If the field area is relatively large then relatively large structures (i.e. conductors) are likely present. The fundamental mode profile of large structures are unlikely to match to a small current source and will resonate (higher order modes). To overcome this issue it is desirable to select small structures to avoid resonances and provide better coupling, the trade-off is higher attenuation.

A PPWG is not feasible because of the large geometry. A Sommerfeld wire is undesirable because of the bend loss and the radial mode is poorly matched to a small current line. The TWWG is also not feasible due to its large transverse geometry. The CPS is nicely matched [48] to a small current line, thus it is of interest. The MSWG can potentially be excited by a small current source, thus it is of interest. The PPCF can only be excited by a radiated field and is not of interest. Again the ribbon waveguide is not of interest due to substantial GVD (and requires excitation by a radiated field).

This research was constrained to using waveguides which could be integrated with other components (i.e. filters, resonators, antennas, etc). The MSWG and CPS waveguide were the most appealing because they could satisfy this criteria. While both of these structures do not have the lowest attenuation, past literature [33, 47] illustrated sufficient performance to justify further investigation. The CPS waveguide on a thin membrane is the most appealing because photolithography can be used to fabricate complex circuits.

Chapter 2

Fabrication

This chapter discusses the fabrication process for the device presented in Appendix C. Fabrication for the photoconductive devices in Appendix A-B is not explicitly discussed here because they are simple in comparison; however, their processing steps can be inferred by negating irrelevant steps (i.e. removing the epilayer).

2.1 General Fabrication

This section details the individual fabrication steps required to fabricate the structure in Appendix C. Section 2.2 uses the information from this section to describe the procedure for fabricating thin-film LTG-GaAs devices.

The following list identifies the required fabrication processes:

1. Crystal Growth and Annealing,
2. Photolithography,
3. Surface Metalization and Etching,
4. Epitaxial Layer Lift-off,
5. Photolithography on a Thin Silicon Nitride Membrane.

2.1.1 Crystal Growth and Annealing

A main component in a photoconductive THz system is the LTG-GaAs epilayer which is required because of its subpicosecond carrier lifetime. For most THz applications

the LTG-GaAs epilayer is grown at a low-temperature ($\approx 230°C$) via Molecular Beam Epitaxy (MBE) on a SI-GaAs substrate. Low-temperature growth of GaAs results in defects (Arsenic antisites) in the crystalline structure which form midgap states that quickly trap electrons from the conduction band [49].

As-grown LTG-GaAs (unannealed) has a minimal carrier lifetime (≈ 0.09 ps) and substrate resistance of 3 MΩ (for a 5 μm gap) [49]. It is desirable to increase the substrate resistance to reduce the dark current. This is accomplished by thermal annealing; however, as a consequence the carrier lifetime also increases. In the limit of reasonable annealing (i.e. 600°C for 10 mins) the defect concentration reduces substantially and the carrier lifetime becomes much greater than 1 ps. For the work in Appendix C the substrate was annealed at 450°C for 10 minutes which corresponds to carrier lifetime of ≈ 0.23 ps and a substrate resistance ≈ 15 MΩ (for a 5 μm gap) [49].

Later during fabrication, we plan to remove the LTG-GaAs epilayer from the base SI-GaAs substrate. This process requires another compound between the layers that can be etched selectively, meaning that the other compound dissolves leaving the LTG-GaAs and SI-GaAs intact. LTG-GaAs is grown on SI-GaAs because they have similar lattice constants, as required by MBE. AlAs has a lattice constant of 5.6605Åwhich is similar to GaAs (5.6533Å) and can therefore be grown epitaxially on GaAs. Fortunately AlAs is etched by Hydrofluoric (HF) acid while both LTG-GaAs and SI-GaAs are resistant to it, thus the LTG-GaAs epilayer can be released by submerging the crystal in HF acid [50]. Figure 2.1 illustrates the cross-section of the crystalline structure used in Appendix C. Note that the selected AlAs and LTG-GaAs layer thickness should be modified in the future, 50 nm AlAs and >1 μm LTG-GaAs [50].

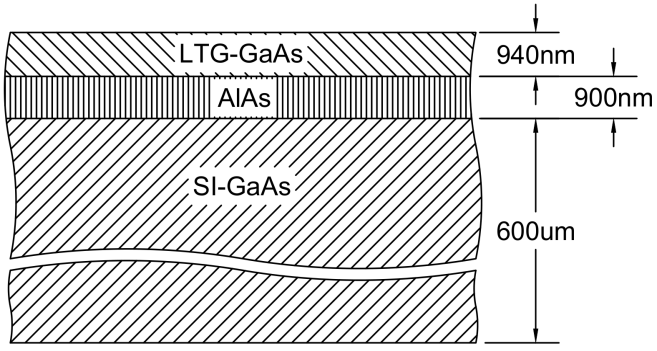

Figure 2.1: Crystal structure which is obtained by growth via MBE.

2.1.2 Photolithography

Photolithography is a process used to selectively mask areas on a substrate surface. The first step is to ensure the substrate is clean. For GaAs this requires that the substrate surface is free of organic compounds, metal ions, and the thin (1-2 nm) native oxide layer [51]. To remove organic contaminates and metal ions the following procedure was used: sonicate the substrate in acetone for 10 mins, sonicate the substrate in methanol for 5 mins, then rinse the substrate in Deionized (DI) water (> 15 MΩ·cm). Next the oxide layer is removed by placing the substrate in a 1:1 HCl/H_2O solution for 10 s. If the substrate is heavily contaminated other recipes are available (see [51]).

After the substrate surface is clean and dry, the following procedure is performed for a each sample (see Fig. 2.2):

1. The substrate is coated in Lift-off Resist (LOR) via a spin coater (2500 rpm, 30 s, 10000 rpm/s) (Fig. 2.2b).

2. The substrate is placed on a hotplate (170°) for 3 minutes to evaporate the solvent in the LOR.

3. The substrate is removed from the hotplate and left to cool to room temperature.

4. The substrate is coated in Shipley S1813 (the positive photoresist) via a spin coater (5000 rpm, 30 s, 10000 rpm/s) (Fig. 2.2c).

5. The substrate is placed on a hotplate (110°) for 1 minute to evaporate the solvent in the Shipley S1813.

6. The substrate is removed from the hotplate and left to cool to room temperature.

7. NOTE: The surface is now delicate, if the thin LOR/S1813 film gets scratched you must start over (be careful with tweezers). Remover PG is required to clean the LOR layer (discussed later).

After the sample has been coated in Shipley S1813 the process for mask alignment begins. The mask aligner uses a high power collimated UV light source with a programmable exposure timer. A mask (typically chrome on quartz) is placed between

the UV light and the substrate surface to selectively place a shadow over desired areas (i.e. mask). The mask and substrate are brought into contact to minimize the effect of diffraction (Fig. 2.2d). Then the substrate is exposed to the UV light for a specified amount of time, Δt. The mask aligner's UV intensity should be constant. During our research it was measured to be $I_0 = 22$ mW/cm^2. To calculate an appropriate exposure dosage ($E_0 = I_0 \times \Delta t$) knowledge of the dissolution rate of the LOR in the developer solution (MF-319) is required. From [52] the dissolution rate of LOR in MF-319 is approximately 14 nm/s. From experimentation we found that an undercut of roughly 840 nm (60 s) was sufficient for good device yield. This implies that the sample needs to remain in the developer for at least 60 s after the S1813 is removed via development. It is desirable to have a relatively slow S1813 development rate such that the 60 s required to remove and undercut the LOR does not cause any undesirable effects to the S1813. From experimentation it was found that an $\Delta t \approx 3$ s ($E_0 = 3 \times 22$ mW/cm^2 $= 66$ mJ/cm^2) gave the best results. After UV exposure, development in MF-319 for 3 min 45 s (Fig. 2.2e) was required. As a final step the sample is rinsed in DI water (> 20 s). The previously specified values can vary depending on environmental conditions and chemical ages. Figure 2.3 is a top-down image of a small section of a CPS transmission line after development where the undercut is clearly visible.

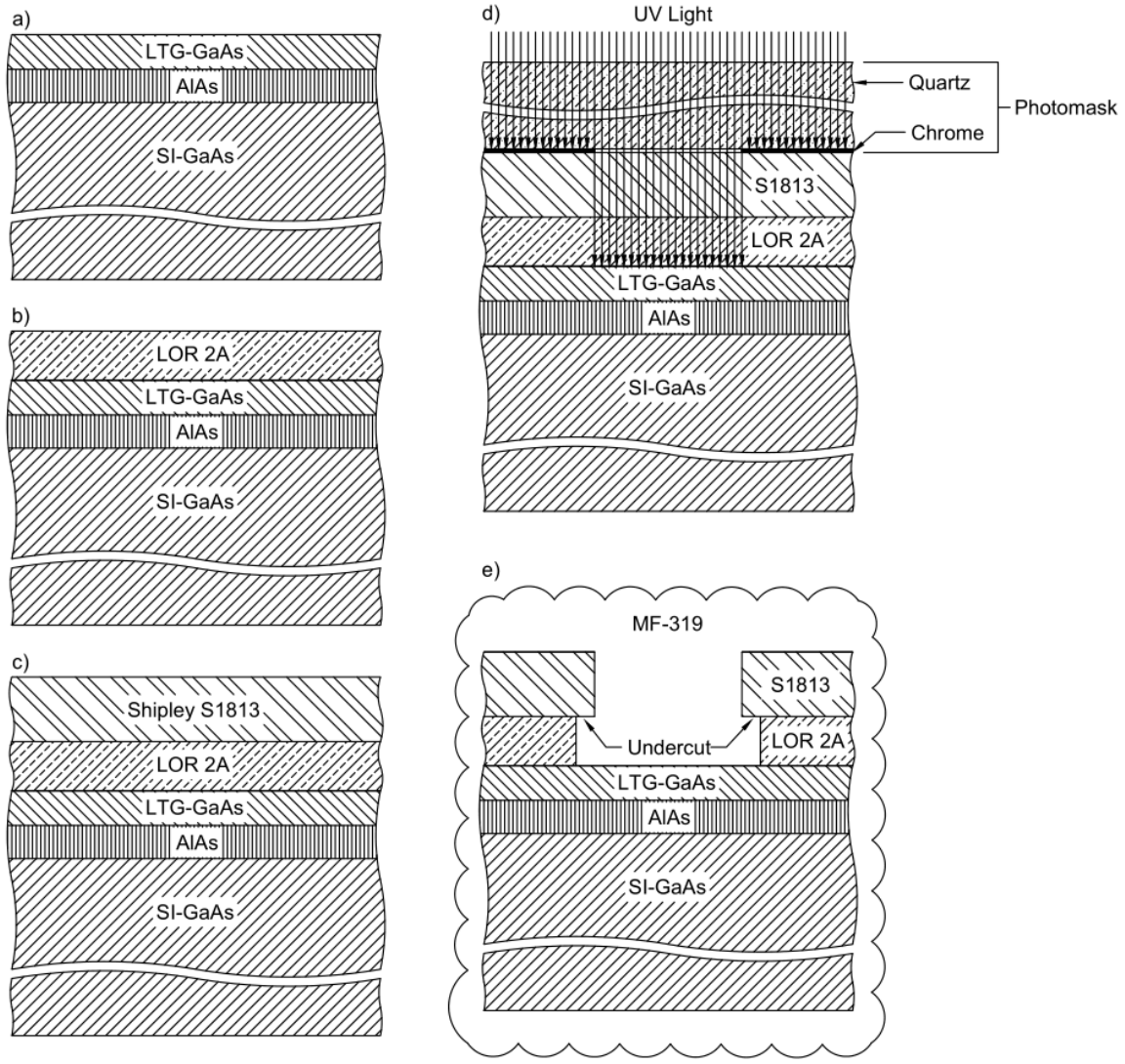

Figure 2.2: Photolithography process. a) Clean sample. b) Addition of LOR 2A via spin coating. c) Addition of Shipley S1813 via spin coating. d) Stucture masking and exposure to UV light. e) Development in MF-319 to remove S1813 and LOR2A in areas which were exposed to UV light.

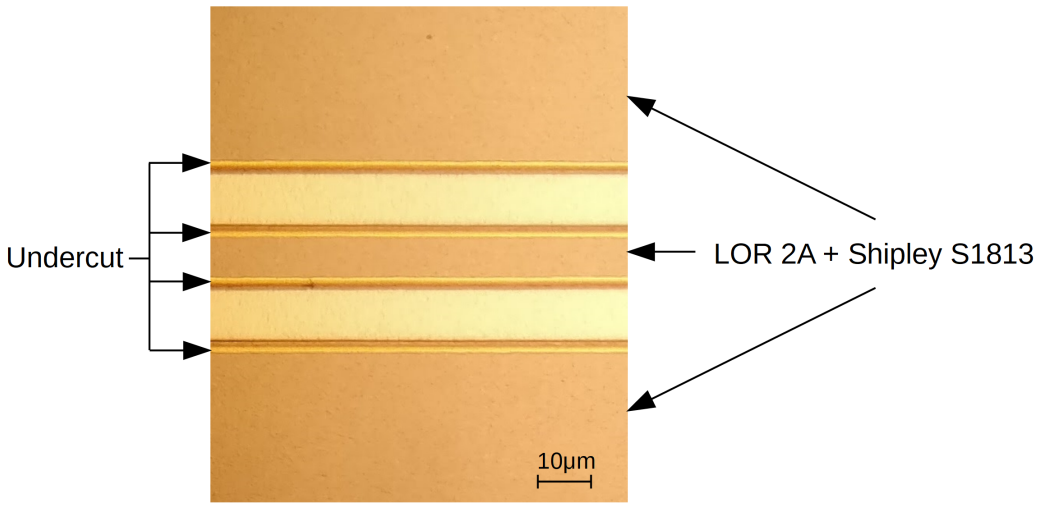

Figure 2.3: Top-down image illustrating the undercut during the fabrication of a CPS transmission line.

2.1.3 Metalization and Etching

After photolithography is completed certain areas of the substrate surface will be masked by the S1813 and LOR. Depending on the fabrication goal there are two common directions to pursue, either metallic conductors will be deposited or trenches will be etched in the substrate. Figure 2.4 illustrates both methods.

Figure 2.4(a-b-c) illustrates the gold deposition and lift-off procedure. The metallic contacts are deposited by Physical Vapor Deposition (PVD), both electron-beam evaporation and Radio Frequency (RF) sputtering were used during the research (depending on equipment availability). Titanium (Ti) (5 nm) is used as an adhesion layer and Gold (Au) (100 nm) is used for its superior conductive and environmental resistance properties. Figure 2.4b demonstrates the purpose of the LOR. If the LOR was absent then the Ti/Au thin film could form a continuous connection between the S1813 and the substrate surface. This bond makes it difficult to cleanly remove the S1813 without damaging the metalization on the substrate surface.

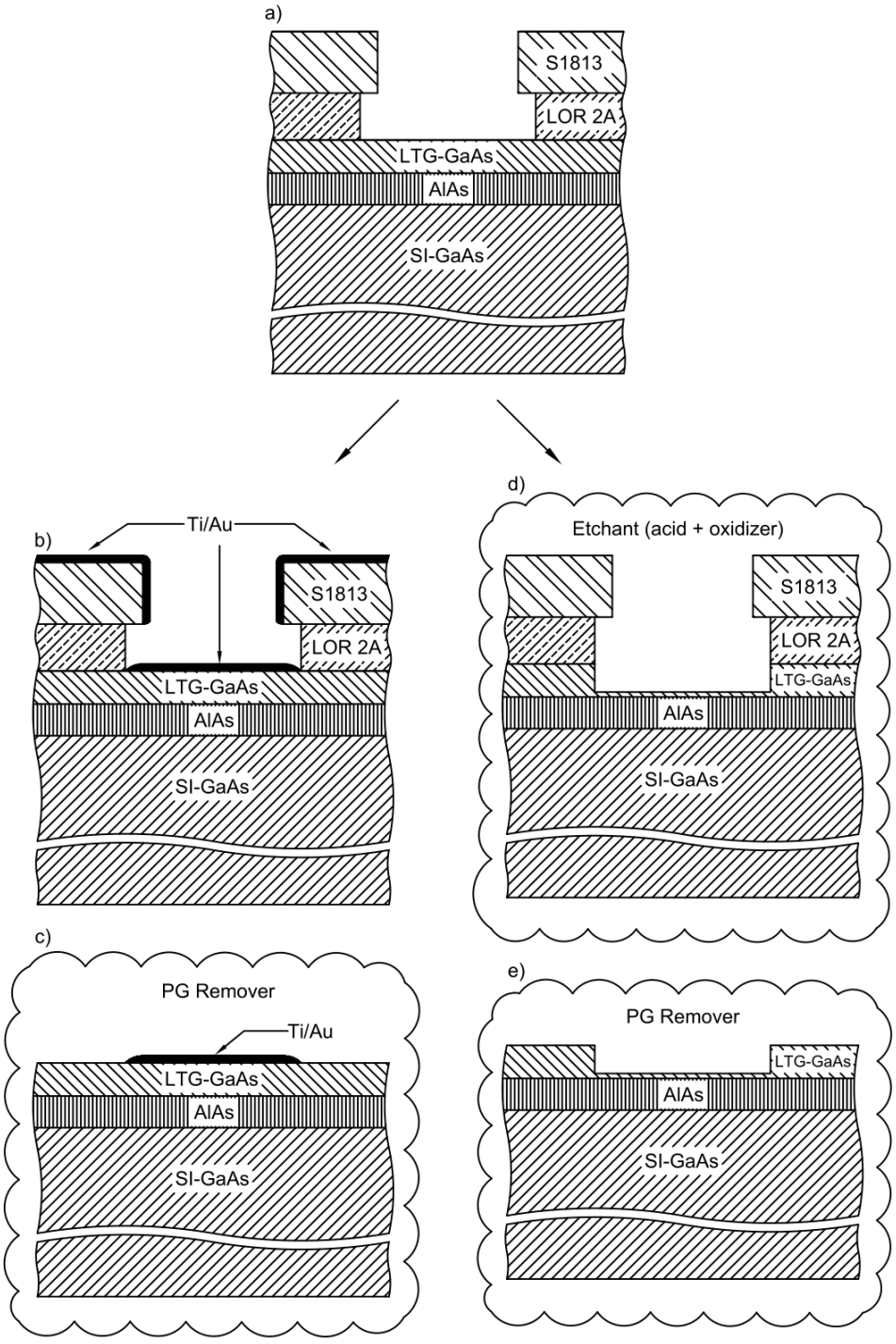

Figure 2.4: Metal deposition and substrate etching. a) Substrate with lithograhically masked areas. b) Metal deposition over entire sample. c) Lift-off of masking materials in Remover PG. d) GaAs substrate etched in unmasked areas. e) Removal of masking materials in Remover PG.

Figure 2.4(a-d-e) illustrates the substrate etching process. For substrate etching the LOR provides no benefit and could have been skipped in previous steps. Figure 2.4d depicts GaAs etching. GaAs is etched by most acid/oxidizer combinations. In this thesis a combination of citric acid and hydrogen peroxide (30%) was used (5:1). After gold deposition or etching the substrate is placed in Remover PG (a proprietary N-Methyl-2-Pyrrolidone (NMP) based solvent) at 60°C to soak (1 hr) which removes the S1813 and LOR. Note that Remover PG is extremely flammable (flash point 88°C) and must be used below this temperature. After the soaking is completed, the substrate is thoroughly rinsed with DI water and the processing is complete.

2.1.4 Epitaxial Layer Lift-Off

This process requires the use of HF acid (hazardous!). Proper training is required.

As noted in Section 2.1.1 the LTG-GaAs epilayer was grown on a sacrificial AlAs layer. When the sample is submerged in HF acid the AlAs layer dissolves while the LTG-GaAs and SI-GaAs layers remain unharmed. Figure 2.5 illustrates the process. To ensure the LTG-GaAs epilayer does disappear in the HF acid (after etching) an etch resistant wax (Apiezon Wax W) is melted (hotplate 130°C) onto the LTG-GaAs surface. Next a polystyrene rod is carefully placed in contact with the wax to bond the two structures (see Fig. 2.5b). Next the polystyrene rod (attached to the sample) is placed in a closed plastic container 1/4 to 1/2 filled with 10% HF acid overnight (sample submerged, not entire rod). Once the LTG-GaAs layer is separated, the polystyrene rod (and epilayer) are removed from the plastic container and rinsed in a water mixed with calcium carbonate to neutralize any residual HF acid. Then the sample is rinsed in DI water. The polystyrene rod is carefully removed from the wax mechanically using a scalpel. At this point the LTG-GaAs layer can be placed on another substrate (SiO_2, Si_3N_4, Mylar, Teflon, etc.) provided that it is not impacted by the chemical used to dissolve the Apiezon Wax W. For example, the substrate should be resistant to Trichloroethene (TCE) .

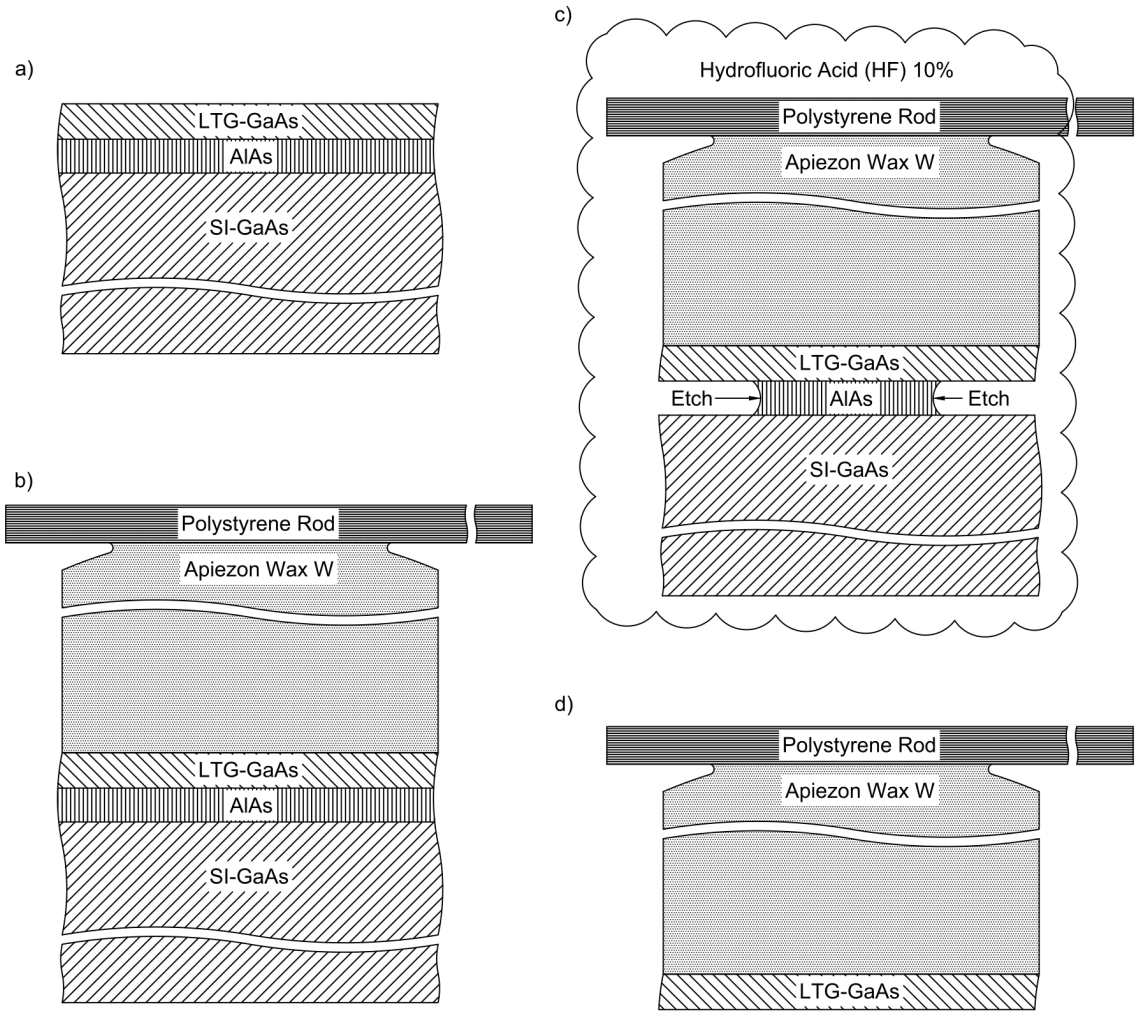

Figure 2.5: Epitaxial layer lift-off process. a) Starting clean substrate. b) Apiezon Wax W is melted onto the LTG-GaAs surface and a polystyrene rod is gently placed in contact with the melted wax to bond the materials. c) The polystyrene rod is placed in HF acid to dissolve the AlAs layer. d) The polystyrene rod is removed from the HF acid and cleaned in water mixed with calcium carbonate (to neutralize the HF acid) then rinsed with DI water.

2.1.5 Photolithography on a Thin Silicon Nitride Membrane

This section describes the methods used to overcome unique issues associated with UV lithography on a thin silicon nitride membrane window. The main issue is that the membrane is very delicate and great care is always required, plastic tweezers are necessary when handling the sample. Initial cleaning of the membrane is likely

to cause more harm than good, therefore cleaning is avoided unless necessary (i.e. a mistake was made during fabrication); however, cleaning will be discussed later. The second issue is that the silicon nitride membrane is suspended in free-space on a silicon frame which makes it difficult to use the vacuum chuck on the spin coater. This issue was overcome by using 2-sided thermal release tape to bond the silicon frame to a standard silicon wafer for mechanical support. The mechanical support wafer (and attached silicon frame and silicon nitride membrane) could then be placed on the vacuum chuck, and the spin coater could be used normally (place a number of LOR drops on the membrane surface, then turn on). Next, the silicon frame is removed from the mechanical support wafer by placing it on a 110°C hotplate for approximately 10 s. After heating, the thermal release tape is no longer adhesive and the sample can be removed. The sample was then placed on another hotplate to evaporate the LOR solvent (170°C for 3 mins). The sample was removed from the hotplate to cool to room temperature, then it was re-bonded to the mechanical support wafer with the 2-sided thermal release tape. Shipley S1813 was deposited on the membrane surface via spin-coating. Again the sample was removed from the mechanical support wafer by placing it on a 110°C hotplate for approximately 10 s. The sample was then replaced onto the hotplate to evaporate the S1813s solvent (110°C for 1 min). The sample is then removed from the hotplate where it cools to room temperature, after which it is now ready for mask alignment. Mask alignment, UV exposure, and development are identical to the previous discussion (i.e. not on membrane). However, after development, the undercut (Fig. 2.3) must be visible under the microscope (40× objective). If no undercut is visible, the procedure must start over, except now the substrate must be cleaned first.

To clean the silicon nitride membrane (remove the LOR and S1813) it must be placed (no squirt bottles because the pressure could damage the substrate) in a heated bath of Remover PG (60°C) for at least 30 min. Afterwards it should be placed in a bath of isopropyl alcohol for 1 minute, then placed in a bath of DI water for 1 minute. Drying with a N_2 blower must be done very careful, low pressure and blown tangential to the surface (not normal to the surface becuase the membrane will get damaged). It is unlikely that all the water will dissipate due to crevices in the silicon frame, a cleanroom cloth can be used to soak up some of the droplets in the frame. The frame should then be placed on the 110°C hotplate for 10 mins to dehydrate the surface. After cooling to room temperature processing can begin again, however adjusting exposure and development times to attempt to achieve a visible undercut.

2.2 Fabrication of Small LTG-GaAs Active Regions

The goal is to use a single host substrate (4 mm × 4 mm) to create an array of many small thin-film LTG-GaAs active regions (40 μm × 20 μm). Figure 2.6 is a rendering of the desired devices. This goal was achieved by following a fabrication process similar to the one described in [53].

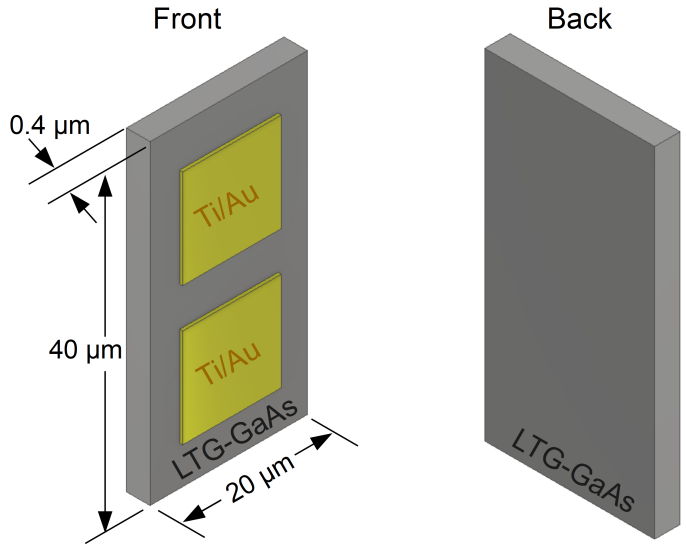

Figure 2.6: Single small thin-film LTG-GaAs region.

Starting from an annealed substrate (Fig. 2.1) cleaning, photolithography, deposition, and lift-off are performed to define the contacts across the entire 4 mm × 4 mm sample. Next the process is repeated (except skipping the LOR) on the same sample which now has gold contacts. This time actual mask alignment is required meaning that markers on the mask are aligned with lithography-defined features on the substrate (gold "+" symbols). After mask alignment, UV exposure, and development each of the future active regions will be coated in S1813 for protection against the LTG-GaAs etchant (5:1, citric acid and 30% hydrogen peroxide). The entire substrate is submerged in the GaAs etchant for ≈ 1 min then removed to measure the etching rate using a profilometer (≈ 130 nm/min). Once the actual etch rate is known the substrate is placed back into the etchant until only 200 - 300 nm of the LTG-GaAs substrate remain (this requires knowledge of the epilayer thickness). Next the LTG-GaAs layer is removed from the substrate by following the procedure in Section 2.1.4. Afterwards the substrate is then placed back into the GaAs etchant to remove the

200 - 300 nm of substrate which was previously left behind. At this point the back of many small thin-film GaAs devices should be visible (see Fig. 2.7a). Finally the LTG-GaAs devices need to be removed from the wax and placed onto another substrate for storage. This is accomplished by placing the samples (attached to the wax) onto a Mylar membrane which is tilted at a slight angle ($\approx$ 5-10°) then slowly placing TCE droplets onto the wax. TCE quickly liquefies the black Apiezon Wax W and is messy therefore cleanroom clothes need to be readily available to absorb the run-off. Once all the wax has been dissolved, a large percentage of the small thin-film LTG-GaAs should remain on the Mylar membrane. The front of the devices should now be visible on the Mylar membrane (Fig. 2.7b). Note that the dark spots in Fig. 2.7b are residual wax which existed when the picture was taken. The last step is to remove any remaining S1813 which was providing protection against the GaAs etchant and the wax. This is accomplished by carefully placing some drops of methanol onto the surface of the samples (on the Mylar membrane), then carefully placing some drops of Isopropyl Alcohol (IPA) to remove the remaining methanol, then a few drops of DI water are placed to bond the devices via Van der Waals (VDW) forces [50]. Figure 2.7b is an image of the front side of the LTG-GaAs devices on the membrane.

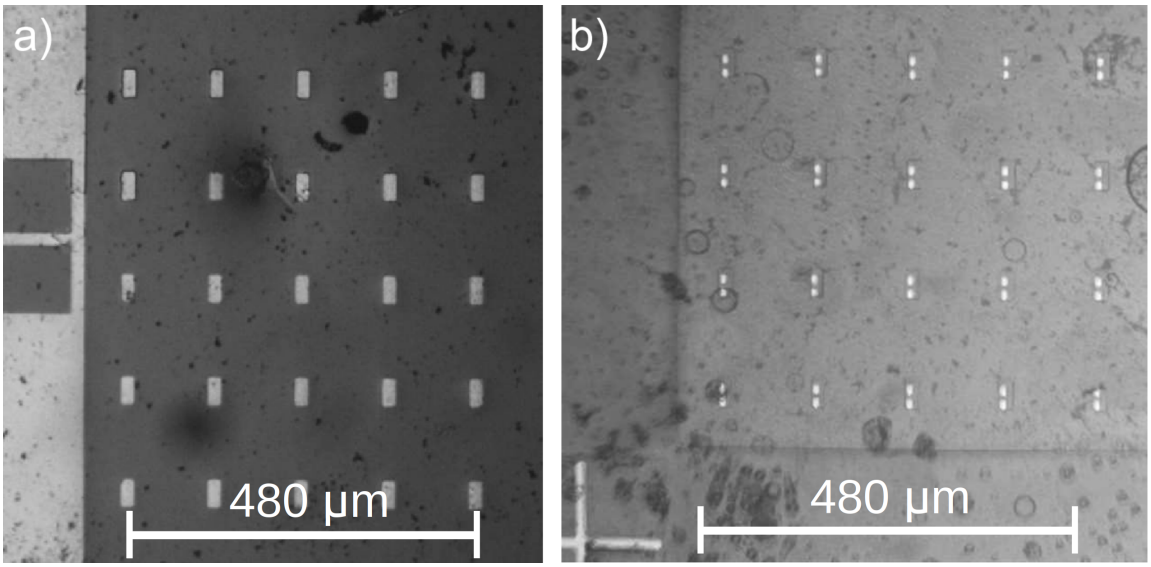

Figure 2.7: Array of small thin-film LTG-GaAs regions. a) Back-side attached to wax. b) Front-side visible on the Mylar membrane.

Placement of thin-film LTG-GaAs regions onto an arbitrary substrate

After the LTG-GaAs regions are bonded to the Mylar membrane they can be transfered to an arbitrary substrate by placing the Mylar membrane with the devices facing the arbitrary substrate. The devices can then be "popped" off the Mylar membrane by applying pressure from the back of the membrane using a sharp needle. For this research we used an acupuncture needle connected to an x-y-z stage on a probe station to perform this process. After the thin-film LTG-GaAs device is transfered to the arbitrary substrate it is pushed to the desired location again using a x-y-z stage with acupuncture needle on a probe station. Once the device is in the correct location a drop of DI water is placed onto the surface and left to dry where it becomes bonded via VDW forces [50]. We found this process works reasonably well; however, if a better bond is required the Focus Ion Beam (FIB) can be used as noted in Appendix C.

Chapter 3

Contributions

A key focus of the research was to design, fabricate, and test THz waveguides with low loss and minimal dispersion. Equally important (and more challenging) was to design the THz system (source, waveguide, receiver) which could be implemented into a manufacturable Terahertz system-on-chip (TSoC) platform. A promising THz waveguide structure was proposed in my M.A.Sc thesis [9] but the design suffered from a difficult and expensive (thousands of dollars per device) manufacturing procedure. This thesis focused on simplifying the manufacturing procedure while demonstrating suitable experimental results for proof-of-concept designs. Numerous experiments were proposed and executed, but a number of these experiments did not have satisfactory results. Regardless, all of the experiments provided useful insight and helped identify the next logical step. This section states my main contributions to our research group and Section 3.1 lists the contributions to scientific literature.

Developed and demonstrated a TSoC platform. We successfully constructed and tested a proof-of-concept TSoC platform using a CPS waveguide on a thin silicon nitride membrane. This research concluded that fabrication was possible and THz pulses can be generated, transmitted, and detected over reasonably long distances. Going forward there is no question if fabrication is possible or if experimentation generates useful results with minimal distortion. Future work can use this platform to investigate a wide variety of circuit elements. For example, a simple filter can be fabricated by periodically varying the characteristic impedance of the waveguide (similar to Bragg grating).

Developed recipe to lift-off LTG-GaAs epilayer. Using equipment available to our research group we successfully replicated the fabrication of small thin-film

LTG-GaAs layers from [53]. Using these thin-film LTG-GaAs epilayers we generated and detected THz pulses on a thin Si_3N_4 membrane and on a glass slide. The small thin-film LTG-GaAs devices can be bonded to different substrates, thus future research could use them for system characterization.

Fabricated and tested MSWG structures. Originally we investigated MSWG structures because of their low loss and low-dispersion properties (and planar geometry). We experimentally demonstrated two useful structures. A Linear Tapered Slot Antenna (LTSA) which can be used as an alternative to a HRFZ-Si for THz beam forming. During this work we noticed an effect which was not clearly identified in the original publications [44, 54]. We found the MSWG would resonate and distort the pulse. A simple fix was identified, using a thinner MSWG (≈ 50 μm); however, the trade-off is higher loss and reduced mechanical strength. For us the larger concern was the reduced mechanical strength because copper becomes delicate when thinner than 150 μm. However we wanted to overcome the resonance issue for our next device in a step towards a MSWG-based THz platform. This platform consisted of a photoconductive THz source, MSWG, and photoconductive receiver. The MSWG was tapered to a lower loss configuration for the majority of the propagation distance to reduce the overall loss. To overcome the mechanical strength issue we selected to fabricate the waveguide from 51 μm (0.002") gold-plated stainless steel which functioned well. Any future work which utilizes a MSWG should consider this resonance effect.

Developed and maintained an experimental facility. All of the research presented in this thesis required experimentation. Most of the experiments were configured similarly to the THz-TDS experiment (i.e. Fig. 1.12) which requires automated instrument control to obtain accurate and reproducible results. For the THz-TDS experiments software was written (in C Sharp) which controlled the delay line via its controller (Thorlabs BSC201), collected the data from the lock-in amplifier (Stanford SR830), and plotted the temporal and spectral response. This software is available for future students to use and modify.

A number of other experimental configurations were assembled using a 1550 nm excitation wavelength and used extensively. Unfortunately we did not obtain useful results from all these experiments, thus experimentation stopped; however, useful knowledge was gained relating to experimental design. These ex-

periments are noted briefly here:

- A fiber-based pulsed THz system for photoconductive switching at 1550 nm was designed similar to [55]. The system was fully operational and included dispersion management, functionality was confirmed by optical autocorrelation measurments. The instrument control scripts (in Python with PyVISA) controlled the delay line (General Photonics MDL-002), voltage (Agilent E3631A), data collection (Standford SR830), and plotting (matplotlib). This experiment was stopped because of unsatisfactory THz pulse generation, transmission, detection results. We knew that a wavelength of 1550 nm is weakly absorbed by GaAs and decided to eliminate this variable and revert to 780 nm. Upon reverting to 780 nm we obtained the data that was published in [1, 2].
- A fiber-based CW THz system for photoconductive mixing was assembled in parallel with the pulsed system. This system was similar to the pulsed system, but two CW tunable (1465 nm to 1575 nm) lasers were combined and used instead. An Erbium-doped fiber amplifier (EDFA) was used to increase the optical pump power delivered to the photoconductors. The instrument control scripts (in Python with PyVISA) controlled the lasers (Agilent 81989A), EDFA (Lightwave 2020 VGA), voltage (Agilent E3631A), data collection (Standford SR830), and plotting (matplotlib). This system was abandoned for a similar reason, 1550 nm is weakly absorbed by GaAs. Given the pulsed difficulties we decided that CW results were unlikely, thus we proceeded to try quasi-CW system.
- A fiber-based quasi-CW THz system for photoconductive mixing. A quasi-CW system is similar to a CW system except the mixed CW optical signal is intensity modulated with a small duty cycle to reduce the average optical power. After modulation the signal is amplified to increase the peak power. This experiment utilized an electro-optic intensity modulator to reduce the duty cycle to D = 0.8 ns / 1.0 μs $\times$ 100% = 0.08%. Unfortunately this experiment was halted prematurely primarily due to an equipment failure. The software in our Tektronix Communications Signal Analyzer (CSA) 8000A failed to load and was too expensive to fix. Figure 3.1 illustrates the measured intensity for the modulated optical pulse with two separate beat frequencies. For Fig. 3.1 the beat frequency could be resolved by

the CSA, whereas when the beat frequency was 1 THz the beat frequency could not be resolved, thus the average value is seen.

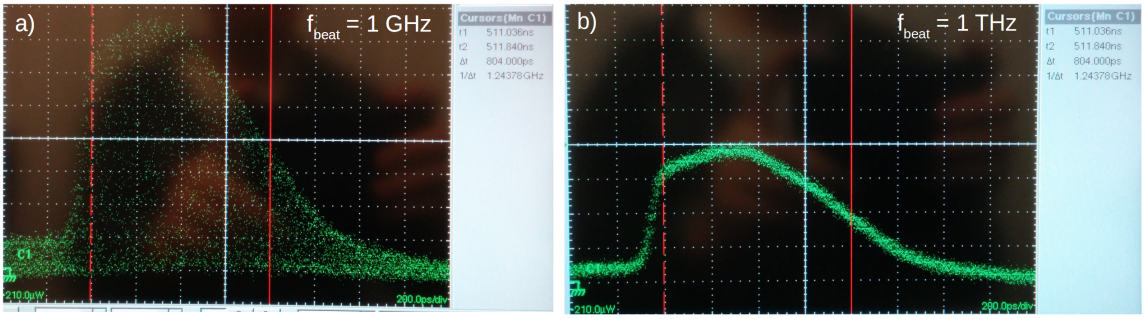

Figure 3.1: Quasi-CW experiment. a) Beat frequency, f_{beat} = 1 GHz. b) Beat frequency, f_{beat} = 1 THz.

3.1 Contributions to Scientific Literature

3.1.1 Main Contributions

The following main contributions are presented in chronological order and state the initial reasoning for pursuing the research. Copies of the published papers are located in the Appendices. It is intended that the respective Appendix is read after reading each of the following sections.

THz-TDS Using a Photoconductive Free-Space Linear Tapered Slot Antenna Transmitter [1]

In [1] we investigated coupling the THz field generated by photoconductive switch to a MSWG configured as a LTSA. This experiment was the initial step for testing near-field coupling to a thin MSWG for use in a THz system. The designed THz LTSA proved to be a useful antenna which could be used as an alternative to existing HRFZ-Si refractive elements.

See Appendix A for copy of published paper.

Contributions:

Levi Smith - Concept, Fabrication, Experiment, Simulation, Writing

Thomas Darcie - Concept, Writing

Afshin Jooshesh - Experimental assistance

James Zhang - Conceptual assistance

Photoconductive Generation and Detection of THz-Bandwidth Pulses Using Near-Field Coupling to a Free-Space Metallic Slit Waveguide [2]

Success of the work presented in [1] made it clear that we should investigate the same antenna, except, used as both the transmitter and receiver to remove all refractive THz elements. Instead, we decided that first we should directly connect the transmitter and receiver using the MSWG in a low-loss configuration (i.e. larger conductor separation). Using knowledge gained from [1] we selected a thinner MSWG to reduce pulse distortion. This concept is the basis of the work [2].

See Appendix B for copy of published paper.

Contributions:

Levi Smith - Concept, Fabrication, Experiment, Simulation, Writing

Thomas Darcie - Concept, Writing

Afshin Jooshesh - Experimental assistance

James Zhang - Conceptual assistance

Demonstration of a low-distortion terahertz system-on-chip using a CPS waveguide on a thin membrane substrate

Shortly after [2] was published we discovered that we could purchase a large (10 mm $\times$ 10 mm) thin (1 μm) silicon nitride membrane window on a silicon frame (15 mm $\times$ 15 mm). Using this substrate we could expect to transmit THz-bandwidth pulses with minimal distortion [43]. With this new information we decided to defer projects related to MSWG structures until we investigated the feasibility of creating a waveguide on a silicon nitride membrane. Upon literature search it seemed viable to fabricate structures on the thin membranes, but it was not clear if lithographic processing should be completed before or after silicon substrate etching (large difference in mechanical strength). We decided to experiment and attempt to fabricate transmission lines on the 1 μm thick silicon nitride membrane using standard UV lithography, Ti/Au sputtering deposition, and lift-off. We found that fabrication was possible (see Fig. 3.2) and the membranes are surprisingly durable for their thickness; however, as expected, fabrication is an extremely delicate procedure (i.e. sonication is not possible without destroying the membrane). Detailed information regarding fabrication is given in Section 2.1.

The work presented in Appendix C can be summarized as follows: a CPS waveguide was fabricated on a thin silicon nitride membrane, novel photoconductive devices were placed on the transmission line, THz-bandwidth pulses were generated, transmitted (10 mm), and detected with excellent performance. In Appendix C we did not investigate any transmission line components (filters, resonators, etc) because we were primarily interested in the proof-of-concept. However we are extremely optimistic about the ability of this platform to support a wide variety of complex THz systems on an integrated device. Figure 3.3 illustrates the experiment used for the work in Appendix C, a similar arrangement to that used for the work in Appendix B.

See Appendix C for copy of accepted paper.

Contributions:

Levi Smith - Concept, Fabrication, Experiment, Simulation, Writing

Thomas Darcie - Concept, Writing

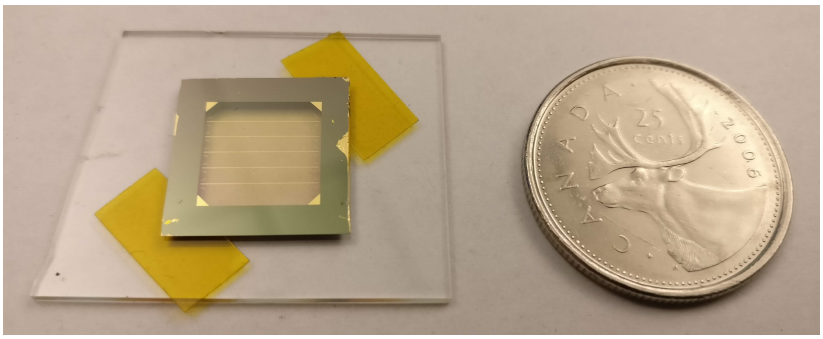

Figure 3.2: Image of CPS on membrane with lithographically-defined gold contacts.

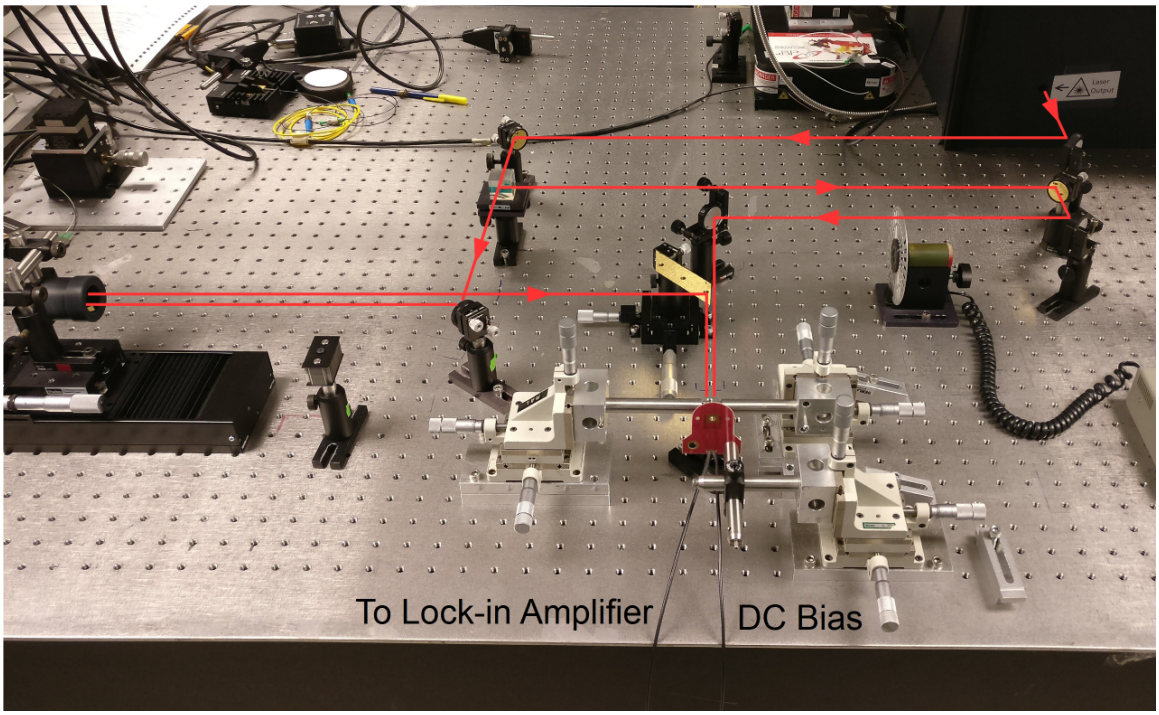

Figure 3.3: Image of CPS on membrane experiment.

3.1.2 Other Contribution

Non-waveguide related experiment and not copied into the Appendix.

Nanoplasmonics enhanced terahertz sources [56]

This work was completed in collaboration with Prof. R. Gordon's group at the University of Victoria. The majority of the work was completed by Dr. A. Jooshesh. The goal of this work was to increase the power radiated by a PCA by introducing a plasmonic array of gold hexagons. The array maximized the bias field (and current density) near the surface such that the gold hexagons could act as heat sinks. Fabrication of this device was completed using photolithography, Ti/Au deposition, and lift-off. Afterwards the plasmonic devices were "drawn" by sputtering away the gold (deposited over the active area) using a FIB. Figure 3.4 illustrates the result of this process. For this work I assisted with photolithography and optical/THz alignment.

Abstract:

Arrayed hexagonal metal nanostructures are used to maximize the local current density while providing effective thermal management at the nanoscale, thereby al-

lowing for increased emission from photoconductive terahertz (THz) sources. The THz emission field amplitude was increased by 60% above that of a commercial THz photoconductive antenna, even though the hexagonal nanostructured device had 75% of the bias voltage. The arrayed hexagonal outperforms our previously investigated strip array nanoplasmonic structure by providing stronger localization of the current density near the metal surface with an operating bandwidth of 2.6 THz. This approach is promising to achieve efficient THz sources.

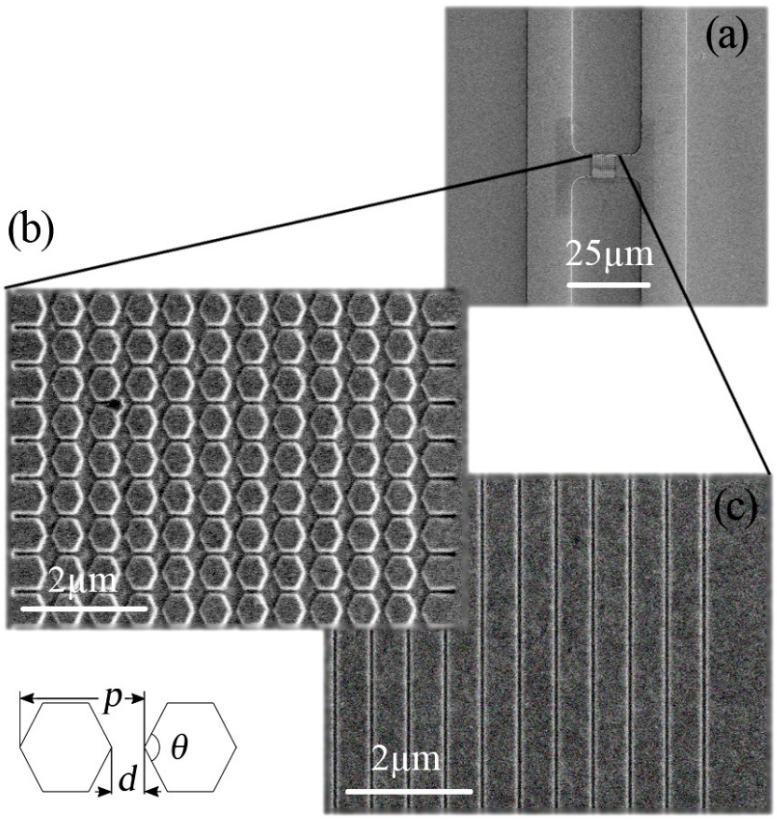

Figure 3.4: Hexagonal structures from [56]. a) Scanning electron microscope image of the 20 μm dipole on SI-GaAs substrate. b) The active area of the hexagonal plasmonic array. c) The active area of the strip plasmonic array. The diagram shows apex angle θ, gap size d and periodicity p. d = 100 nm, p = 587 nm, $\theta = 127°$. Reprinted by permission from [56]. © 2014 Optical Society of America.

Contributions:

Afshin Jooshesh - Concept, Fabrication, Experiment, Simulation, Writing

Levi Smith - Experimental and Fabrication assistance

Mostafa Masnadi-Shirazi - Fabrication
Vahid Bahrami-Yekta - Fabrication
Thomas Tiedje - Concept, Fabrication, Writing
Thomas E. Darcie - Concept, Writing
Reuven Gordon - Concept, Writing

Chapter 4

Conclusion and Future Work

This thesis investigated three planar waveguide devices experimentally. The first device (Appendix A) was a MSWG configured as an LTSA which was used for THz-TDS. This device can function as an alternative to standard refractive beam forming THz components (i.e. HRFZ-Si lenses). The second device (Appendix B) was an MSWG which was tapered (conductor separation increased) to reduce the overall loss and is an attractive option when transmission over relatively long distances ($\approx$ 20 cm) is necessary. The last device investigated was a CPS waveguide on a thin silicon nitride membrane (Appendix C). This device was found to function very well and shows great promise to serve as a THz platform which can host a multitude of circuits. To begin with filters, resonators, power dividers, couplers, tapers, antennas, antenna arrays, can all be investigated.

4.1 Future Work

4.1.1 Metallic-Slit Waveguide Devices

As mentioned earlier we had plans to test two MSWG-based antennas functioning as the transmitter and receiver. There are currently no experimental results for this configuration. Completion of this experiment should result in further justification that edge-coupled MSWG-based devices are useful in specific circumstances.

4.1.2 Waveguide Components on Silicon Nitride Membrane

In Appendix C a basic CPS on a thin silicon nitride membrane was investigated. In this work we wanted a baseline measurement, therefore no variation in waveguide geometry was introduced along the propagation direction. Future work will now recognize that the pulse will only undergo moderate distortion on a continuous waveguide. With this knowledge future devices such as filters, resonators, and couplers can be designed and tested then compared with the baseline measurement.

4.1.3 Fiber-Based Probe-Station Measurements

Early on we attempted to simplify the analysis of THz waveguides using a Fiber-Based Probe-Station (FBPS). The purpose the FBPS was to use standard telecommunication band (1550 nm) lasers and optical components (i.e. optical fibers) to excite and detect THz pulses. The setup was desirable because it allowed for experimentation with multiple configurations of THz circuitry. Usage of the FBPS for THz excitation and detection (via photoconductive switching and mixing) is a novel method which we have not seen demonstrated elsewhere in literature. The concept is illustrated in Fig. 4.1. The experiment was to be divided into a number of steps:

1. 1550 nm pulsed excitation without MSWG (Fig 4.2a),
2. 1550 nm continuous-wave excitation without MSWG (Fig 4.2a),
3. 1550 nm pulsed excitation with MSWG (Fig 4.2b),
4. 1550 nm continuous-wave excitation with MSWG (Fig 4.2b).

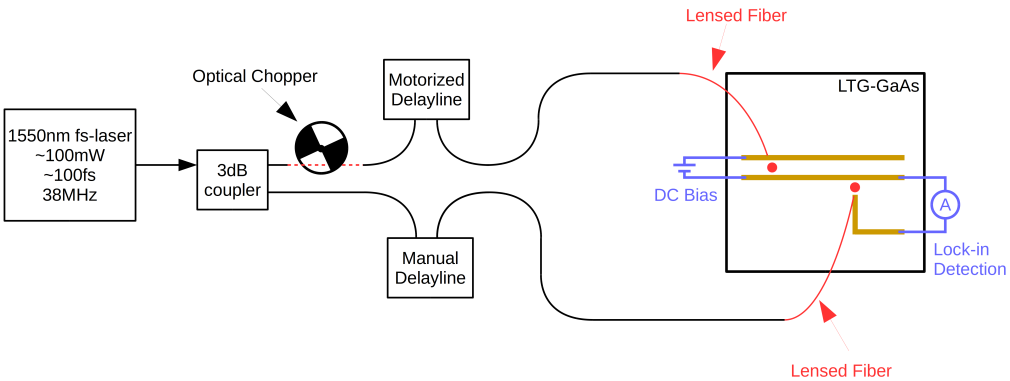

Figure 4.1: Optical fiber setup using the FBPS with lensed fibers.

Figure 4.3 is a picture which illustrates the electrical probes contacting the substrate to bias the active area and detect the generated current. The lensed fibers are also visible which deliver the optical pump to the active areas. Figure 4.4 gives an overall view of the FBPS.

Figure 4.2a depicts the first step of the series of experiments. This setup was selected to be the first since similar experiments were completed using free-space 780 nm [48] and 1550 nm [57] pulsed lasers without a FBPS. It was proposed that after we completed the first two steps (Fig 4.2a), we would cleave the substrate and move onto the next steps (Fig 4.2b). The first two steps of the experiment seemed like a simple task since they had been completed elsewhere [48]; however, after a number of months we were unable to collect any meaningful results from the FBPS. Prior to constructing this optical setup a number of non-ideal features were recognized:

1. A 1550nm laser ($E_{1550nm} \approx 0.8eV$) is only weakly absorbed by LT-GaAs ($E_G \approx 1.4eV$) because excitation occurs via defect states or two-photon absorption [58, 59, 55].

2. The optical pulse will broaden inside a fiber by dispersion (linear and simple to compensate) and self-phase modulation (non-linear and difficult to compensate); both of these effects will limit the THz-bandwidth, but not eliminate the signal.

3. The optical modulation (for lock-in detection) will be directly detected by the receiver and should appear as a fixed offset. Also given that past literature [57] used a similar arrangement we were not worried about this artifact.

Given that we were aware of the weak 1550 nm optical absorption we reverted to using a 780 nm optical excitation where absorption was guaranteed which led to quick results and the work presented in Appendix B.

We currently believe the reason why we were unable to obtain results using the FBPS was related to the entire substrate surface becoming modulated by the incident optical excitation beam. Using the structure from Appendix C this effect would be removed due to the localized LTG-GaAs transmitter and receiver regions. Reattempting this experiment using the device from Appendix C could have significant impact because prototyping speeds would drastically increase and 1550 nm excitation is typically more desirable (due to component availability).

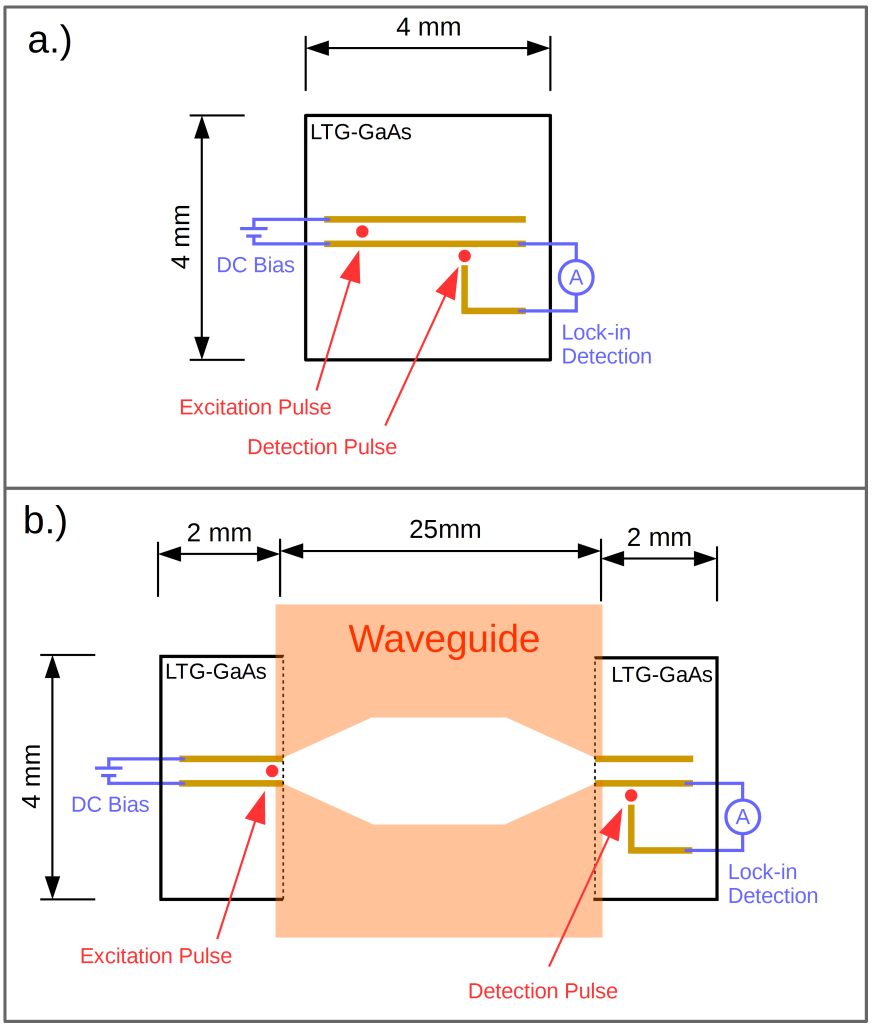

Figure 4.2: FBPS experiment schematic. a) Stage one of FBPS experiment. b) Proposed stage two of FBPS experiment.

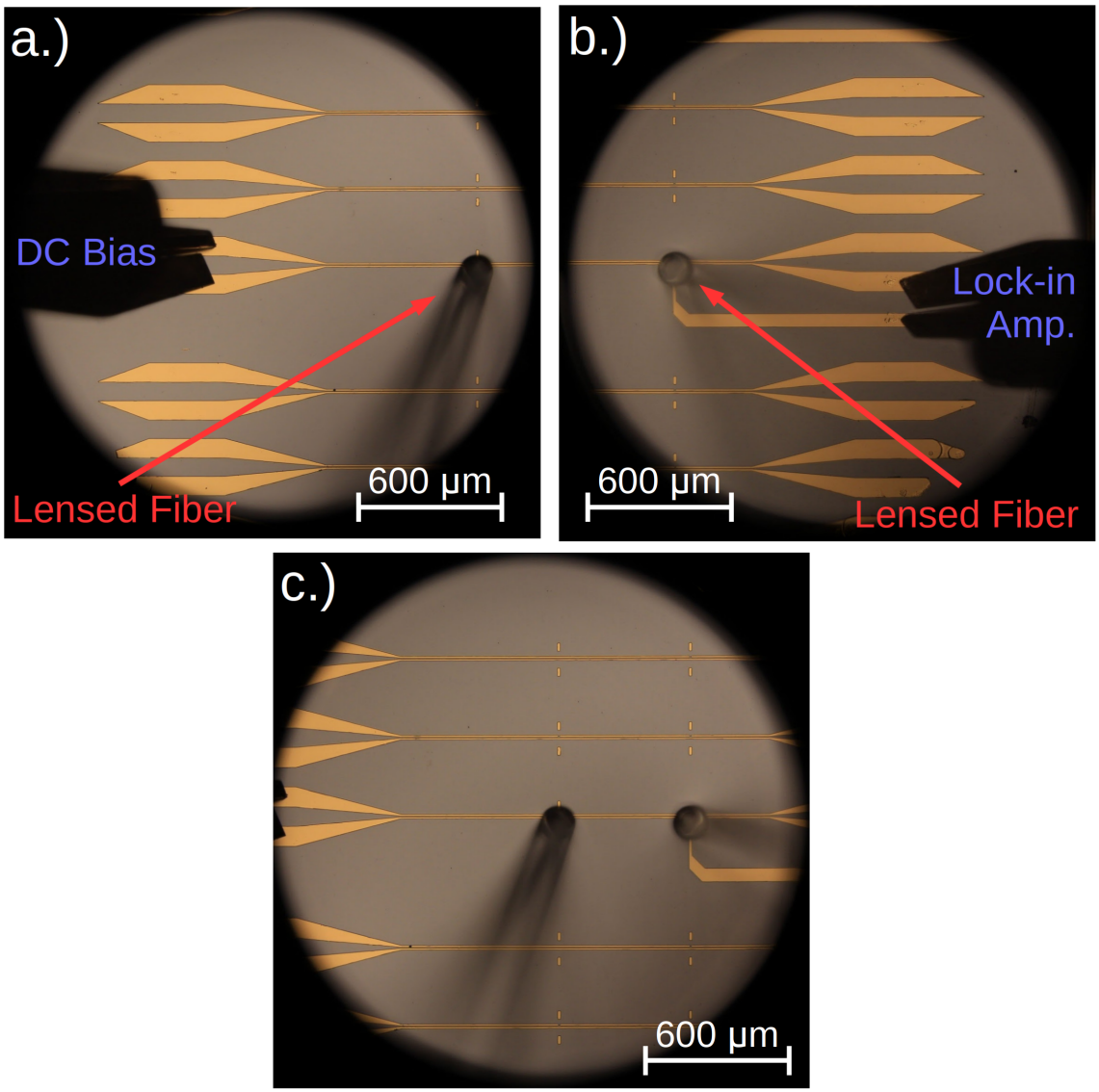

Figure 4.3: Pictures of FBPS experiment on LTG-GaAs. a) Transmitter b) Receiver c) Transmitter/Receiver overlap.

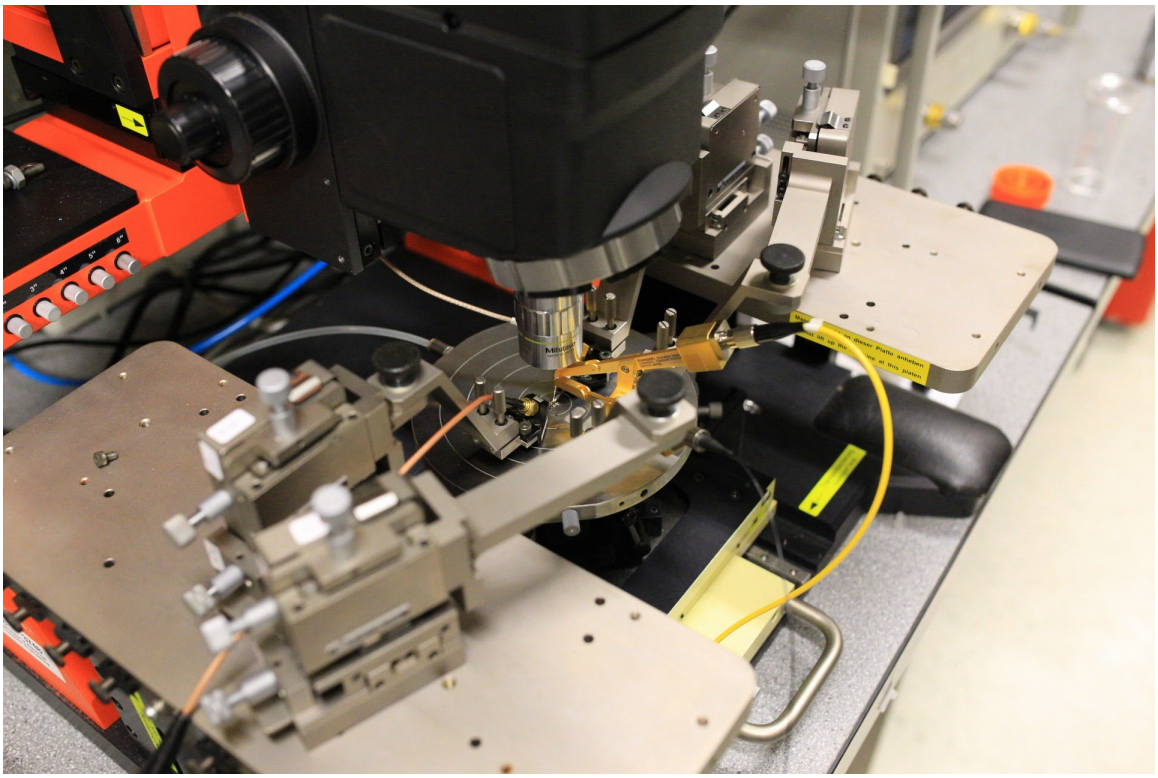

Figure 4.4: FBPS overall image.

4.1.4 Optical Waveguides on Silicon Nitride Membrane

In Appendix C a basic CPS on a thin silicon nitride membrane was investigated. The optical pump was delivered using free-space optics. In the future optical waveguides could be lithographically defined on the membrane surface and directed to the LTG-GaAs regions. This would allow for a pigtailed package to be manufactured which would be desirable in a CW system.

Bibliography

[1] R. Smith, A. Jooshesh, J. Zhang, and T. Darcie. THz-TDS using a photoconductive free-space linear tapered slot antenna transmitter. *Optics Express*, 25(9):10118, 2017.

[2] R. Smith, A. Jooshesh, J. Zhang, and T. Darcie. Photoconductive generation and detection of THz-bandwidth pulses using near-field coupling to a free-space metallic slit waveguide. *Optics Express*, 25(22):26492, 2017.

[3] Y.-H. Lee. *Principles of Terahertz Science and Technology*. Springer, 2009.

[4] M. Asada and S. Suzuki. Room-temperature oscillation of resonant tunneling diodes close to 2 THz and their functions for various applications. *Journal of Infrared, Millimeter, and Terahertz Waves*, 37(12):1185–1198, 2016.

[5] Q. Lu, D. Wu, S. Sengupta, S. Slivken, and M. Razeghi. Room temperature continuous wave, monolithic tunable THz sources based on highly efficient mid-infrared quantum cascade lasers. *Scientific Reports*, 6(1), 2016.

[6] N.T. Yardimci, S. Cakmakyapan, S. Hemmati, and M. Jarrahi. A high-power broadband terahertz source enabled by three-dimensional light confinement in a plasmonic nanocavity. *Scientific Reports*, 7(1), 2017.

[7] B. Ferguson and X.-C. Zhang. Materials for terahertz science and technology. *Nature Materials*, 1(1):26–33, 2002.

[8] I. E. Gordon and et. al. The HITRAN2016 molecular spectroscopic database. *Journal of Quantitative Spectroscopy and Radiative Transfer*, 203:3–69, 2017.

[9] R. Smith. Terahertz field enhancement by optimized coupling and adiabatic tapering, *M.A.Sc Thesis*, University of Victoria, BC, Canada, 2014.

[10] D.H. Auston, K.P. Cheung, and P.R. Smith. Picosecond photoconducting hertzian dipoles. *Applied Physics Letters*, 45(3):284–286, 1984.

[11] E.R. Brown, K.A. McIntosh, K.B. Nichols, and C.L. Dennis. Photomixing up to 3.8 THz in low-temperature-grown GaAs. *Applied Physics Letters*, 66(3):285–287, 1995.

[12] A. Nahata, A.S. Weling, and T.F. Heinz. A wideband coherent terahertz spectroscopy system using optical rectification and electro-optic sampling. *Applied Physics Letters*, 69(16):2321–2323, 1996.

[13] J. Ward, E. Schlecht, G. Chattopadhyay, A. Maestrini, J. Gill, F. Maiwald, H. Javadi, and I. Mehdi. Capability of THz sources based on schottky diode frequency multiplier chains. In *2004 IEEE MTT-S International Microwave Symposium Digest (IEEE Cat. No.04CH37535)*. IEEE.

[14] A. Dobroiu, M. Yamashita, Y.N. Ohshima, Y. Morita, C. Otani, and K. Kawase. Terahertz imaging system based on a backward-wave oscillator. *Applied Optics*, 43(30):5637, 2004.

[15] B. Knyazev, G. Kulipanov, and N. Vinokurov. Novosibirsk terahertz free electron laser: instrumentation development and experimental achievements. *Measurement Science and Technology*, 21(5):054017, 2010.

[16] B.S. Williams. Terahertz quantum-cascade lasers. *Nature Photonics*, 1(9):517–525, 2007.

[17] D. Rutledge and M. Muha. Imaging antenna arrays. *IEEE Transactions on Antennas and Propagation*, 30(4):535–540, 1982.

[18] R. Paschotta. *Encyclopedia for Photonics and Laser Technology*. Wiley, 2014.

[19] E. Brown, F. Smith, and K. McIntosh. Coherent millimeter-wave generation by heterodyne conversion in low-temperature-grown gaas photoconductors. *Journal of Applied Physics*, 73:1480, 1993.

[20] I. Gregory, C. Baker, W. Tribe, I. Bradley, M. Evans, E. Lindfield, A. Davies, and M. Missous. Optimization of photomixers and antennas for continuous-wave terahertz emission. *IEEE Journal of Quantum Electronics*, 41:717–728, 2005.

[21] M. Tani, S. Matsuura, K. Sakai, and S.I. Nakashima. Emission characteristics of photoconductive antennas based on low-temperature-grown GaAs and semi-insulating GaAs. *Applied Optics*, 36:7853–7859, 1997.

[22] P.Y. Han and X.-C. Zhang. Coherent, broadband midinfrared terahertz beam sensors. *Applied Physics Letters*, 73(21):3049–3051, 1998.

[23] Y.C. Shen, P.C. Upadhya, H.E. Beere, E.H. Linfield, A.G. Davies, I.S. Gregory, C. Baker, W.R. Tribe, and M.J. Evans. Generation and detection of ultrabroadband terahertz radiation using photoconductive emitters and receivers. *Applied Physics Letters*, 85(2):164–166, 2004.

[24] S. Dexheimer, editor. *Terahertz Spectroscopy: Principles and Applications*. CRC Press, 2008.

[25] D. Pozar. *Microwave Engineering*. Wiley, 4th edition, 2011.

[26] Keysight. Basics of measuring the dielectric properties of materials, *Application Note*, 2017.

[27] D.B. Rutledge, D.P. Neikirk, and D.P. Kasilingham. *Infrared and Millimeter Waves*, volume 10, part II. Academic, New York, 1983.

[28] D.P. Kasilingam and D.B. Rutledge. Surface-wave losses of coplanar transmission lines. In *MTT-S International Microwave Symposium Digest*. MTT005, 1983.

[29] M.Y. Frankel, S. Gupta, J.A. Valdmanis, and G.A. Mourou. Terahertz attenuation and dispersion characteristics of coplanar transmission lines. *IEEE Transactions on Microwave Theory and Techniques*, 39:910 – 916, 1991.

[30] R. Mendis and D. Grischkowsky. Undistorted guided-wave propagation of subpicosecond terahertz pulses. *Optics Letters*, 26:846–848, 2001.

[31] K. Wang and D. Mittleman. Metal wires for terahertz wave guiding. *Nature*, 432:376–379, 2004.

[32] M.K. Mbonye, R. Mendis, and D.M. Mittleman. A terahertz two-wire waveguide with low bending loss. In *Conference on Lasers and Electro-Optics 2010*. OSA, 2010.

[33] M. Wachter, M. Nagel, and H. Kurz. Metallic slit waveguide for dispersion-free low-loss terahertz signal transmission. *Applied Physics Letters*, 90:061111, 2007.

[34] H. Han, H. Park, M. Cho, and J. Kim. Terahertz pulse propagation in a plastic photonic crystal fiber. *Applied Physics Letters*, 80:2634, 2002.

[35] C. Yeh, F. Shimabukuro, and P.H. Siegel. Low-loss terahertz ribbon waveguides. *Applied Optics*, 44(28):5937, 2005.

[36] T. Jeon, J. Zhang, and D. Grischkowsky. Thz sommerfeld wave propagation on a single metal wire. *Applied Physics Letters*, 86:161904, 2005.

[37] M. Walther, M.R. Freeman, and F.A. Hegmann. Metal-wire terahertz time-domain spectroscopy. *Applied Physics Letters*, 87(26):261107, 2005.

[38] A. Markov and M. Skorobogatiy. Two-wire terahertz fibers with porous dielectric support. *Optics Express*, 21(10):12728, 2013.

[39] H. Pahlevaninezhad, T. Darcie, and B. Heshmat. Two-wire waveguide for terahertz. *Optics Express*, 18:7415–7420, 2010.

[40] M. Mbonye, R. Mendis, and D.M. Mittleman. A terahertz two-wire waveguide with low bending loss. *Applied Physics Letters*, 95(23):233506, 2009.

[41] A. Markov, H. Guerboukha, and M. Skorobogatiy. Hybrid metal wire–dielectric terahertz waveguides: challenges and opportunities. *Journal of the Optical Society of America B*, 31(11):2587, 2014.

[42] D.R. Grischkowsky. Optoelectronic characterization of transmission lines and waveguides by terahertz time-domain spectroscopy. *IEEE Journal of Selected Topics in Quantum Electronics*, 6(6):1122–1135, 2000.

[43] H.-J. Cheng, J.F. Whitaker, T.M. Weller, and L.B. Katehi. Terahertz-bandwidth characteristics of coplanar transmission lines on low permittivity substrates. *IEEE Transactions on Microwave Theory and Techniques*, 42(12):2399–2406, 1994.

[44] M. Wachter, M. Nagel, and H. Kurz. Metallic slit waveguide for dispersion-free low-loss terahertz signal transmission. *Applied Physics Letters*, 90:061111, 2007.

[45] R. Mendis. Comment on "low-loss terahertz ribbon waveguides". *Applied Optics*, 47(23):4231, 2008.

[46] R. Mendis and D.M. Mittleman. Comparison of the lowest-order transverse-electric (TE1) and transverse-magnetic (TEM) modes of the parallel-plate waveguide for terahertz pulse applications. *Optics Express*, 17:14839–14850, 2009.

[47] H. Cheng, J.F. Whitaker, T.M. Weller, and L.B. Katehi. Terahertz-bandwidth pulse propagation on a coplanar stripline fabricated on a thin membrane. *IEEE Microwave and Guided Wave Letters*, 4(3):89–91, 1994.

[48] D.R. Grischkowsky, M.B. Ketchen, C.-C. Chi, I.N. Duling, N.J. Halas, J.-M. Halbout, and P.G. May. Capacitance free generation and detection of subpicosecond electrical pulses on coplanar transmission lines. *IEEE Journal of Quantum Electronics*, 24(2):221–225, 1988.

[49] I. S. Gregory, C. Baker, W. R. Tribe, M. J. Evans, H. E. Beere, E. H. Linfield, A. G. Davies, and M. Missous. High resistivity annealed low-temperature GaAs with 100 fs lifetimes. *Applied Physics Letters*, 83(20):4199–4201, 2003.

[50] E. Yablonovitch, D.M. Hwang, T.J. Gmitter, L.T. Florez, and J.P. Harbison. Van der waals bonding of GaAs epitaxial liftoff films onto arbitrary substrates. *Applied Physics Letters*, 56(24):2419–2421, 1990.

[51] A. Baca and C. Ashby. *Fabrication of GaAs Devices*. IET, 2005.

[52] Microchem. *LOR/PMGI Datasheet*. Rev. A.

[53] R.D.V.Ríos, S. Bikorimana, M. A. Ummy, R. Dorsinville, and S-W. Seo. A bow-tie photoconductive antenna using a low-temperature-grown GaAs thin-film on a silicon substrate for terahertz wave generation and detection. *Journal of Optics*, 17(12):125802, 2015.

[54] M. Wachter, M. Nagel, and H. Kurz. Low-loss terahertz transmission through curved metallic slit waveguides fabricated by spark erosion. *Applied Physics Letters*, 92(16):161102, 2008.

[55] J. Ramer, F. Ospald, G. Freymann, and R. Beigang. Generation and detection of terahertz radiation up to 4.5THz by low-temperature grown GaAs photocon-

ductive antennas excited at 1560nm. *Applied Physics Letters*, 103(2):021119, 2013.

[56] A. Jooshesh, L. Smith, M. Shirazi, V. Yekta, T. Tiedje, T. Darcie, and R. Gordon. Nanoplasmonics enhanced terahertz sources. *Optics Express*, 22(23):27992, 2014.

[57] H. Erlig, S. Wang, T. Azfar, A. Udupa, H.R. Fetterman, and D.C. Streit. LT-GaAs detector with 451 fs response at 1.55 μm via two-photon absorption. *Electronics Letters*, 35(2):173, 1999.

[58] M. Tani, K.-S. Lee, and X.-C. Zhang. Detection of terahertz radiation with low-temperature-grown GaAs-based photoconductive antenna using 1.55 μm probe. *Applied Physics Letters*, 77(9):1396–1398, 2000.

[59] T. Kataoka, K. Kajikawa, J. Kitagawa, Y. Kadoya, and Y. Takemura. Improved sensitivity of terahertz detection by GaAs photoconductive antennas excited at 1560 nm. *Applied Physics Letters*, 97(20):201110, 2010.

Appendix A

Copy of [1]

THz-TDS Using a Photoconductive Free-Space Linear Tapered Slot Antenna Transmitter

ROBERT SMITH,[1,*] AFSHIN JOOSHESH,[1] JINYE ZHANG[1], AND THOMAS DARCIE [1]

[1]*Department of Electrical and Computer Engineering, University of Victoria, Victoria, BC, Canada, V8P 5C2*
[*]*levismit@uvic.ca*

Abstract: A near-field edge-coupled photoconductive free-space linear tapered slot antenna has been constructed as a planar alternative to the standard photoconductive switch coupled to a silicon substrate lens. The temporal response along the optical axis is investigated to ensure the structure itself does not introduce pulse distortion which would fundamentally limit the usefulness of the structure. Experimental results show that a 1.6 THz bandwidth with a ≈50dB dynamic range is achievable with the new structure which is comparable to our reference experiment with a standard silicon substrate lens. The investigated structure has the added benefit of a potential substantial physical size reduction and can also be used to excite waveguides in the near-field.

OCIS codes: (300.6495) Terahertz Spectroscopy; (250.3140) Integrated optoelectronic circuits; (250.5530) Pulse propagation and temporal solitons; (250.6715) Switching.

References and links

1. D. H. Auston, K. P. Cheung, and P. R. Smith, "Picosecond photoconducting hertzian dipoles," Appl. Phys. Lett. **45**, 284 (1984).
2. A. P. DeFonzo, M. Jarwala, and C. Lutz, "Transient response of planar integrated optoelectronic antennas," Appl. Phys. Lett. **50**, 1155 (1987).
3. A. P. DeFonzo and C. R. Lutz, "Optoelectronic transmission and reception of ultrashort electrical pulses," Appl. Phys. Lett. **51**, 212 (1987).
4. Y. Pastol, G. Arjavalingam, J. Halbout, and G. Kopcsay, "Characterisation of an optoelectronically pulsed broadband microwave antenna," Electronics Letters **24**, 1318–1319 (1988).
5. S. Gearhart, H. Ekstrom, P. Acharya, E. Kollberg, S. Jacobsson, and G. Rebeiz, "Submillimeter-wave endfire slotline antennas," in "Antennas and Propagation Society International Symposium," (1992), pp. 18–25.
6. G. Rebeziz, "Millimeter-wave and terahertz integrated circuit antennas," Proceedings of the IEEE **80**, 1748–1770 (1992).
7. C. Fattinger and D. Grischkowsky, "Point source terahertz optics," Appl. Phys. Lett. **53**, 1480 (1988).
8. C. Fattinger. and D. Grischkowsky, "Terahertz beams," Appl. Phys. Lett. **54**, 490 (1989).
9. M. W*ä*chter, M. Nagel, and H. Kurz, "Tapered photoconductive terahertz field probe tip with subwavelength spatial resolution," Appl. Phys. Lett. p. 041112 (2009).
10. M. Nagel, A. Michalski, and H. Kurz, "Contact-free fault location and imaging with on-chip terahertz time-domain reflectometry," Optics Express **19**, 12509–12514 (2011).
11. S. Sawallich, B. Globisch, C. Matheisen, M. Nagel, R. Dietz, and T. G*ö*bel, "Photoconductive terahertz near-field detectors for operation with 1550-nm pulsed fiber lasers," IEEE Transactions on Terahertz Science and Technology **6**, 365 – 370 (2016).
12. K. Wang and D. Mittleman, "Metal wires for terahertz wave guiding," Nature **432**, 376–379 (2004).
13. J. Deibel, K. Wang, M. Escarra, and D. Mittleman, "Enhanced coupling of terahertz radiation to cylindrical wire waveguides," Optics express **14**, 279–290 (2006).
14. J. Deibel, M. Escarra, N. Berndsen, K. Wang, and D. Mittleman, "Finite-element method simulations of guided wave phenomena at terahertz frequencies," in "Proceedings of the IEEE," , vol. 95 (2007), vol. 95, pp. 1624–1640.
15. D. Rutledge, *"Integrated Circuit Antennas," in Infrared and Millimeter Waves, vol. 10, Millimeter Components and Techniques, Part II* (New York: Academic, 1983).
16. M. W*ä*chter, M. Nagel, and H. Kurz, "Metallic slit waveguide for dispersion-free low-loss terahertz signal transmission," Applied Physics Letters **90**, 061111 (2007).
17. M. W*ä*chter, M. Nagel, and H. Kurz, "Low-loss terahertz transmission through curved metallic slit waveguides fabricated by spark erosion," Appl. Phys. Lett. **92**, 161102 (2008).
18. H. Zhan, R. Mendis, and D. M. Mittleman, "Thz energy confinement in finite-width parallel-plate waveguides," in "Conference on Lasers and Electro-Optics/International Quantum Electronics Conference," (2009).

19. S. Pandey, G. Kumar, and A. Nahata, "Slot waveguide-based splitters for broadband terahertz radiation," Optics Express **18**, 23466–23471 (2010).
20. H. Zhan, R. Mendis, and D. M. Mittleman, "Characterization of the terahertz near-field output of parallel-plate waveguides," JOSA B **28**, 558–566 (2011).
21. R. Smith, F. Ahmed, A. Jooshesh, J. Zhang, M. Jun, and T. Darcie, "Thz field enhancement by antenna coupling to a tapered thick slot waveguide," Journal of Lightwave Technology **32**, 15878 (2014).
22. M. Tani, S. Matsuura, K. Sakai, and S. Nakashima, "Emission characteristics of photoconductive antennas based on low-temperature-grown gaas and semi-insulating gaas," Applied Optics **36**, 7853–7859 (1997).
23. D. Schaubert, E. Kollberg, T. Korzeniowski, and T. Thungren, "Endfire tapered slot antennas on dielectric substrates," IEEE Transactions on Antennas and Propagation **33**, 1392 – 1400 (1985).
24. M. Y. Frankel, S. Gupta, J. A. Valdmanis, and G. A. Mourou, "Terahertz attenuation and dispersion characteristics of coplanar transmission lines," IEEE Transactions on Microwave Theory and Techniques **39**, 910 – 916 (1991).
25. "Batop, www.batop.com," .

1. Introduction

Terahertz photoconductive (PC) switches have existed for a number of years and were investigated as early as 1984 [1]. In [1] two PC switches were placed on opposing sides of the same substrate and did not include free-space propagation. Subsequently, extensive research was pursued in free-space antenna design and optimization. At this point two approaches appeared for collimating the generated THz field: guided-wave electronic antennas [2–6] and optical lensing from a point source [7, 8].

The work completed by [2–4] uses substrate slotline and coplannar strip antennas. These antennas function admirably but distort the temporal response due to reflections and the refractive index mismatch on the guiding interface. The induced pulse distortion limits the ability for these antennas to function as a broadband THz time-domain spectrometer (THz-TDS) source. In [5, 6] the undesired effects associated with the substrate are mitigated by using a slotline antenna on a thin dielectric membrane. This method functions well but has several issues: the resulting antenna is delicate, manufacturing requires harsh etchants, and the conductor loss is relatively high. The issues associated with guided-wave antennas are mostly overcome by optical lensing [7, 8] which therefore became the dominate method for guiding the electromagnetic field generated by a photoconductive switch. The main issues associated with substrate lenses are: pulse attenuation and dispersion, lens manufacturing, alignment, physical size, and cost.

In this paper we investigate a hybrid photoconductive structure which is edge-coupled in the near-field region to a guided-wave metallic-slit antenna termed a *photoconductive free-space linear tapered slot antenna* (PC-FS-LTSA). Near-field coupling methods have existed for a number of years, although they are commonly found in the form of near-field probes for surface characterization [9–11]. The PC-FS-LTSA overcomes many of the issues associated with substrates lens and guided-wave antennas. The PC-FS-LTSA can be small (2mm $\times$ 2mm $\times$ 5mm), inexpensive (eg. fabrication using precision stamping), and easily assembled using a top-down alignment. Providing that the pulse shape remains undistorted at the output of the antenna, the PC-FS-LTSA could be a viable alternative to a substrate lens. Thus the pulse distortion along the optical axis of a prototype PC-FS-LTSA is investigated is this paper.

The novelty of the PC-FS-LTSA presented here arises from its simplicity and performance as a THz-TDS transmitter in the absence of refractive THz optical components. The same near-field edge-coupled source can be used as an alternative method (to [12–14]) for exciting waveguides without THz optics.

2. Design

Standard photoconductive antennas (PCAs) are commonly coupled to a high-resistivity float-zone (HRFZ) silicon lens to overcome the total internal reflection (TIR) of substrate back-face and direct the THz field [15]. It is desirable to eliminate the need for a HRFZ-Si lens because they are

costly, lossy, and introduce dispersion thus limiting the transmitted power and bandwidth. Here we focus on the design of a PC-FS-LTSA for near-field edge-coupled THz antenna excitation as an alternative to the standard HRFZ-Si lens.

Figure 1 illustrates the PC-FS-LTSA which consists of a photoconductive active-area on SI-GaAs which is edge coupled to a metallic-slit based antenna [16–21] (i.e. the FS-LTSA). The photoconductive active-area was patterned using standard UV-lithography and the metalization (15nm Ti, 150nm Au) was fabricated using E-beam deposition and lift-off. A SI-GaAs substrate was selected for its low-cost, high DC resistivity and high responsivity to 785nm [22].

The metalization pattern was selected to bias the active-area and guide the generated THz field into the FS-LTSA. It was found through simulation that the geometry illustrated in Fig. 1(b) was able to couple to the FS-LTSA without significant pulse distortion.

The FS-LTSA should be relatively thin (T≈50μm) to reduce the Fabry-Pérot resonances (see Appendix A) yet maintain mechanical rigidity and minimize conductor loss. In this work the FS-LTSA is constructed out of a relatively long (L≈15mm) and thick (T≈127μm) copper sheet because hand-polishing a short (L<5mm) and thin (T≈50μm) copper sheet was found to be difficult. For this proof-of-concept experiment a FS-LTSA was selected (instead of, for example, a broadband Vivaldi taper [23]) for the manufacturing convenience. The FS-LTSA can be easily constructed by-hand whereas a Vivaldi taper requires precision machining.

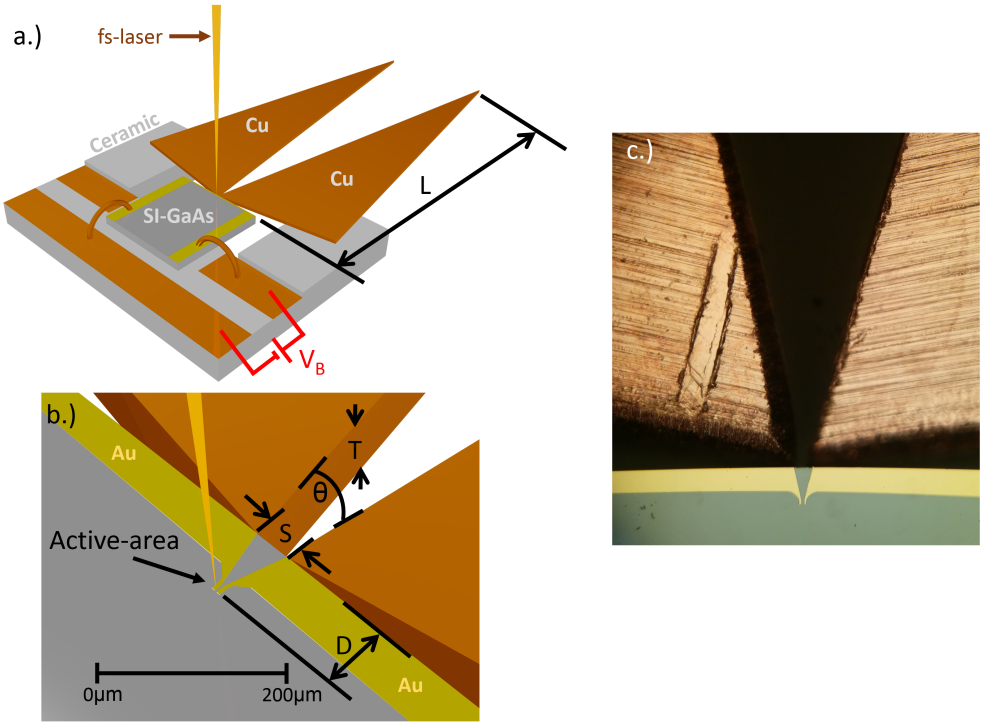

Fig. 1. Design of the PC-FS-LTSA. a) Overall structure b) Active-area to FS-LSTA c) Image of experimental structure where T≈127μm, S≈45μm, D≈85μm, L≈15mm, and θ ≈28°

A key difference between this work and past work [2–4] is the usage of a metallic-slit based *free-space* LTSA. A free-space antenna has a number of advantages over planar substrate based antennas. In particular, after the field is coupled to the FS-LTSA, the effect of substrate radiation, surface-waves, and dispersion are mostly eliminated. This goal has been mostly achieved by [5] where substrate etching was used to create an antenna on a thin (<2μm) SiO_2/Si_3N_4 membrane.

The antenna presented here has some distinct advantages over thin membrane antennas: the metallic-slit based antenna has lower conductor loss due to increased conductor surface area, it is less delicate due to the material and thickness, and the manufacturing process doesn't require harsh etchants (EDP, HF, etc). Other substrate-based antennas [2–4] which closely model coplanar strip/slotline configurations can have a total loss of ≈17dB/mm at 1 THz [24], whereas the free-space metallic-slit geometry has a loss of <1dB/mm at 1 THz [16]. To note, these numbers are not representative of all designs, but they illustrate the possible large difference between the expected losses.

The loss of a metallic slit waveguide is dependent on the conductor material, separation, and thickness. For the copper FS-LTSA used in this experiment a FEM simulation was used to estimate the loss. Given the FS-LTSA dimensions at the entrance to the antenna (T=127μm, S=45μm, f=1THz), the loss is 0.11dB/mm. As the FS-LTSA expands (S increases) the field localization on the conductors reduces resulting in a lower loss. The antenna presented here provides an excellent alternative to membrane-based antennas and illustrates that a guided-wave antenna can be used as a THz-TDS transmitter.

3. Simulation

The design of the PC-FS-LTSA was aided by simulations performed using the Ansys HFSS transient solver which utilizes the Discontinuous Galerkin Time Domain (DGTD) method. Key observations that resulted from the simulations were: the existence of a transverse Fabry-Pérot resonance in the FS-LTSA which will disperse the THz pulse (cavity length=T), a resonance between the PC active-area and the FS-LTSA edge (cavity length=D), combination of both cavities (cavity length = D+T). To summarize, the thickness of the FS-LTSA should be selected to minimize the Fabry-Pérot resonances while maintaining some thickness to reduce conductor loss. Also the active-area should be close to the substrate edge.

Figure 2 illustrates the simulated E-field of the PC-FS-LTSA after transient excitation. Figure 3(b) plots the simulated pulse shape at the output of the PC-FS-LTSA. The active-area in the simulation is modeled by a current pulse with a rise time of 800fs. The simulation illustrates that relatively few resonances are introduced by the waveguide and metalization geometries.

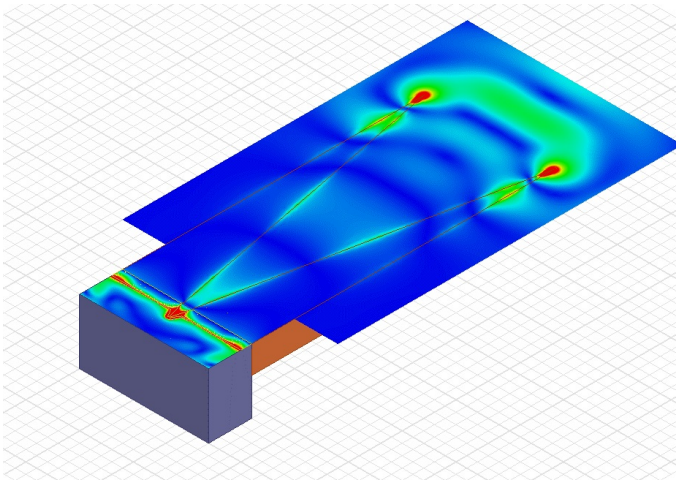

Fig. 2. Transient simulation with Ansys HFSS which illustrates the E-field

Note that the length, L, of the simulated structure is 2.25mm, whereas the experimental structure has a length of 15mm. The shorter length in the simulation was required to solve the

simulation with an acceptable resolution. This is not expected to have a large effect on THz pulse because as the conductors separation increases the field confinement on the conductors reduces resulting in a radiated wave [23].

The discrepancy between the experimental and simulated length may cause concern thus further elaboration is warranted. To reiterate, the manufactured PC-FS-LTSA length was selected purely based on manufacturing convenience. Given that this paper is an investigation of the temporal response along the optical axis, then the main requirement is that the conductor separation at the end of the FS-LTSA is much greater than the free-space pulse length. The conductor separation at the end of the experimental PC-FS-LTSA is ≈7.5mm and ≈1.1mm for simulated structure, both of which are multiple times greater than the free-space pulse length (≈0.3mm). The effects associated with the different lengths will appear in the off-axis field components which are not investigated is this paper. Appendix B illustrates the simulated results for a number of LTSA lengths and concludes that when the length of the LTSA is longer than 2.1mm the temporal and spectral responses are relatively unaffected.

4. Experiment

We used a standard THz-TDS arrangement [Fig. 3(a)] to investigate the PC-FS-LTSA's performance. A 1570nm fiber laser with a 100mW average power producing 100fs pulses at 38MHz was used. The 1570nm beam is frequency doubled using a periodically-polled lithium niobate (PPLN) crystal resulting in ≈20mW at 785nm to excite the photoconductors. Then the optical beam is split into two paths to excite the transmitter and gate the receiver.

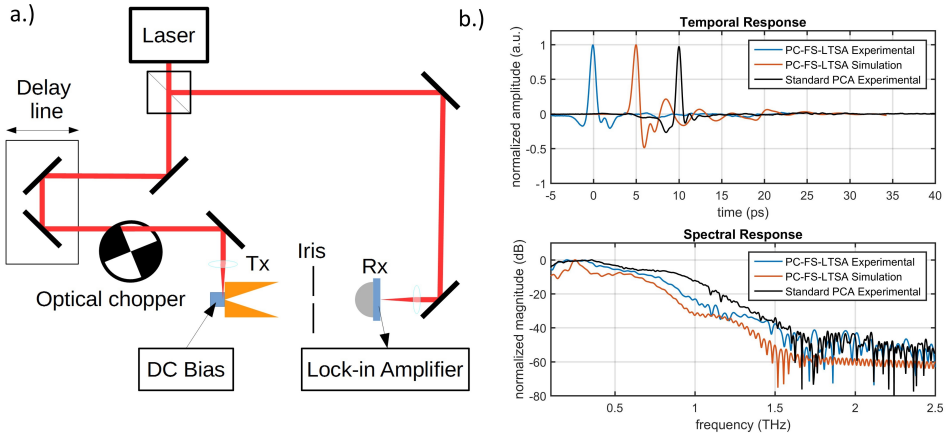

Fig. 3. a) Experimental setup for testing the PC-FS-LTSA. The active-area consisted of a 5×5μm area biased by 20V$_{dc}$. The average optical power focused onto the transmitter and receiver were 6mW and 7mW, respectively. The iris (opening = 5mm diameter) was placed midway between the transmitter and receiver which were separated by 10cm. The optical chopper was set at 1.1kHz. The receiver was connected to the current input of a lock-in amplifier. b) Experimental and simulated response obtained from the setup

The transmitter optical beam path length can be varied using a mechanical delay line which is used to obtain the temporal response of THz field. The optical beam passes through an optical chopper, then afterwards the optical beam is focused onto the active-area to generate a THz field which is coupled to the FS-LTSA then radiated. Then the THz beam is passed through an iris to block or scatter off-axis wavefront components. This increases the detectable bandwidth but reduces the detectable power. A portion of the THz beam reaches and biases the commercial LT-GaAs PCA receiver [25] and the detected current is read by a lock-in amplifier.

An identical experiment was performed with a PCA transmitter (identical to receiver) in-place of the PC-FS-LTSA to provide a comparison. The results of this experiment are plotted in Fig. 3(b).

5. Discussion

The temporal response [Fig. 3(b)] of the PC-FS-LTSA resembles that of a standard PCA which is desirable. The bandwidth of the PC-FS-LTSA reaches around 1.6THz which is admirable considering the simplicity of the design. It is also expected that the PC-FS-LTSA should become lossy at higher frequencies due excitation of transverse Fabry-Pérot modes (see Appendix A). This effect is most clearly observed by comparing the experimental PC-FS-LTSA and standard PCA spectral responses.

A notable feature in Fig. 3(b) is the presence of the water vapor absorption lines which are observable around 1.26THz. Presence of these absorption lines indicate that the PC-FS-LTSA is capable of functioning as a THz-TDS source. These lines do not originate from the previously stated Fabry-Pérot resonance because the "cavity" has a relatively low Q.

When comparing the simulated and experimental results [Fig. 3(b)] an obvious discrepancy is observed. For the simulated results the pulse has a strong negative portion whereas for the experiment this is minor. This is expected since the simulation defines the source as an impulse, whereas a SI-GaAs transmitter has a slow carrier decay (step-like response) resulting in a small negative peak [22]. Also note that the simulation peak at ≈0.255THz originates from a cavity (length=D+T, $n_e \approx \sqrt{(12.9+1)/2} = 2.64$) which is stronger for the simulated structure due to ideal edges.

Referring to Fig. 3(b), a common trait of a LTSA is observed. After the initial transient, a small "double hump" occurs which is characteristic of the LTSA [2]. The double hump is undesirable because it broadens the pulse thus limiting the bandwidth. The simple method to eliminate this feature is to use a Vivaldi taper instead of a linear taper. A small hump also appears for the standard PCA before and after the main pulse. This typically arises from imperfect substrate lens alignment.

The bandwidth of the PC-FS-LTSA could be increased by correcting non-idealities with the following adjustments: utilize a thinner FS-LTSA (T≈50μm), reduce the distance between the active-area and the FS-LTSA (D≈10μm), and use a Vivaldi taper.

Regarding the physical size of the PC-FS-LTSA simulation shows that the length could be reduced to, for example, the simulated size (L=2.25mm) without causing pulse distortion. Therefore the total structure could quite likely fit into a volume ≈5mm × 2mm × 2mm = 20mm^3 which is significantly less than the volume of a typical PCA coupled to a silicon lens ≈10mm × 10mm × 5mm = 500mm^3.

6. Conclusion

If the thickness of the FS-LTSA is adequately selected for the anticipated system bandwidth then the generated THz pulse should not exhibit signs of pulse distortion, thus illustrating that the PC-FS-LTSA could be a useful alternative to a substrate lens. Experimental results have shown that a ≈1.6THz bandwidth with a ≈50dB dynamic range can be achieved. Water vapor absorption lines can be resolved which confirms that the PC-FS-LTSA is a functional THz-TDS transmitter.

The PC-FS-LTSA allows for a planar THz setup which could be used for imaging or spectroscopy in a less bulky arrangement than current implementations which utilize PCAs coupled to a HRFZ-Si lenses.

Appendix A - Fabry-Pérot Resonance

The Fabry-Pérot modes can be excited when a thick (with respect to wavelength) metallic slit waveguide is used. Figure 4(a-b) illustrates the results of a time-domain simulation that shows

the Fabry-Pérot resonance when the metallic slit is thick. The start and stop frequency of the excitation pulse are 0.3 and 3THz respectively. Figure 4(c-d) illustrates the removal of the resonance by reducing the thickness of the metallic slit waveguide. Figure 4(d) illustrates the desired undistorted response.

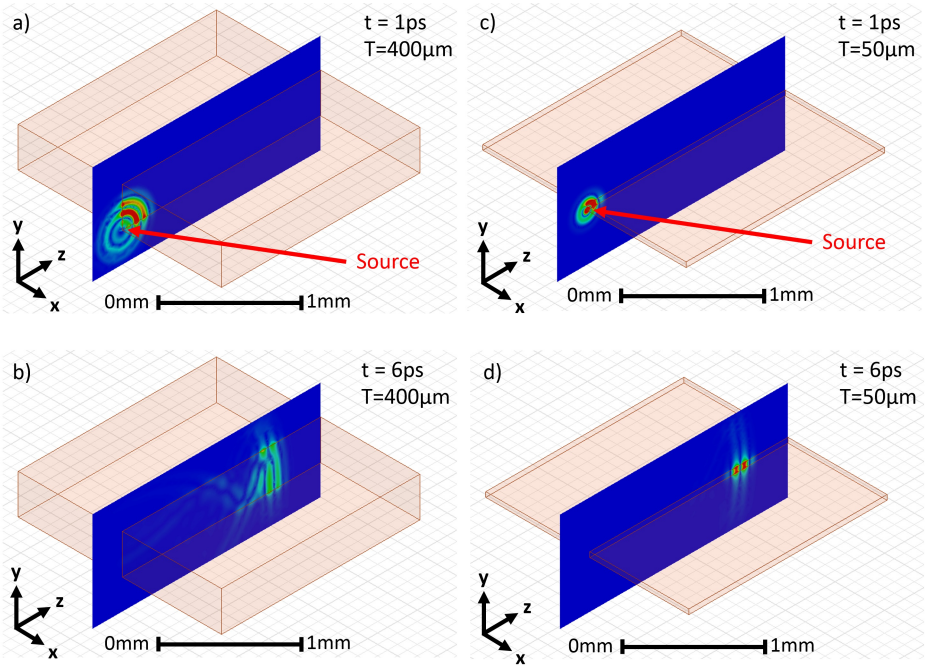

Fig. 4. Transient E-field plot illustrating the Fabry-Pérot resonance. a) Thick waveguide, field profile around the source location just after excitation (t=1ps) b)Thick waveguide, field profile of guided-wave after 6ps, note that the field profile is dispersed by reflections. c) Thin waveguide, field profile around the source location just after excitation (t=1ps) d) Thin waveguide, field profile of guided-wave after 6ps, note that the field profile is relatively undispersed and confined to the waveguide.

Appendix B - FS-LTSA length

Figure 5 plots the temporal response for various FS-LTSA lengths. When the length of the FS-LTSA exceeds 2.1mm there is little change in the radiated temporal response. To note, the simulated structure in Fig. 5 does not include the substrate/FS-LTSA interaction (as found in Fig. 2 and Fig. 3(b)). The substrate was negated because the high dielectric constant of the substrate demands a finer mesh (more computational resources) which would limit our simulation structure size to less than 3.3mm. Also, the structure was excited by a current sheet (closely matched to fundamental mode) instead of a current line to minimize the Fabry-Pérot resonance as discussed in Appendix A. The noise floor of the various lengths are different due to nonidentical meshes at convergence and does not contribute much insight to the comparison as it models an extremely small portion of the injected energy.

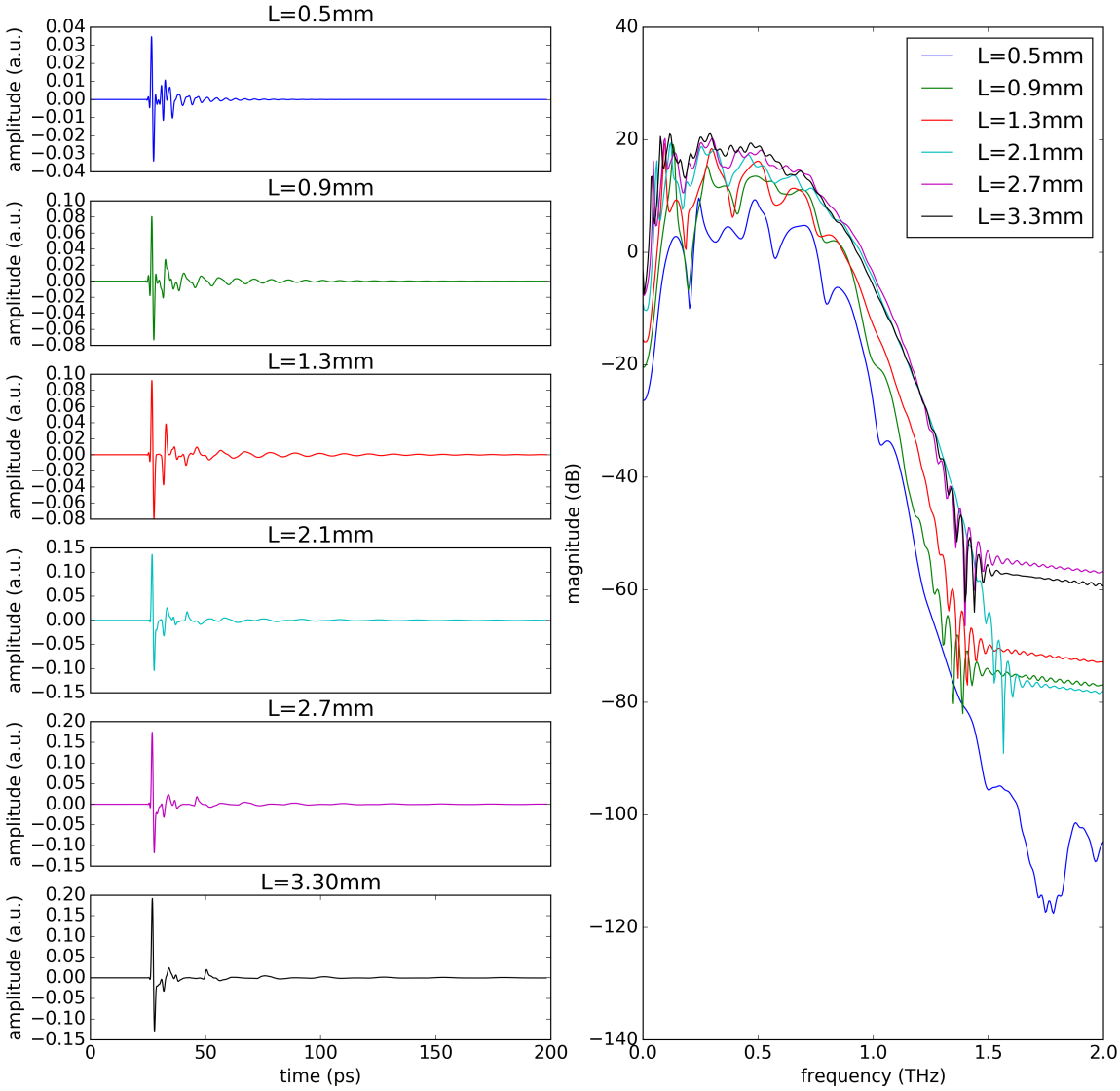

Fig. 5. The radiated temporal response sampled along the optical axis for a selection of LTSA lengths and the associated spectral response.

Funding

This work was supported by funding from the Natural Science and Engineering Research Council (NSERC) Canada.

Appendix B

Copy of [2]

Photoconductive generation and detection of THz-bandwidth pulses using near-field coupling to a free-space metallic slit waveguide

ROBERT SMITH,[1,*] AFSHIN JOOSHESH,[1] JINYE ZHANG[1], AND THOMAS DARCIE [1]

[1]*Department of Electrical and Computer Engineering, University of Victoria, Victoria, BC, Canada, V8P 5C2*
[*]*levismit@uvic.ca*

Abstract: THz-bandwidth pulses are generated, transmitted along a gold-plated stainless steel metallic slit waveguide, and detected with 1.5 THz bandwidth and 60 dB dynamic range. The source and detector were edge-pumped slotlines on LT-GaAs placed within the near-field region of the waveguide entrance and exit aperture. The motivation for this work was to develop a complete dispersion-free THz system which was simple to manufacture and could be utilized for free-space waveguide experimentation.

OCIS codes: (300.6495) Terahertz Spectroscopy; (250.3140) Integrated optoelectronic circuits; (250.5530) Pulse propagation and temporal solitons; (250.6715) Switching.

References and links

1. D. Auston, "Impulse response of photoconductors in transmission lines," IEEE Journal of Quantum Electronics **19**, 639–648 (1983).
2. D. Auston, *Picosecond Photoconductors: Physical Properties and Applications* (1984).
3. M. B. Ketchen, D. Grischkowsky, T. C. Chen, C.-C. Chi, I. N. Duling, N. J. Halas, J.-M. Halbout, J. A. Kash, and G. P. Li, "Generation of subpicosecond electrical pulses on coplanar transmission lines," Applied Physics Letters **48**, 751–753 (1986).
4. D. Grischkowsky, M. Ketchen, C.-C. Chi, I. Duling, N. Halas, J.-M. Halbout, and P. May, "Capacitance free generation and detection of subpicosecond electrical pulses on coplanar transmission lines," IEEE Journal of Quantum Electronics **24**, 221–225 (1988).
5. D. Krökel, D. Grischkowsky, and M. B. Ketchen, "Subpicosecond electrical pulse generation using photoconductive switches with long carrier lifetimes," Applied Physics Letters **54**, 1046–1047 (1989).
6. D. Rutledge, D. Neikirk, and D. Kasilingam, *Integrated-Circuit Antennas* (1983).
7. J. Nees, S. Williamson, and G. Mourou, "100 GHz traveling-wave electro-optic phase modulator," Applied Physics Letters **54**, 1962–1964 (1989).
8. H. Cheng, J. Whitaker, T. Weller, and L. Katehi, "Terahertz-bandwidth pulse propagation on a coplanar stripline fabricated on a thin membrane," IEEE Microwave and Guided Wave Letters **4**, 89–91 (1994).
9. M. W*ä*chter, M. Nagel, and H. Kurz, "Metallic slit waveguide for dispersion-free low-loss terahertz signal transmission," Applied Physics Letters **90**, 061111 (2007).
10. M. W*ä*chter, M. Nagel, and H. Kurz, "Low-loss terahertz transmission through curved metallic slit waveguides fabricated by spark erosion," Appl. Phys. Lett. **92**, 161102 (2008).
11. R. Smith, F. Ahmed, A. Jooshesh, J. Zhang, M. Jun, and T. Darcie, "Thz field enhancement by antenna coupling to a tapered thick slot waveguide," Journal of Lightwave Technology **32**, 15878 (2014).
12. R. Smith, A. Jooshesh, J. Zhang, and T. Darcie, "THz-TDS using a photoconductive free-space linear tapered slot antenna transmitter," Optics Express **25**, 10118 (2017).
13. H. Zhan, R. Mendis, and D. M. Mittleman, "Superfocusing terahertz waves below $\lambda/250$ using plasmonic parallel-plate waveguides," Optics Express **18**, 9643 (2010).
14. M. W*ä*chter, M. Nagel, and H. Kurz, "Tapered photoconductive terahertz field probe tip with subwavelength spatial resolution," Appl. Phys. Lett. p. 041112 (2009).
15. S. Sawallich, B. Globisch, C. Matheisen, M. Nagel, R. Dietz, and T. G*ö*bel, "Photoconductive terahertz near-field detectors for operation with 1550-nm pulsed fiber lasers," IEEE Transactions on Terahertz Science and Technology **6**, 365 – 370 (2016).
16. M. Nagel, A. Michalski, and H. Kurz, "Contact-free fault location and imaging with on-chip terahertz time-domain reflectometry," Optics Express **19**, 12509–12514 (2011).
17. G. Veronis and S. Fan, "Modes of subwavelength plasmonic slot waveguides," Journal of Lightwave Technology **25**, 2511–2521 (2007).

18. J. Xiao, Q.-Q. Wei, D.-G. Yang, P. Zhang, N. He, G.-Q. Zhang, and X.-P. Chen, "Hybrid plasmonics slot THz waveguide for subwavelength field confinement and crosstalk between two waveguides," IEEE Journal of Selected Topics in Quantum Electronics **23**, 1–5 (2017).
19. M. Wächter, M. Nagel, and H. Kurz, "Tapered photoconductive terahertz field probe tip with subwavelength spatial resolution," Applied Physics Letters **95**, 041112 (2009).
20. S. Gupta, M. Y. Frankel, J. A. Valdmanis, J. F. Whitaker, G. A. Mourou, F. W. Smith, and A. R. Calawa, "Subpicosecond carrier lifetime in GaAs grown by molecular beam epitaxy at low temperatures," Applied Physics Letters **59**, 3276–3278 (1991).
21. Y.-H. Lee, *Principles of Terahertz Science and Technology* (Springer, 2009).
22. L. Duvillaret, F. Garet, J.-F. Roux, and J.-L. Coutaz, "Analytical modeling and optimization of terahertz time-domain spectroscopy experiments, using photoswitches as antennas," IEEE Journal of Selected Topics in Quantum Electronics **7**, 615–623 (2001).

1. Introduction

Photoconductive pulse generation and detection on a substrate was investigated in the 1980s [1–5]. In [1] the theory of photoconductive pulse generation and detection was investigated. This theory was expanded upon in [2] where experimental results were provided. In [3] THz-bandwidth pulses are generated and transmitted along an 8mm coplanar transmission line and the "sliding contact" excitation method was introduced. The results of [3] are re-analyzed in [4] and conclude that a sliding contact source or detector can have no capacitance. In [5] the sliding contact is slightly modified to generate short pulses from a long-carrier-lifetime substrate. This was achieved by asymmetrically exciting the transmission line.

In the previously cited work the transmission lines consisted of metallic contacts deposited on a thick dielectric substrate. This configuration is undesirable because of leaky-wave radiation [6]. Leaky-wave radiation can be minimized by reducing the waveguide width or homogenizing the dielectric. To approximate a homogeneous dielectric a superstrate with same dielectric constant as the substrate can be placed [7], or the substrate can be thinned (<2 μm) to approximate the loss and dispersion of an air dielectric [8].

In this paper we use a metallic slit waveguide (MSWG) for low-loss and dispersion-free waveguiding [9–13]. In [9–11] a relatively thick (>300 μm) MSWG was excited by coupling the radiated field generated by a photoconductive switch. In [12] near-field excitation of a relatively thin (127 μm) copper MSWG was performed and used as a linear tapered slot antenna. In other works [14–16] near-field detectors have been utilized for surface conductivity and transverse field mapping. Plasmonic MSWGs have also been investigated in the optical [17] and THz regimes [18].

The novelty of this paper arises from the designed THz system. The system provides an effective and simplistic method for generating, transmitting, and detecting dispersion-free THz-bandwidth pulses which is not found elsewhere. The method of waveguide excitation is similar to past work [12], but here the THz source is a DC biased edge-pumped slotline which minimizes the pulse distortion by eliminating reflections associated with the bias lines. THz field transmission along a free-space MSWG is found elsewhere [9–12], but in this work a thinner gold-plated steel MSWG is utilized for broadband transmission. Also the MSWG includes tapers to reduce attenuation which is unique to this work. THz field detection is achieved by tapering the MSWG onto an edge-pumped slotline detector which located within the near-field region of the exit aperture of MSWG. We were unable to find a similar detector in other work. Other near-field detectors exist [14–16] which could potentially be utilized, but the manufacturing procedure for these detectors is difficult in comparison to a simple cleaved slotline.

2. Design

We have designed a THz system [Fig. 1] which uses a MSWG to overcome the issue of leaky-wave radiation, loss, and dispersion associated with substrate-based waveguides. The MSWG and

slotline are excited by an optical pulse illuminating the biased slotline [Fig. 1(b)]. The generated field is transmitted along the MSWG and detected at the receiver [Fig. 1(c)]. Cross-sections of the MSWG and slotline are shown in Figs. 1(e)-1(f). Figure 1(d) illustrates the configuration of the experimental structure.

The thickness, T, of the MSWG should be selected based on the system bandwidth and excitation configuration. In [12] we identified detrimental Fabry-Pérot oscillations which are excited when a thick MSWG is asymmetrically excited by a current line (similar to the source presented here). These oscillations are present when the MSWG thickness, T, is comparable to the spatial pulse length in the metallic-slit waveguide (which is the same as the spatial pulse length in air because n≈1). For example, if a MSWG is excited with a 0.5 ps pulse then T $\ll 150\mu$m.

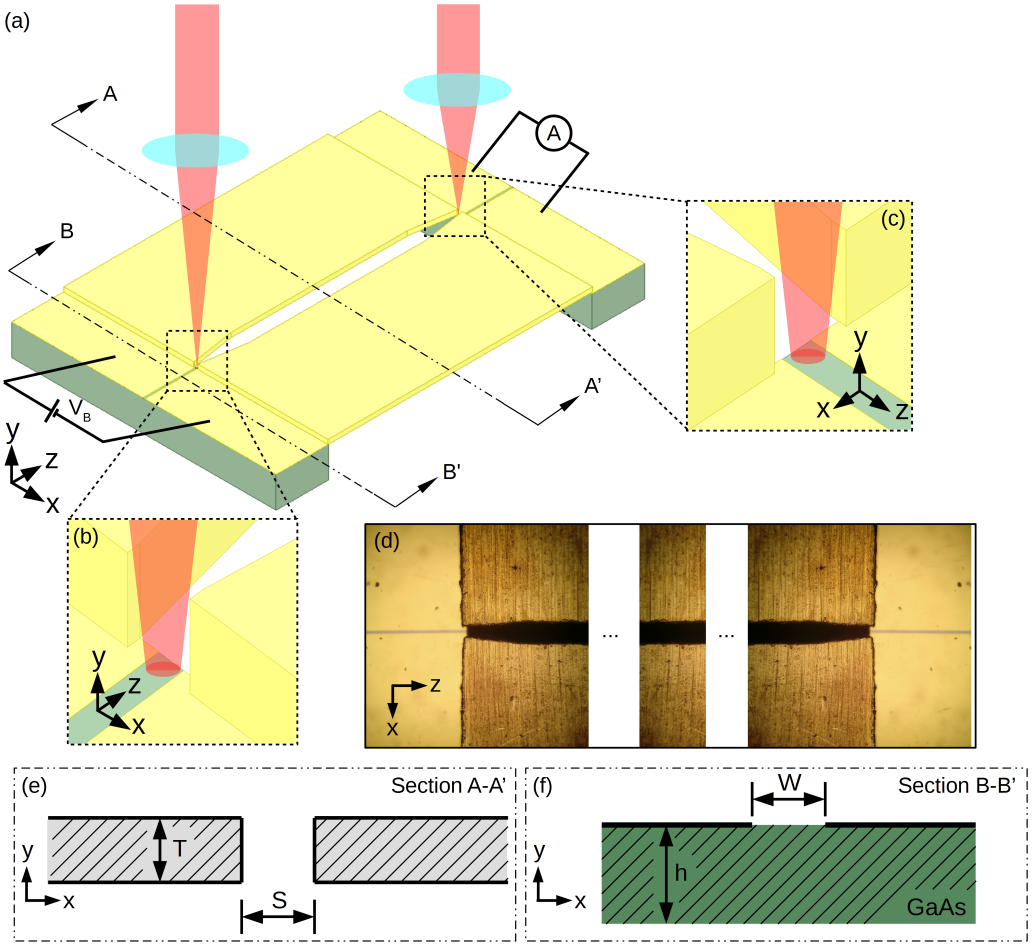

Fig. 1. Design of the THz system. (a) Overall structure. (b) Transmitter active area and optical excitation location. (c) Receiver active area and optical excitation location. (d) Configuration of experimental structure (top-down view). (e) Cross-section of MSWG and definitions. (f) Cross-section of slotline and definitions.

Figure 2 illustrates the circuit diagram which approximates the THz system. A DC bias voltage (90 V) is applied to the transmitter active area using a slotline. The transmitter active area is illuminated by a femtosecond optical pulse resulting in a conductance spike in $g_1(t)$. The current spike through $g_1(t)$ drives both the slotline and MSWG. Ideally no power should be delivered to

the slotline but this is difficult to incorporate without introducing unwanted resonances due to discontinuous bias lines. A portion of the signal is near-field coupled across an air-gap from the slotline into the MSWG which travels along a tapered section of waveguide to reach a geometry with a lower attenuation coefficient. To maximize the signal coupled into the MSWG from the slotline the air-gap should be small [Fig. 5]. To minimize the radiation into free-space (and maximize coupling into the MSWG) the separation, S, at the start of the taper should be close to the slotline gap width (W = 20 μm) or slightly larger (such that the active area is not blocked from the optical pump). The MSWG was positioned by-hand and we were able to achieve S = 80 μm which proved to be sufficient since we detected a signal. For the work presented here we selected to use a slight taper so the field remains confined to an area close to a free-space pulse width. Given that we were able to achieve S = 80 μm this corresponded to S = 160 μm based on our pre-machined MSWG plates which gives an appreciable reduction in the attenuation coefficient [Fig. 3]. After the taper the pulse travels the length of the MSWG for 24 mm before tapering to the receiver. A portion of the signal couples to the receiver which generates a detectable DC current proportional to the product of the incident signal voltage and receiver conductance. The cross-correlation trace is produced by sweeping the relative time delay between the two signals (i.e. via an optical delay line).

The MSWG material and thickness was selected to have acceptable mechanical strength and Fabry-Pérot oscillation reduction. As the waveguide becomes thinner the bend strength degrades but the adverse effects of Fabry-Pérot oscillations are minimized. In the limit of T $\rightarrow$ 0 μm, the metallic slit becomes a free-space slotline and the oscillations are eliminated, but this is impossible to achieve (or approximate) while maintaining mechanical strength. Copper with a thickness less than 100 μm is delicate therefore steel was used. The MSWG was fabricated using 0.002" (T = 51 μm) 304 stainless steel via wire electrical discharge machining (EDM) then gold-plated (plating thickness $\approx$ 1.5 μm).

The THz source and detector are identical W = 20 μm slotlines made of Ti/Au (5 nm/100 nm) RF sputtered on a 1 μm low-temperature Gallium Arsenide (LT-GaAs) epilayer. LT-GaAs is a sub-picosecond carrier-lifetime photoconductive material [20] which is commonly used for detecting THz pulses. The LT-GaAs epilayer was grown on a semi-insulating Gallium Arsenide (SI-GaAs) substrate (h = 350 μm) which was annealed for 60 seconds at 600°C. Slotlines were selected because they do not introduce unwanted cavity resonances and are simple to manufacture (lithography, deposition, lift-off, then cleave at any point). Compared to our previous source [12], we expect that the transmitter losses a portion of the power to the slotline but the signal transmitted into the MSWG will have less distortion.

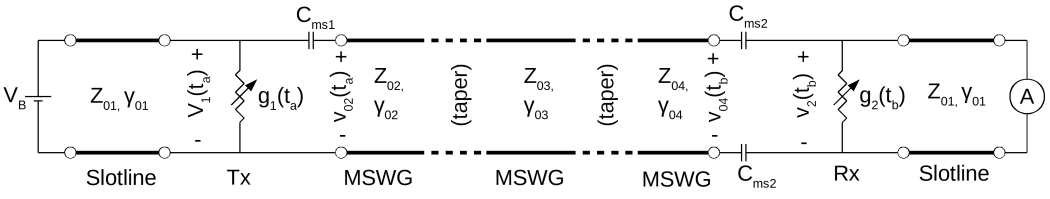

Fig. 2. Transmission line representation of circuit

3. Simulation

The structure was simulated in both time and frequency domain using Ansys HFSS v18. For all time-domain simulations the substrates are lossless GaAs with the relative permittivity set to ϵ_r = 12.9 and the conductors set to PECs. For the frequency-domain simulation the substrates are lossless GaAs with the relative permittivity set to ϵ_r = 12.9 and the MSWG conductors

are set to gold with conductivity of $\sigma_{Au} = 4.1 \times 10^7 S/m$. The frequency-domain simulation was used to calculate waveguide parameters $\alpha(f, S)$ and $Z_0(f, S)$ [Fig. 3]. The attenuation coefficient is dominated by conductor loss which was determined by comparing simulations with MSWG set to a PEC and gold. The attenuation coefficient at the entrance and exit of the MSWG is α(2 THz, 80 μm) = 0.099 dB/mm. The central section has an attenuation coefficient of α(2 THz, 160 μm) = 0.054 dB/mm. The difference between these attenuation coefficients is the reason for the taper. By doubling S the attenuation coefficient is approximately halved (note this does not scale linearly).

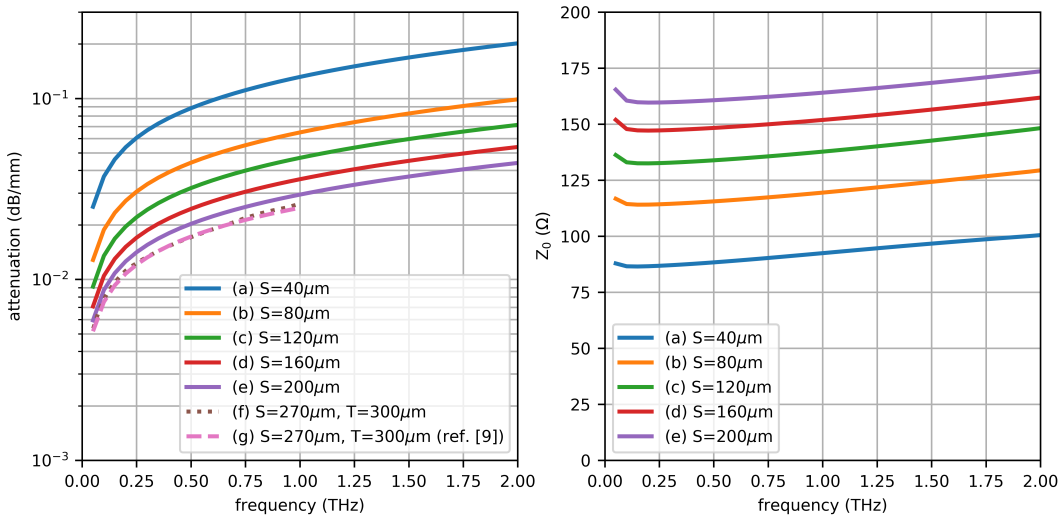

Fig. 3. MSWG attenuation solved with Ansys HFSS. The attenuation for various separations is plotted. Traces (f)-(g) are plotted to verify that our simulation results align with the results presented in [9]. The real part of the Z_{0pv} characteristic impedance is also plotted.

Time-domain simulations were used to visualize pulse coupling and transmission in a similar method to experimentation [Fig. 4]. For all transient simulations the source was a current source with the pulse shape defined by the normalized form of Eqn. 1 where the parameters where obtained from the experimental fit (τ_p = 0.21 ps, τ_c = 0.39 ps, τ_s = 0.08 ps). For the transient simulations the length of the central section of MSWG was reduced from 24 mm to 3 mm to reduce the simulation time. Videos for the transient simulations are included in the **Supplementary Material** to better illustrate the pulse propagation. The voltage at the receiver was calculated by integrating the E-field, $v_2(t) = \int \vec{E}(t) \cdot d\vec{l}$ at each time step. In Section 5 the simulated receiver voltage is used to fit the experimental data [Fig. 7].

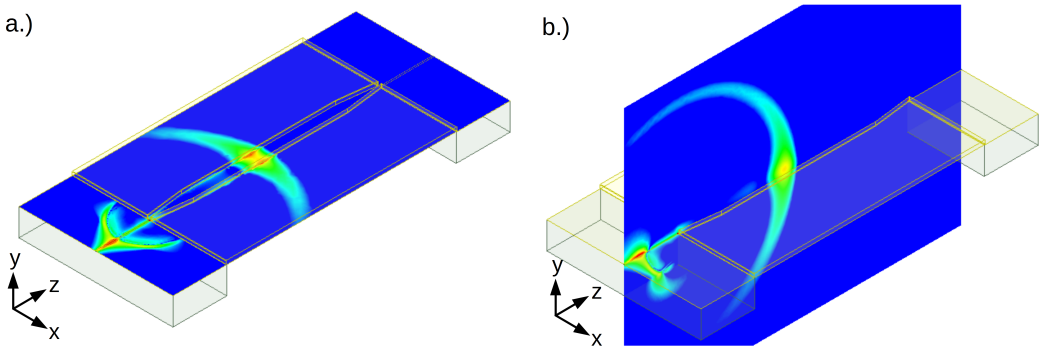

Fig. 4. Time-domain simulation illustrating the field coupled into MSWG 4 ps after excitation. The MSWG was set to a PEC. W=20μm, S=80μm→160μm. a) xz-plane (for video see **Visualization 1**). b) yz-plane (for video see **Visualization 2**).

The slotline to MSWG transition was investigated using a time-domain simulation with ideal material parameters (PECs and lossless dielectrics). The simulated structure consisted of a slotline coupled to a MSWG (without a taper or receiver). Figure 5 plots the results of the simulation which illustrates that the pulse does not get heavily distorted by the introduction of a gap and that the relative attenuation remains less than 6dB for the gap size investigated in this paper.

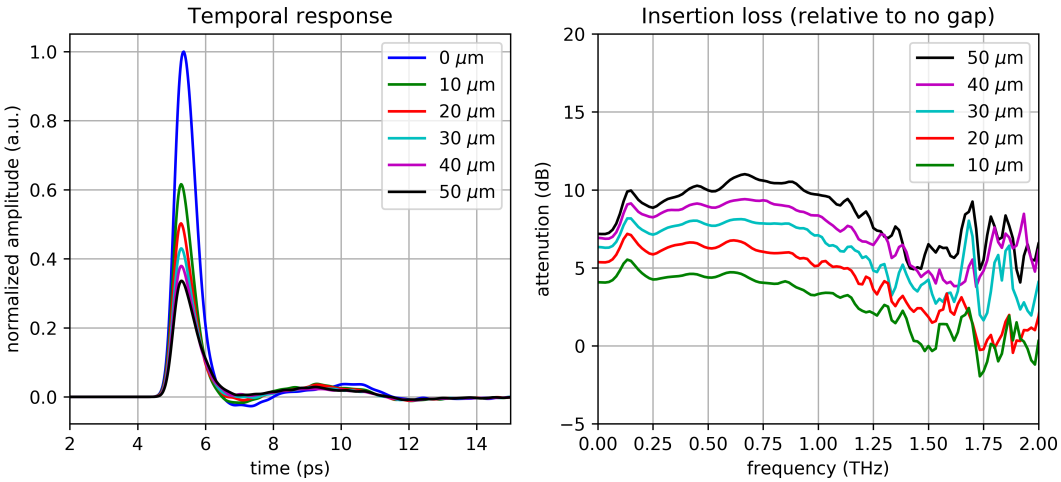

Fig. 5. Time-domain simulation which illustrates the field coupled to the MSWG from the slotline for a selection of gap sizes between the slotline and MSWG. a) Temporal response for various gap sizes normalized to the case without a gap. b) Frequency-dependent attenuation for various gap sizes relative to the case without a gap.

4. Experiment

A 780nm mode-locked femtosecond laser generated 80 fs pulses with an 80 MHz repetition for the experiment. The average optical power delivered to the transmitter and receiver was ≈15 mW. A photoconductive slotline transmitter and receiver were placed at the entrance and exit of a MSWG [Figs. 1(b)-1(c)]. The slotline and MSWG overlapped by approximately 20 μm. At the transmitter the slotline physically contacted one plate of the MSWG. At the receiver the slotline does not contact the MSWG and was separated by a small gap (≈10 μm). This configuration was

selected to minimize the low-frequency modulation of the optical chopper from being detected (which would appear as a DC offset).

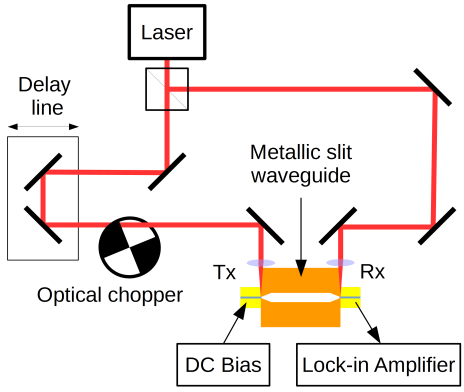

Fig. 6. Experimental setup. An 80 fs 780 nm laser beam is split into two paths, one directed to the transmitter through a mechanical delay line for THz generation, the other directed to the receiver for detection. A 25 mm MSWG connects the slotline based transmitter and receiver.

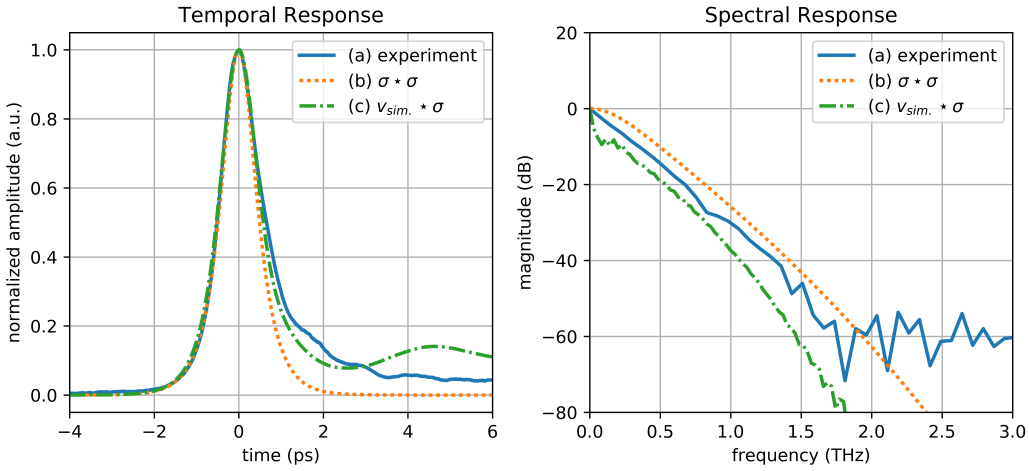

Fig. 7. Time-domain signals and respective Discrete Fourier Transform (DFT). (a) Experimental signal detected using the designed structure. (b) Autocorrelation of Eqn. 1 fitted to signal (τ_p = 0.21 ps, τ_c = 0.39 ps, τ_s = 0.08 ps). (c) Simulated response, the receiver voltage was obtained with Ansys HFSS transient, the conductivity was obtained from Eqn. 1.

5. Discussion

Figure 7 plots the measured results for the experiment illustrated in Fig. 6. The detected pulse proves that we are able generate, transmit (25 mm), and receive a THz-bandwidth pulse using a thin gold-coated steel MSWG. Use of near-field coupling of slotlines to the transmitter and receiver allows for a simple alignment with a non-resonant broadband response which is a desirable attribute for undistorted pulse transmission.

In this paper we are primarily concerned with the temporal profile of the received pulse. Many factors affect the amplitude therefore constant scaling factors are negated for curve fitting. The small signal voltage across transmitters active area is represented by $v_1(t)$, the conductance of the source active area is given by $g_1(t)$, and the substrate conductivity is given by $\sigma_1(t)$. Given that $v_1(t) \propto g_1(t) \propto \sigma_1(t)$ [4, 21, 22] the curves will be fit based on normalized Eqn. 1 [21]:

$$\sigma_1(t) \propto \exp\left(\frac{\tau_p^2}{4\tau_c^2} - \frac{t}{\tau_c}\right) \cdot \operatorname{erfc}\left(\frac{\tau_p}{2\tau_c} - \frac{t}{\tau_p}\right) - \exp\left(\frac{\tau_p^2}{4\tau_{cs}^2} - \frac{t}{\tau_{cs}}\right) \cdot \operatorname{erfc}\left(\frac{\tau_p}{2\tau_{cs}} - \frac{t}{\tau_p}\right), \quad (1)$$

where τ_p is the square-root of the sum of squares of laser pulse width and carrier transit time [4], τ_c is the substrate carrier lifetime, τ_s is the substrate momentum relaxation time, $\tau_{cs} = (\tau_c^{-1} + \tau_s^{-1})^{-1}$, and erfc(x)=1-erf(x)=$2/\sqrt{\pi}\int_x^\infty e^{-t^2}dt$.

Experimentally the average current measured at the receiver is given by the time integral of the cross-correlation [3] of the induced voltage across the receivers active area, $v_2(t)$, and the sampling substrate conductance, $g_2(t)$. To generate the plot the signal shown in Fig. 7(a) a relative delay swept between the two signals via an optical delay line.

Observation of Fig. 7 reveals that the detected pulse is a baseband signal which contains a DC component in the Discrete Fourier Transform (DFT). This may cause confusion because there are gaps between the slotlines and MSWG which should block the DC component. This can be explained by a couple points. First, the detected current, at a given delay, is obtained by the convolution of $v_2(t)$ and $g_2(t)$ which implies the average detected current does not directly correspond to $v_2(t)$. Next, given the relatively narrow temporal window (10 ps) the DC component appears large, if the temporal window length was substantially larger, the DC component would be heavily reduced. Finally, the detected signal was scaled between zero and one which modified the DC component.

Figure 7(b) was fitted to the experimental results by starting with common initial time constants (τ_p^0 = 0.18 ps, τ_c^0 = 0.5 ps, τ_s^0 = 0.03 ps) then adjusting until they fit the experimental results, which occurs when τ_p = 0.21 ps, τ_c = 0.39 ps, τ_s = 0.08 ps. Of these values the only parameter which can be easily modified is the carrier transit time (contained in τ_p) which could potentially increase the bandwidth. We selected to use a W = 20 μm slotline primarily because we had that lithography mask available. It is presumed that by reducing W, the reduced carrier transit time will result in a wider bandwidth.

Figure 7(c) is the result of a transient simulation which is numerically cross-correlated with the normalized conductivity function, Eqn. 1. Fig. 7(c) illustrates that the leading edge of the detected pulse is relatively undistorted by traversing the MSWG.

6. Conclusion

We have demonstrated THz-bandwidth pulse generation, transmission and detection over a MSWG, showing that using near-field coupling for waveguide excitation and detection can be both simple and effective. Dispersion-free transmission is achieved over 25 mm with a bandwidth of 1.5 THz. Comparison with a theoretical model suggests bandwidth is limited by carrier transit time which will be reduced in subsequent photoconductor designs.

Funding

This work was supported by funding from the Natural Science and Engineering Research Council (NSERC) Canada.

Appendix C

Copy of accepted paper

The Author Accepted Manuscript (pre-print) version is copied.

Demonstration of a low-distortion terahertz system-on-chip using a CPS waveguide on a thin membrane substrate

ROBERT SMITH AND THOMAS DARCIE*

Department of Electrical and Computer Engineering, University of Victoria, Victoria, BC V8P 5C2, Canada
*tdarcie@uvic.ca

Abstract: Distortion-free transmission of THz-bandwidth pulses over centimeter-scale distances is desirable for future THz system-on-chip (TSoC) applications. In this work we achieve this by utilizing a coplanar strip (CPS) transmission line fabricated on a thin (1 μm) silicon nitride membrane. To generate and detect the THz-bandwidth pulses we use a well-known lift-off technique to construct thousands of small (20 μm $\times$ 40 μm) thin-film LTG-GaAs photoconductive devices from a small (approx. 4 mm $\times$ 4 mm) substrate. The devices are then bonded to the CPS transmission line on the thin silicon nitride membrane, DC biased and optically pumped by a sub-picosecond laser. We demonstrate the generation and detection of a pulses containing frequencies up to 1.5 THz after propagating for 10 mm.

1. Introduction

THz technology continues to advance from the original Austin switch ([1], 1984) to support a wide variety of applications in spectroscopy, science, inspection, communications, etc. The vast majority of these applications use common photoconductive antennas (PCAs) to transmit and receive THz radiation through an optical path formed using bulk-optical THz elements. However, to decrease cost and increase performance and functionality, it is essential to develop a next generation of THz system-on-chip (TSoC) [2–6] comprising multiple THz components and functions. In analogy with MMICs operating at microwave frequencies, such TSoCs would include active devices (photoconductors, photomixers, amplifiers, mixers, etc.), passives (filters, matching elements, capacitors, chokes, etc.) and, as is the focus of this work, low-loss and non-dispersive waveguides and transmission lines.

Experiments that demonstrated sub-picosecond pulse transmission were first completed in the 1980s [1, 7]. In [7] a coplanar waveguide (CPW) fabricated on a silicon-on-sapphire (SOS) substrate was used to a transmit a subpicosecond pulse over 8 mm after which it broadened to 2.6 ps. Later in the 1990s a coplanar strip (CPS) transmission line was fabricated on a thin silicon dioxide/silicon nitride membrane which supported subpicosecond pulse transmission over 4 mm [8]. After this initial work a number of other waveguide technologies [9–12] were investigated which achieve low loss and minimal pulse distortion over relatively long distances (>24 cm). However, they are rather bulky mechanically, which limits their suitability for direct connection to active devices or precise fabrication of complex TSoC. As a result, these are typically excited by capturing a portion of the far-field radiated from a standard photoconductive antenna (PCA). Previously we utilized a different approach to achieve low loss and low dispersion THz waveguides by near-field coupling to a metallic slit waveguide [13]. However, this waveguide is still far from ideal for TSoC integration. In 2009 CPS transmission lines were investigated on low-permittivity substrates for spectroscopic applications where thin-film active regions were connected to a plastic substrate using pre-process bonding [14]. In [14] discrete active regions were bonded before the lithographically-defined transmission lines were deposited (thus requiring

mask alignment), limiting the flexibility for complex system fabrication where many discrete components may be required. Post-process bonding is desirable because the active regions can be placed onto an existing conducting circuit, which is similar to placing low-frequency surface-mount components onto a printed-circuit board (PCB). In [15] a CPS transmission line on a 400 μm thick quartz substrate was excited by post-process LTG-GaAs bonding, however only short distances were investigated ($\approx$ 1 mm).

This work is motivated by the development of a practical TSoC platform or workbench for engineering circuits for THz frequencies, circuits that may ultimately include a wide variety of active and passive components designed largely by scaling MMIC counterparts. To meet these objectives we require 1) compatibility with standard surface-mount fabrication techniques, 2) THz transmission lines with low loss and low dispersion and 3) ability to define and fabricate RF-engineered features (stubs, impedance transformers, multi-section filters, etc.) with high precision. After considerable investigation, we conclude that only approach that meets all three requirements is one similar to that reported in 1994 in [8]. Low-loss and low dispersion result from fabrication of the CPS on a thin membrane, which results in relatively weak dielectric loading, which minimizes group velocity dispersion (GVD) and Cherenkov radiation [16]. Precision is insured using standard photolithography to define circuit features.

In this paper we resurrect and extend the approach presented in [8] to demonstrate a simple example of this TSoC platform; a system consisting of a transmitter, waveguide and receiver. Several things have changed since the original 1994 work. We use thin (1 μm) silicon nitride membranes which are now commercially available over at least 1 cm $\times$ 1 cm areas, rather than the previously demonstrated oxide-clad membranes. In [8] the pulse was generated by photoconductive switching and detected by electro-optic sampling. While electro-optic sampling performs well, the optical elements required are not compatible with our TSoC objectives. Rather, we use small (40 μm $\times$ 20 μm) discrete thin-film photoconductive LTG-GaAs epi-layers as both transmitter and photoconductive receiver.

This paper combines several contributions in demonstrating the transmission of THz-bandwidth pulses and potential of this TSoC platform. Specific contributions include 1) extending prior work (mainly [8, 17]) to fabricate a non-dispersive CPS transmission line on a thin silicon nitride membrane, 2) detection of pulses containing frequencies up to 1.5 THz after propagating for 10 mm, the furthest a pulse with this bandwidth has been transmitted on a CPS, 3) demonstration, for the first time, of post-processing placement of thin-film photoconductive LTG-GaAs devices on the membrane-based CPS, 4) investigation of contact efficacy between the CPS and placed devices, 5) demonstration of a simple radiatively-coupled DC block to isolate the photoconductive receiver from relatively high DC bias voltage applied at the transmitter and 6), numerical simulation of various CPS configurations to show a path forward to lower loss and increased functionality. Taken together, these contributions demonstrate a novel technology platform that allows precise and simple fabrication of THz-bandwidth circuits. Work continues to investigate various other applications of this platform to produce membrane-based TSoCs.

2. Design

The structure investigated in this paper is a CPS transmission line on a thin (1 μm) silicon nitride membrane. Silicon nitride was selected because thin-film membranes on silicon frames are commercially available. The dielectric loss for silicon nitride is reasonable at THz frequencies (thin-film loss tangent, $\tan \delta_\varepsilon \approx 0.00526$ [18]). Note that the majority of the field is located in the surrounding air, thus the overall dielectric loss is minor. Figure 1(a) illustrates renderings of the overall structure and enlarged images of the transmitter and receiver regions are shown in Figs. 1(b)-1(c), respectively. Figure 1(d) is a microscope image of the fabricated receiver region. The cross-section of the CPS transmission line is shown in Fig. 1(e). Electrical contacts are patterned onto a commercial silicon/silicon nitride frame which is typically used for X-ray

microscopy [19]. For this experiment we used a 10 mm × 10 mm silicon nitride window on a 15 mm × 15 mm silicon frame. We were most concerned with the proof-of-concept design (not heavily optimized) so we selected waveguide dimensions (S = W = 10 μm) which would have a moderate attenuation at high frequencies while keeping the total structure dimensions (S + 2W) relatively small compared to the spatial pulse length (<300 μm) to minimize radiation losses during excitation.

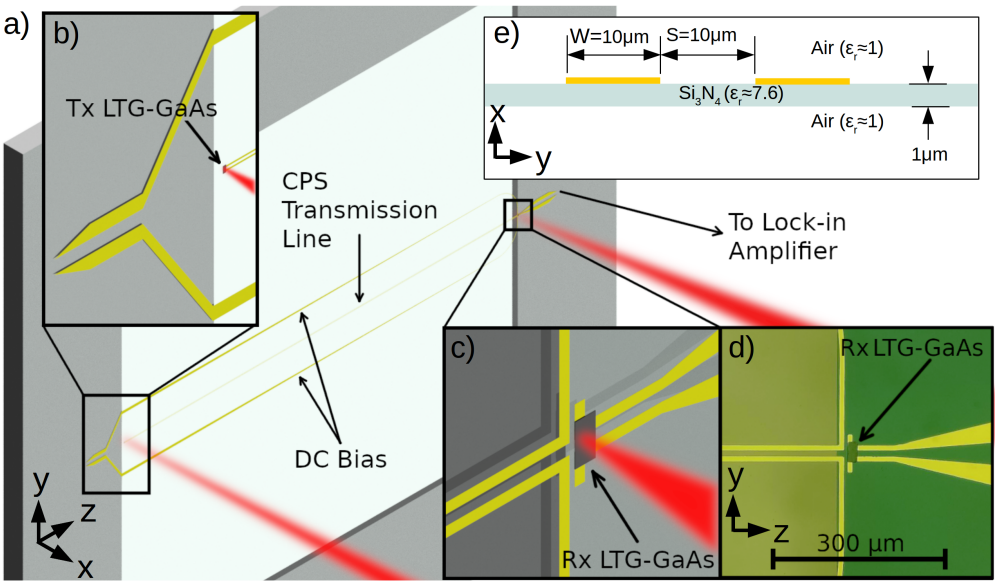

Fig. 1. Illustration of the THz platform. a) Overall structure on membrane. b) Rendering of transmitter LTG-GaAs connection. c) Rendering of receiver LTG-GaAs connection. d) Microscope image of receiver LTG-GaAs connection. e) Cross-section of CPS transmission line.

Our selected circuit configuration resembles a standard "sliding contact" transmitter except that the transmitter is located at the end of the transmission line. This excitation method is used to maximize the transmitted power towards the receiver and minimize the resonances which can occur with biasing features. The receiver is similar to a standard PCA which is placed in close proximity to the DC biasing lines. This configuration was selected because it resembles a microwave bias tee and minimizes signal distortion which occurs from resonant cavities, this was confirmed by prior simulations. The transmitter and receiver bias lines are fed from opposing sides of the silicon frame primarily such that they fit onto a probe station.

The thin-film photoconductive LTG-GaAs layer originated from a 940 nm LTG-GaAs/900 nm AlAs/650 μm semi-insulating (SI)-GaAs structure. The LTG-GaAs layer was grown at 260°C via molecular beam epitaxy (MBE). After growth the substrate was annealed at 450°C for 10 minutes. We found that these anneal conditions give subpicosecond carrier lifetimes that are in agreement with [20] (1/e carrier lifetime of ≈0.23 ps). Note that the extremely thick sacrificial AlAs layer was not required for this experiment, however the material was available. A much thinner AlAs layer (≈ 50 nm [21]) should be used to reduce substrate deterioration by oxidization.

To fabricate the LTG-GaAs photoconductive devices we used a processing method similar to that described in [17]. To summarize the procedure we first used standard photolithography, gold deposition (5 nm Ti and 100 nm Au), and lift-off. Afterwards photoresist was used to protect the active regions via mask alignment and development. Then the entire substrate was submerged in a GaAs etching solution (citric acid and hydrogen peroxide) to create an array

of mesa devices. Next an etch resistant wax was melted onto the surface, then the structure was submerged in Hydrofluoric (HF) acid which etches the sacrificial AlAs layer and releases the LTG-GaAs epilayer. The structure, still bonded to the wax, was reinserted into the GaAs etching solution until all the mesa devices were cleanly separated. The wax and structures were placed onto a Mylar membrane, then the wax was removed with Trichloroethylene (TCE). After this procedure we obtained thousands of 40 μm × 20 μm × 0.4 μm LTG-GaAs photoconductive devices which can be used as either transmitters or receivers.

3. Simulations

The transmission line was simulated in both the time and frequency domain using commercial software [22]. Time-domain simulations are used to characterize transmission-line excitation. Frequency-domain simulations are used for transmission-line design and insight. Due to the extreme dimensional ratio - a 1 μm thick membrane and a 10 mm length (1:10000) - long simulation times are required to characterize the structure in its entirety. To gain the most insight, evaluation the complex propagation constant, $\gamma = \alpha + i\beta$ is needed, where α is the attenuation coefficient and β is the phase constant. To obtain γ a 2D simulation of the transmission-line cross section is required. After γ is obtained via simulation the pulse transmission can be characterized by application of the Fourier transform:

$$\tilde{V}(z,\omega) = \tilde{V}(0,\omega)\exp(-\gamma z), \tag{1}$$

and its inverse:

$$V(z,t) = \frac{1}{2\pi}\int_{-\infty}^{\infty}\tilde{V}(z,\omega)\exp(-i\omega t)\,d\omega, \tag{2}$$

where z is the propagation distance, $\tilde{V}(0,\omega)$ is the Fourier transform of the input pulse $V(0,t)$, ω is the angular frequency, and $\tilde{V}(z,\omega)$ is the Fourier transform of the output pulse $V(z,t)$.

The following material properties are used in the simulations. For silicon nitride: the relative permittivity $\varepsilon_r = 7.6$, relative permeability $\mu_r = 1$, electrical conductivity $\sigma = 0$ S/m, and loss tangent $\tan\delta_e = 0.00526$ [18]. For the gold contacts we assumed the best case scenario with negligible surface roughness and selected the standard bulk conductivity $\sigma_{\mathrm{Au}} = 4.1 \times 10^7$ S/m. Adjustment of the transmission-line separation, S, and width, W, can greatly impact γ. To illustrate this we simulated the transmission line with various S and W values (see Fig. 2). Figure 2(a) plots the attenuation coefficient, α, which can be significant and will limit the bandwidth of the system. Note that the majority of the attenuation originates from conductor loss (confirmed by comparing simulations with perfect and gold conductors). Figure 2(b) plots the phase constant, β. The difference between the light line (vacuum/lossless propagation) and the other traces indicates the presence dielectric loading. For convenience we selected to set S equal to W, however when optimizing system performance they are unlikely to be equal, Appendix A illustrates the impact of varying the W/S ratio for a fixed cross section (S + 2W).

Thus far the simulation suggests that we should select a large CPS separation and width to achieve the best performance (i.e. S = W = 50 μm). However, as the cross-section of the transmission-line increases (i.e. S + 2W = 150 μm) more radiation will occur at the higher frequencies during excitation. Figure 3 plots the time-domain simulation results located 950 μm from the source, $V(z = 950\ \mu m, t)$, for various transmission-line widths and separations. From Fig. 3(b) it is clear that larger transmission-line cross-sections experience more loss at higher frequencies which is contrary to the data shown in Fig. 2(a). This occurs because the transmission line looks like a larger antenna during excitation (S + 2W is larger); however, once the pulse is coupled to the transmission line it will propagate with lower loss. This is the reason that we have selected to use S = W = 10 μm for the experiment (minimize radiation during excitation) although the transmission line attenuation is larger [Fig. 2(a)]. The time shift for the various

peaks in Fig. 3(a) is the result of a variation in the effective dielectric constant. For smaller cross-sections the field is more localized to the dielectric thus the group velocity is reduced. The crossing traces in Fig. 3(b) originates from the complex nature of radiation during excitation and coupling to the transmission line. Future work will investigate optimized tapering structures which minimize the radiation during excitation (i.e. S = W = 5 μm) then transform to a low-loss configuration (i.e. S = W = 50 μm) for the majority of the propagation distance. Also, we have focused on membrane thickness of 1 μm, which reduce dielectric loading adequately for the frequencies considered. Substantially thinner (e.g. down to 100 nm) membranes are available providing another dimension for investigation.

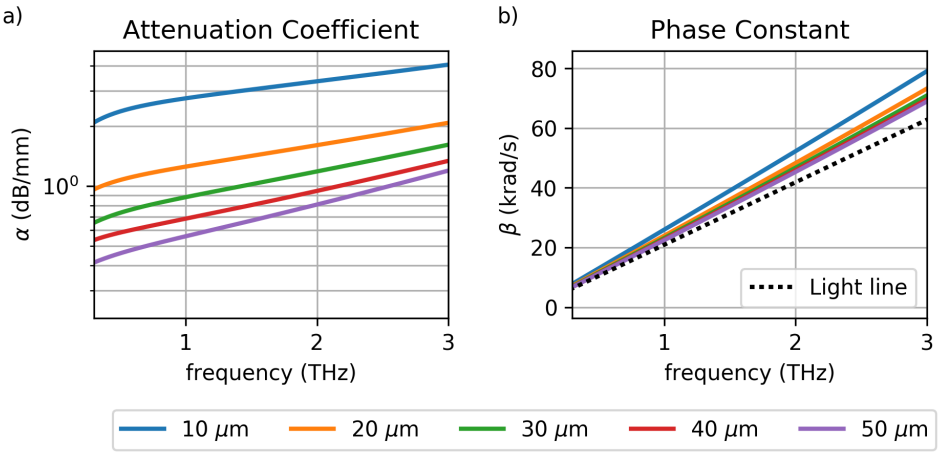

Fig. 2. Frequency-domain simulations results for a CPS transmission line on a 1 μm silicon nitride membrane with S = W = 10 μm, 20 μm, 30 μm, 40 μm, and 50 μm. a) The attenuation coefficient. b) The phase constant.

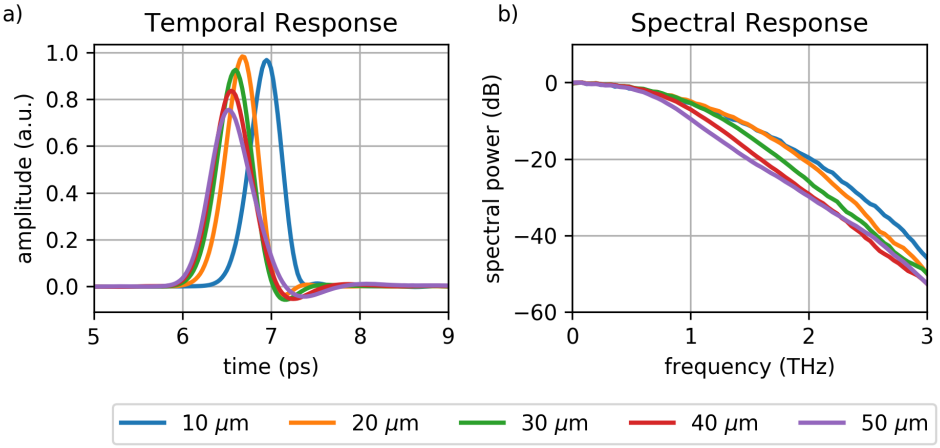

Fig. 3. Time-domain simulation results for Gaussian pulses plotted 950 μm from the source for S = W = 10 μm, 20 μm, 30 μm, 40 μm, and 50 μm. These pulses are plotted 950 μm away from the source to ensure any ringing has sufficiently decayed.

Once the complex propagation constant is known, the output pulse for an arbitrary input pulse

can be obtained by numeric application of Eqs. (1) and (2). In this work we assume the excitation pulse is of the following form [23]:

$$V(t) \propto \sigma(t) \propto \exp\left(\frac{\tau_p^2}{4\tau_c^2} - \frac{t}{\tau_c}\right) \cdot \mathrm{erfc}\left(\frac{\tau_p}{2\tau_c} - \frac{t}{\tau_p}\right) - \exp\left(\frac{\tau_p^2}{4\tau_{cs}^2} - \frac{t}{\tau_{cs}}\right) \cdot \mathrm{erfc}\left(\frac{\tau_p}{2\tau_{cs}} - \frac{t}{\tau_p}\right), \quad (3)$$

where τ_p is the laser pulse duration, τ_c is the substrate carrier lifetime, τ_s is the substrate momentum relaxation time, $\tau_{cs} = (\tau_c^{-1} + \tau_s^{-1})^{-1}$, and erfc(x)=1-erf(x)=$2/\sqrt{\pi}\int_x^\infty e^{-t^2}dt$.

We have selected to use common values for the following analysis [23]: τ_c = 0.5 ps, τ_s = 0.03 ps, and τ_p = 0.054 ps. Figure 4a plots the input and output pulses in the time domain. The input pulse is given by Eq. (3) and the output pulse is obtained by application of Eqs. (1) and (2) using the simulated complex propagation constant. Figure 4(b) plots the spectral response. It is apparent from Fig. 4(a) that the pulse both broadens and becomes attenuated after propagating 10 mm. Note that the peak amplitude of the received pulse is 0.066× the input amplitude. While the attenuation is large, if the pulse can be resolved with a reasonable signal-to-noise ratio (via a lock-in amplifier) then the transmission line can still be used to investigate circuit elements. However for longer interconnects it would be desirable to taper the transmission line to a lower loss configuration, for example, if S = W = 50 μm (not pictured) which would change the peak reduction to 0.367× the input amplitude (10 mm) - a potentially substantial improvement.

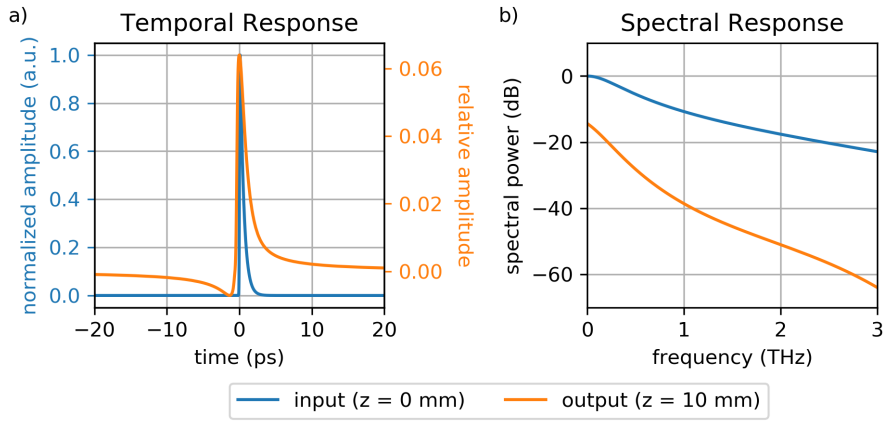

Fig. 4. Input and calculated output pulses via Fourier Transform (using simulated $\gamma(\omega)$) for S = W = 10 μm.

4. Experiment and results

The experimental setup used (Fig. 5) is similar to a standard THz-time-domain spectroscopy (TDS) measurement setup. A femtosecond laser (90 fs pulse width, 780 nm wavelength, 80 MHz repetition rate) is passed through a beam splitter; one beam is directed to the transmitter through a optical chopper (1100 Hz), the other to the receiver via a mechanical delay line. Note that we used optical chopping to remove the inductively coupled signal which is detected when using electrical chopping. The transmitter consists of a thin-film LTG-GaAs layer which has a 25 V_{DC} bias applied. The receiver contacts are connected to a lock-in amplifier which is referenced to the optical chopper in the transmitter optical path. The received pulse is plotted by sweeping the physical path length difference between transmitter and receiver. Providing that the receiver has a minimal carrier lifetime (τ_c in the subpicosecond range) it becomes possible to resolve THz-bandwidth signals, which is why LTG-GaAs ($\tau_c \approx 0.5$ ps) is used.

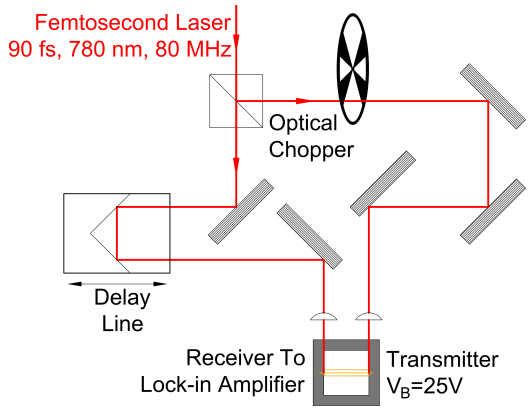

Fig. 5. Experimental setup for testing the transmission line. For the FIB-bonded experiment the optical power delivered to the transmitter and receiver is 6.2 mW and 7.4 mW, respectively. For the VDW-bonded experiment the optical power delivered to the transmitter and receiver is 1.6 mW and 2.0 mW, respectively.

Two different techniques were explored for the physical connection between the thin-film LTG-GaAs transmitter and receiver and their respective contacts on the silicon nitride membrane. Initially we bonded the transmitter and receiver similarly using the Van der Waals (VDW) technique [Fig. 6(b)] [17, 21]. In short, we placed the thin-film LTG-GaAs transmitter and receiver with their contacts touching the CPS conductors on the silicon nitride membrane, then using a micro-manipulator they were moved to their precise location (as illustrated in Fig. 1). A drop of deionized (DI) water was then placed over each, dried, then the thin-film LTG-GaAs layer was bonded to the silicon nitride membrane and gold contacts. Although there is no bonding material (i.e. Indium), after fabrication and testing this VDW-bonding technique [Fig. 6(b)] was found to function reasonably well. We were able to measure a strong photoresponse for both devices. However, with an applied DC bias, we noticed that as the optical power increased, the photocurrent would gradually become unstable, we suspect, due to heating, thus we limited the optical power to the VDW-bonded transmitter. To provide better thermal dissipation we decided to "weld" the transmitter contacts to the membrane contacts. The thin-film LTG-GaAs transmitter was removed, then a new thin-film LTG-GaAs device was placed upside-down, repositioned, and re-bonded via the VDW method except without any gold-on-gold contact. The exact same device was not reused because we were unsure if original device had become thermally damaged during testing; however, we did use a device from the same batch which performs near identically. Afterwards we directly welded the thin-film LTG-GaAs contacts onto the membrane contacts using Tungsten deposition in a Focused Ion Beam (FIB) [Fig. 6(a)]. This helped to reduce the photocurrent noise however it increased the dark current which we suspect is the result of Gallium implantation which occurred during Tungsten deposition via the FIB. With this modification higher optical powers could be used with the FIB-bonded configuration compared to the VDW-bonded configuration.

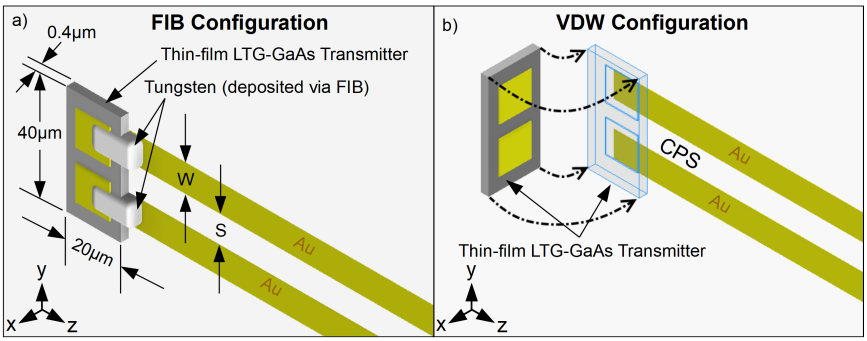

Fig. 6. Illustration of the LTG-GaAs bonding techniques. Note that the gold contact pads are both 12.5 μm $\times$ 10 μm and are separated by 5 μm, the feature resolution has a radius of curvature of 2.5 μm. a) Van der Waals bonding with FIB deposited tungsten. b) Van der Waals bonding without tungsten.

Figure 7(a) plots the received temporal pulse where the inset is focused on the normalized leading edge of the pulse. Figure 7(b) plots the spectral response (magnitude) which is obtained by applying the Fast-Fourier Transform (FFT) to the received temporal pulse. The data in Fig. 7(b) is normalized to the maximum of the FIB configuration spectrum, and the VDW configuration spectrum is shifted down by 10 dB for clarity. Note that the phase is not plotted, as is common practice in literature. For the FIB-bonded method it is evident from the spectral response that the received pulse contains frequency components which extend to 1.5 THz. For the VDW-bonded method frequencies extend up to approximately 1.0 THz. This is explained by a difference in optical power. As previously mentioned, when the optical power for the VDW-bonded transmitter increases, the photocurrent becomes noisy, likely due to heating. To mitigate this issue for the VDW-bonded method a lower optical power is used: 1.3 mW (transmitter) and 2.0 mW (receiver). For the FIB-bonded method an average optical power of 6.2 mW (transmitter) and 7.4 mW (receiver) is used. For both cases the optical beam is focused to a waist diameter of approximately 7 μm on the transmitter and receiver. Since the noise issue was not noted in past work we suspect it is occurring because we used a very thin LTG-GaAs layer (0.4 μm). We selected to use this thickness simply because the material was available to us. Past work used the following LTG-GaAs layer thicknesses: 0.8 μm in [14] and 2.0 μm in [15, 17]. Compared with the work in [14] (pre-process bonding), these post-processing bonding techniques have lower bandwidth and dynamic range; however, we did demonstrate comparable results when transmitting over a longer distance using a higher loss configuration (S = W = 10 μm compared to S = W = 20 μm in [14]). Given the large advantage in terms of fabrication (i.e. mask alignment is not necessary), post-process bonding becomes a very attractive option.

Future work will explore the two related issues, device bonding and heat dissipation. Device bonding with the FIB is undesirable due to a high processing cost and potential Gallium implantation effects, however it provides better heat dissipation. VDW bonding is desirable because of the lower cost, however it appears to not dissipate heat as effectively. Another option to improve heat dissipation is to use a thicker metalization on the thin-film LTG-GaAs devices and the CPS transmission line. Alternatively, and preferably, use of well known flip-chip bonding with Indium as a bonding material may be a useful method to provide a better bond, low contact resistance and good heat dissipation.

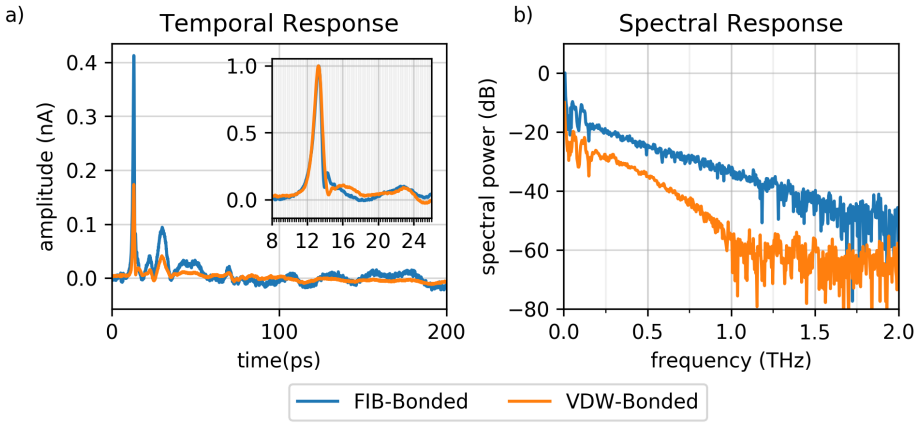

Fig. 7. Experimental result plotting the received THz-bandwidth pulse.

In Fig. 7(a) the received pulse has a relatively flat tail following the main pulse which is desirable for high resolution system. The two peaks following the main pulse in Fig. 7(a) correspond to two resonant cavities, this is seen as ringing below 0.25 THz in Fig. 7(b) (two peaks at 59 GHz and 117 GHz). The first cavity occurs between the receiver and the back of the Silicon frame (along the air/Silicon interface). Quasi-statically the resonance is calculated as $\Delta f = 3 \times 10^8/(2 \times 2.54\times$ 117 GHz) = 0.505 mm which is close to the frame thickness (0.500 mm). The second cavity occurs between the receiver and the end of its contact pads (1.00 mm long). As approximation (ignoring the silicon nitride because it is very thin) this can be calculated quasi-statically as $\Delta f = 3 \times 10^8/(2 \times 2.54\times$ 59 GHz) = 1.04 mm which is close the distance between the receiver and the end of its contact pads. The first ringing effect can be minimized by placing the silicon frame onto another thicker silicon mount which has a rough end-face to minimize reflections. The second ringing effect can be minimized by extending and smoothly flaring the receiver contact pads.

Appendix B illustrates the importance of the thin silicon nitride substrate by plotting the result which uses a glass coverslip as the substrate and the VDW-bonding method.

5. Conclusion

We have demonstrated a simple system-on-chip for the generation and detection of THz-bandwidth pulses after propagating 10 mm on a coplanar stripline defined on a thin silicon nitride membrane. Thin-film LTG-GaAs photoconductive devices are positioned and bonded using two separate bonding methods. Received pulses exhibit low distortion due to the minimal dielectric loading of the thin substrate. A pathway forward to lower propagation loss and increased system functionality is articulated. The combination of thin membranes, photolithographic feature definition and compatibility with surface-mount techniques provides an attractive platform for the construction of complex TSoCs. Challenges in device bonding and heat dissipation are under ongoing investigation as we explore implementation of more complex circuits.

Appendix A - Sweeping the CPS width and separation ratio

As previously mentioned the optimal W/S ratio for the CPS transmission line is not likely obtained when S = W. The concept is illustrated here. Figure 8 plots the simulated attenuation coefficient for a few different frequencies when the total CPS cross-section (S + 2W) is held at 90 μm. From Fig. 8 it is clear that the lowest attenuation occurs near W/S = 0.75 (S = 36 μm and W = 27 μm). Note when S = W the attenuation coefficient is not significantly different than the optimal value.

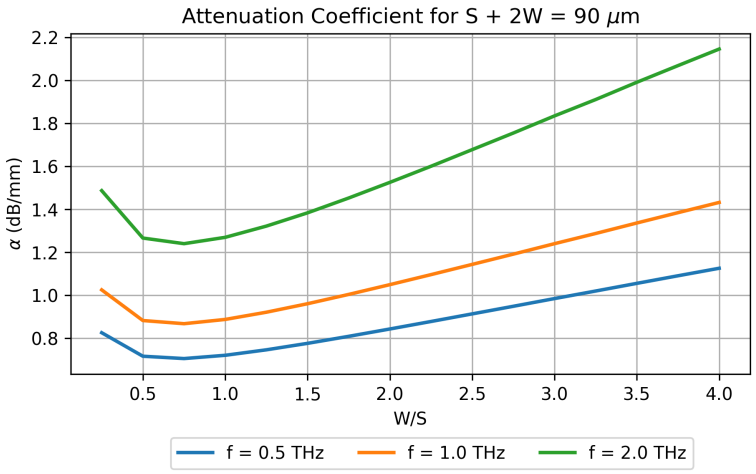

Fig. 8. Simulated attenuation coefficient for a number of S/W ratios at different frequencies.

Appendix B - Experiment on a thick glass coverslip

Before constructing the CPS transmission line on the thin silicon nitride membrane we constructed the same waveguide structure on a 18 mm × 18 mm × 0.18 mm glass cover-slip for fabrication practice. It was expected to have significant pulse distortion due to heavy dielectric loading. Figure 9(a) illustrates the received pulse when using glass cover-slip. Figure 9(b) plots the spectral response. Comparison between Fig. 7 and Fig. 9 illustrates that the usage of a thin membrane can have a profound impact on the performance of the device (as expected).

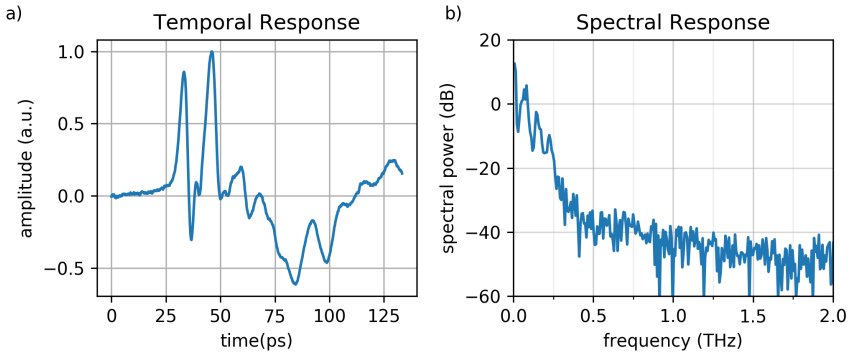

Fig. 9. Detected pulse on glass cover-slip using the VDW-bonding method.

Funding

Natural Sciences and Engineering Research Council (NSERC) Canada.

Acknowledgments

We would like to thank Dr. Thomas Tiedje for the meaningful discussions. We would like to acknowledge the Waterloo Institute of Nanotechnology for fabricating the LTG-GaAs.

References

1. D. Auston, *Picosecond Photoconductors: Physical Properties and Applications* (1984).
2. L. Samoska, "An overview of solid-state integrated circuit amplifiers in the submillimeter-wave and THz regime," IEEE Trans. Terahertz Sci. Technol. **1**, 9–24 (2011).
3. S. Koenig, D. Lopez-Diaz, J. Antes, F. Boes, R. Henneberger, A. Leuther, A. Tessmann, R. Schmogrow, D. Hillerkuss, R. Palmer, T. Zwick, C. Koos, W. Freude, O. Ambacher, J. Leuthold, and I. Kallfass, "Wireless sub-THz communication system with high data rate," Nat. Photonics **7**, 977–981 (2013).
4. T. Nagatsuma, G. Ducournau, and C. Renaud, "Advances in terahertz communications accelerated by photonics," Nat. Photonics **10**, 371–379 (2016).
5. P. Siegel, R. Smith, M. Graidis, and S. Martin, "2.5-THz GaAs monolithic membrane-diode mixer," IEEE Trans. Microw. Theory Tech. **47**, 596–604 (1999).
6. H. M. Cheema and A. Shamim, "The last barrier: on-chip antennas," IEEE Microw. Mag. **14**, 79–91 (2013).
7. M. B. Ketchen, D. Grischkowsky, T. C. Chen, C.-C. Chi, I. N. Duling, N. J. Halas, J.-M. Halbout, J. A. Kash, and G. P. Li, "Generation of subpicosecond electrical pulses on coplanar transmission lines," Appl. Phys. Lett. **48**, 751–753 (1986).
8. H. Cheng, J. Whitaker, T. Weller, and L. Katehi, "Terahertz-bandwidth pulse propagation on a coplanar stripline fabricated on a thin membrane," IEEE Microw. Guid. Wave Lett. **4**, 89–91 (1994).
9. R. Mendis and D. Grischkowsky, "Undistorted guided-wave propagation of subpicosecond terahertz pulses," Opt. Express **26**, 846–848 (2001).
10. K. Wang and D. Mittleman, "Metal wires for terahertz wave guiding," Nature **432**, 376–379 (2004).
11. T. Jeon, J. Zhang, and D. Grischkowsky, "THz sommerfeld wave propagation on a single metal wire," Appl. Phys. Lett.. **86**, 161904 (2005).
12. M. Wächter, M. Nagel, and H. Kurz, "Metallic slit waveguide for dispersion-free low-loss terahertz signal transmission," Appl. Phys. Lett. **90**, 061111 (2007).
13. R. Smith, A. Jooshesh, J. Zhang, and T. Darcie, "Photoconductive generation and detection of THz-bandwidth pulses using near-field coupling to a free-space metallic slit waveguide," Opt. Express **25**, 26492 (2017).
14. S. Yanagi, M. Onuma, J. Kitagawa, and Y. Kadoya, "Propagation of terahertz pulses on coplanar strip-lines on low permittivity substrates and a spectroscopy application," Appl. Phys. Express **1**, 012009 (2008).
15. L. Desplanque, J. F. Lampin, and F. Mollot, "Generation and detection of terahertz pulses using post-process bonding of low-temperature-grown GaAs and AlGaAs," Appl. Phys. Lett. **84**, 2049–2051 (2004).
16. D. Grischkowsky, "Optoelectronic characterization of transmission lines and waveguides by terahertz time-domain spectroscopy," IEEE J. Sel. Top. Quantum Electron. **6**, 1122–1135 (2000).
17. R. D. V. Ríos, S. Bikorimana, M. A. Ummy, R. Dorsinville, and S.-W. Seo, "A bow-tie photoconductive antenna using a low-temperature-grown GaAs thin-film on a silicon substrate for terahertz wave generation and detection," J. Opt. **17**, 125802 (2015).
18. G. Cataldo, J. A. Beall, H.-M. Cho, B. McAndrew, M. D. Niemack, and E. J. Wollack, "Infrared dielectric properties of low-stress silicon nitride," Opt. Express **37**, 4200 (2012).
19. Norcada Inc., https://www.norcada.com/.
20. I. Gregory, C. Baker, W. Tribe, I. Bradley, M. Evans, E. Linfield, A. Davies, and M. Missous, "Optimization of photomixers and antennas for continuous-wave terahertz emission," IEEE J. Quantum Electron. **41**, 717–728 (2005).
21. E. Yablonovitch, D. M. Hwang, T. J. Gmitter, L. T. Florez, and J. P. Harbison, "Van der waals bonding of GaAs epitaxial liftoff films onto arbitrary substrates," Appl. Phys. Lett. **56**, 2419–2421 (1990).
22. ANSYS HFSS V19.1, https://www.ansys.com/products/electronics/ansys-hfss.
23. Y.-S. Lee, *Principles of Terahertz Science and Technology* (Springer, 2009).